THE DEVELOPMENT AND CHARACTERIZATION OF SOL GEL SUBSTRATES FOR CHEMICAL AND OPTICAL APPLICATIONS

By

KEVIN W. POWERS

A DISSERTATION PRESENTED TO THE GRADUATE SCHOOL
OF THE UNIVERSITY OF FLORIDA IN PARTIAL FULFILLMENT
OF THE REQUIREMENTS FOR THE DEGREE OF
DOCTOR OF PHILOSOPHY

UNIVERSITY OF FLORIDA

1998

This work is dedicated to my wife, Michelle, without whose support it would have truly been impossible. She kept the home fires burning and the children healthy and happy when Dad always seemed to be "at the lab!"

ACKNOWLEDGMENTS

There are a number of people who made this work possible and all are deserving of credit. I am particularly grateful to my advisor, Dr. Larry L. Hench, for his support and the freedom he gave me to pursue these investigations. I am also indebted to him for introducing me into the worlds of sol-gel science and biomaterials. I have been particularly impressed with his perspective and his vision of helping mankind through scientific inquiry.

I would also like to thank my committee members, all of whom have been both teachers and friends. I am grateful to Dr. David Clark who gave me an excellent introduction to the field of ceramics, Dr. Joseph Simmons who provided a superb introductions to optics and glass science, and Dr. Jim Adair who taught me materials chemistry (and Civil War history). Special thanks go to Dr. Joseph Delfino who taught me my first college chemistry course over 25 years ago and gave me the most memorable piece of scientific advice; “Follow your nose!”

I am especially indebted to Dr. Jon West who has been a friend, teacher and confidant during my studies.

Finally, I would like to thank the U.S. Air Force for providing much needed financial support through both the G.I. Bill and the AFOSR sponsored ASSERT Grant No. F49620-94-1-0295.

TABLE OF CONTENTS

ACKNOWLEDGEMENTS iii

LIST OF TABLES viii

LIST OF FIGURES ix

ABSTRACT xvi

CHAPTER 1 LOW DENSITY XEROGELS IN THE SPECTRUM OF POROUS GLASSES 1

- 1.1 Vycor® and Phase Separated Glasses 2
- 1.2 Alkoxide Derived Silica Gels 2
- 1.3 The Surface Area of Porous Glasses 5
- 1.4 Pore Volume 5
- 1.5 Pore Size 6
- 1.6 Consolidation 7
- 1.7 Research Objectives 8
- 1.8 Chapter Summaries 9
- 1.9 Conclusions 10

CHAPTER 2 THE SOL-GEL PROCESS 13

- 2.1 Silica in Aqueous Solution 14
  - 2.1.1 DLVO Theory and the Effect of pH on Stability 20
  - 2.1.2 Colloidal Dispersions and Gels 26
  - 2.1.3 Precipitation of Colloidal Silica 28
- 2.2 Silica Gels Derived From Alkoxides 29
  - 2.2.1 Hydrolysis 32
  - 2.2.2 Condensation 38
  - 2.2.3 Re-esterification 40
  - 2.2.4 Solvent Effects 41
  - 2.2.5 Gelation 41
  - 2.2.6 Aging and Syneresis 43
  - 2.2.7 Drying 45
    - 2.2.7.1 Constant Rate Period 45

2.2.7.2 Critical Point ... 47
2.2.7.3 First Falling Rate Period ... 49
2.2.7.4 Second Falling Rate Period ... 51
2.2.7.5 Cracking of Gels During Drying ... 51
2.2.8 Surface Chemistry and Water ... 52
2.2.9 Stabilization and Densification ... 56
2.2.10 Dehydroxylation Treatments ... 60
2.3 Aerogels ... 62
2.3.1 History ... 63
2.3.2 Structural Characteristics ... 64
2.4 Summary ... 65

CHAPTER 3 NITROGEN ADSORPTION FOR SURFACE AREA AND POROSITY DETERMINATION ... 66

3.1 Surface Area -- The BET Equation ... 67
3.1.1 Porosity by Gas Adsorption ... 69
3.1.2 Adsorption Isotherm ... 69
3.1.3 Pore Size Distribution ... 71
3.1.4 Microporous Solids ... 75
3.1.5 Nonporous Materials ... 80
3.2 Nitrogen Adsorption Analysis of Silica Gels ... 80
3.2.1 Preparation ... 81
3.2.2 Interpretation of Results ... 81
3.2.3 Adsorbates Other Than Nitrogen ... 83
3.3 Nitrogen Analysis of Stober Silica Powder ... 84
3.4 Microporous Silica ... 87
3.5 Mesoporous Silica Gel ... 89
3.6 Macroporous silica Gel ... 93
3.6.1 Analysis of Macroporous Gel ... 96
3.6.2 Hysteresis ... 97
3.7 Vycor® Porous Glass ... 101
3.8 Aerogels ... 103
3.9 Conclusion ... 109

CHAPTER 4 FLUORIDE CATALYSIS OF TMOS DERIVED SILICA GEL ... 111

4.1 Hypercoordinated Fluoride-Silicon Complexes ... 111
4.2 Experimental ... 113
4.3 HF Concentration versus Gelation Time ... 116
4.4 The Fate of Fluoride During Polymerization ... 123
4.4.1 Experimental ... 123
4.4.2 Ionic Strength and Activities ... 124
4.4.3 Results and Discussion ... 125
4.4.4 Evidence for a Stable Pentavalent State ... 130

4.4.5 Gelation 135
4.5 Effect of Solvent on TMOS Titration 138
4.6 Conclusions 140

CHAPTER 5 SOL GEL PROCESSING OF LARGE PORE MONOLITHS 142

5.1 Gel Processing 143
5.2 Formulation and Mixing 145
5.3 Cosolvent 151
5.4 Casting 151
5.5 Mold Selection 153
5.6 Aging 154
5.7 Drying 154
5.7.1 Drying Schedule 155
5.7.2 Drying Intact Monoliths 155
5.8 Rehydration and Doping Gel Monoliths 158
5.9 Stabilization and Densification 161
5.10 Conclusions 163

CHAPTER 6 VARIATION OF PORE SIZE BY AGING AND DRYING 165

6.1 The Evolution of Pore Structure During Aging and Drying 166
6.1.1 Experimental 166
6.1.2 Results and Discussion 168
6.1.3 Conclusions 177
6.2 Pore Size Modification by Sacrificial Aging 177
6.2.1 Experimental 179
6.2.2 Results and Conclusions 181
6.3 Effect of Gelation Volume on Pore Texture 183
6.3.1 Experimental 184
6.3.2 Results and Discussion 184
6.3.3 Conclusions 187

CHAPTER 7 PROPERTIES OF LARGE PORE ACID CATALYZED GELS 190

7.1 Texture of Large Pore Gels 191
7.2 Large Pore Gel Texture as a Function of Heat Treatment 198
7.2.1 Results and Discussion 198
7.2.2 Comparison to Smaller Pore Silica Gels 207
7.2.3 Conclusions 209
7.3 Microhardness of Porous Monoliths 209
7.4 Mercury Porosimetry 211
7.5 Optical Scattering in Large Pore Monoliths 215
7.5.1 The Rayleigh Equation 217
7.5.2 Turbidity and Scattering From Sol-Gel Glass 219

7.5.3 Optical Scattering During Sintering. 222
7.6 Fully Dense Large Pore Gels 224
7.7 Conclusions 224

CHAPTER 8 METAL COLLOIDS IN SOL-GEL GLASS 228

8.1 Traditional Gold Ruby Glass 229
8.2 The Mechanism of Colloidal Color 230
8.3 Scattering and Absorption 231
8.4 Scattering in Sol-Gel Derived Porous Glasses 236
8.5 Quantum Size Effects 238
8.6 Variation of Electronic Spectrum with Cluster Size 240
8.7 Nonlinear Effects 241
8.8 Metal Colloids in Sol-Gel Derived Glasses 242
8.8.1 10Å Pores -- Hot Nitric Acid Formula 243
8.8.2 30Å Formula 244
8.8.3 200Å Formula 244
8.8.4 Doping and Heat Treatment 248
8.9 Results and Discussion 248
8.10 Conclusions 251

CHAPTER 9 CONCLUSIONS AND RECOMMENDATIONS 253

9.1 Nitrogen Adsorption Analysis 254
9.2 Fluoride Catalysis 255
9.3 Large Pore Gel Monoliths 256
9.4 Nanocomposites Made with Sol-Gel Glass 258
9.5 Recommendations for Future Work. 258
9.6 Closing 259

LIST OF REFERENCES 260

BIOGRAPHICAL SKETCH 270

LIST OF TABLES

Table Page

1.1 Composition of typical phase separated Vycor® glass 3

1.2 Typical properties of Corning brand (7930) Vycor® glass 3

4.1 Results of HF concentration versus gel time 120

5.1 Formulations for HF catalyzed TMOS derived monoliths. 146

6.1 Pore characteristics of standard 200Å gels at various stages of aging/drying 170

LIST OF FIGURES

Figure Page

1.1 Sol Gel Moon 12

2.1 Solubility of amorphous silica versus pH 15

2.2 Relationship between solubility of amorphous silica in water at 25°C and particle diameter. 17

2.3 Solubility of amorphous silica versus pH at different temperatures. 18

2.4 Principal forms of soluble silica as a function of pH. 19

2.5 Illustration of the major elements of DLVO theory. φ represents the potential at the indicated locations. 22

2.6 Zeta potential versus pH for 1.0 micron Stober silica. 24

2.7 Condensation rate versus pH for acid catalyzed silica gel. 25

2.8 Spherical silica particles made by the Stober process and allowed to slowly settle over a one year period to form an opaline material. (Top) -- a fracture surface. (Bottom) -- surface of opaline compact showing the layered hexagonal close-packed array of spheres. 30

2.9 Stober surface formed on the side of a polymethylpentane mold with spheres stacked in orderly arrays. Note the stacking faults as layers change from hexagonal close packed to simple cubic. (Bottom) -- Same as top but at lower magnification. 31

2.10 Water Concentration versus time of hydrolysis for TEOS and TMOS. 34

2.11 S_N2 Hydrolysis of tetramethoxy silane. 36

2.12 Relative acidity of common ligands attached to oligomeric species of silica 37

2.13 Rate of water loss from an alumina gel illustrating the Constant Rate Period (CRP), First Falling Rate Period (FRP1) and Second Falling Rate Period (FRP2). 46

2.14 Schematic conception of the first falling rate period. Gel begins to turn opaque as the drying front penetrates the gel. 48

2.15 Funicular and pendular states in a porous body. 50

2.16 Different types of silanol groups on the surface of hydroxylated silica. 54

2.17 Concentration of silanols on the surface of various forms of silica. 55

2.18 UV-Vis-NIR spectrum of dense Gelsil®. The ultra-low water content is a result of chlorine dehydroxylation during sintering. 61

3.1 The five types of isotherms as classified by Brunauer, Deming, Deming, and Teller (BDDT). 70

3.2 DeBoer's five types of hysteresis loops 72

3.3 The Kelvin pore radius plotted versus relative pressure for nitrogen at 77.4K. 76

3.4 The t-plots of (a) A nonporous material. (b) A microporous material. (c) A mesoporous material and (d) A mesoporous material with the presence of micropores.. 79

3.5 BET plot and Isotherm for 500nm Stober spheres. 86

3.6 Nitrogen adsorption data for microporous gel. a.) Isotherms. b.) BET plot.. 90

3.7 Micropore analysis for microporous gel. a.) Langmuir isotherm. b.) t-plot. 91

3.8 Adsorption and desorption pore size distributions for microporous gel. 92

3.9 BET data for mesoporous gel. a.) Isotherm. b.) BET plot. 94

3.10 Nitrogen adsorption data for mesoporous gel. a.) Pore size distribution. b.) t-plot 95

3.11 BET data for macroporous gel. a.) Isotherm. b.) BET plot 98

3.12 Adsorption and desorption pore size distributions for macroporous gel 99

3.13 Illustration of capillary condensation in a pore. a.) Cylindrical pore open at both ends filling by condensation on walls. b.) Cylindrical pore filling via a hemispherical meniscus 99

3.14 As soon as the neck fills up as in (a) the entire ink well will fill up if the well diameter is less than or equal to 1/2 the neck as in (b). 102

3.15 BET data for Vycor 7930 porous glass. a.) Isotherm. b.) BET plot 104

3.16 Pore size distribution for Vycor 7930 porous glass. Note the extremely narrow desorption pore size distribution. 105

3.17 Nitrogen adsorption data for an aerogel. a.) Isotherm. b.) Pore size distribution. 107

3.18 BET data for an aerogel. a.) t-plot. b.) BET plot 108

4.1 Plot of hydrolysis time versus pH for fluoride catalyzed gels. Note that for pH's between 1.0 and 2.0 hydrolysis is very rapid, on the order of a minute or less. 115

4.2 Several of the possible combinations of fluoride and hydroxide around the silicon center with tetrahedral, trigonal bipyramidal and octahedral symmetry. 117

4.3 Calibration curve for the fluoride ion-specific electrode. The electrode response shows good linearity throughout its entire range of sensitivity 118

4.4 The gel time(a) and gel rate (b) of an HF catalyzed TMOS sol as a function of HF concentration. 121

4.5 Log-log plot of gel time versus HF concentration showing the point at which the reaction changes from hydrolysis limited to condensation limited 122

4.6 The results of the titration of three different concentrations of HF in nitric acid with tetramethoxy silane 126

4.7 Expanded view of the endpoints of the titrations in Figure 4.6. The higher the initial concentration, the lower the final equilibrium level of fluoride ion. 127

4.8 If the decrease in fluoride concentration is extrapolated to zero, the ratio of (total) fluoride:TMOS is determined by the x-intercept 128

4.9 Initial complexation ratio for more concentrated solutions is 6:1. As availability of silica increases and the endpoint nears, this drops back to the 4:1 ratio seen in the more dilute solutions. 129

4.10 Several examples of possible reactions of HF with silicic acid. 132

4.11 The pH of the solution plotted versus the moles of TMOS added. 133

4.12 At higher HF concentrations, the formation of silicon hexafluoride increases the buffering capacity of the solution and the pH initially rises in (a). As the buffering capacity of the solution is exceeded the pH begins to fall as in (b)... 134

4.13 Proposed mechanism for HF catalyzed condensation involving a pentacoordinate species with a hexacoordinated intermediate. 137

4.14 The effect of added methanol on the titration of acidified HF solution with TMOS such as occurs in the early stages of HF catalyzed sol gel synthesis 139

4.15 Schematic representation of colloidal growth and gelation during HF catalyzed sol gel process synthesis. 141

5.1 Schematic of the basic steps involved in the production of monolithic silica gel products. 144

5.2 Standard aging and drying schedules for small monoliths (2.5cm x .7cm) in the large pore system 147

5.3 A variety of silica gel monoliths made with the "standard" formula for 200 angstrom radius.. 148

5.4 The isotherm (a) and BET plot (b) for a representative silica gel monolith made with the standard formula.. 149

5.5 Pore size distributions (a) and surface area distributions (b) for the same standard formula gel monolith shown in Figure 5.4. 150

5.6 Bubbles can survive the drying process as evidenced by this photograph of two dried gel monoliths. 152

5.7 Desorption pore size distributions for three gels made with the same formulation but with different pore textures due to differences in drying schedules 156

5.8 Several different size silica monoliths made with the same formulation dried with different schedules. 157

5.9 Large pore gel just beginning to enter the opaque stage during drying. 159

5.10 Large pore gel being rehydrated with water in a plastic dish............................. 160

5.11 Series of photos illustrating what happens when rehydration of a large pore monolith is interrupted. 162

5.12 Standard densification schedule for large pore monoliths. 164

6.1 Schematic of aging and drying schedule for four gels taken from the same large pore formulation 169

6.2 Nitrogen adsorption data for Sample #1 (KP70826) solvent exchanged shortly after gelation and supercritically dried. a.) Isotherm. b.) Pore size distribution 171

6.3 Nitrogen adsorption data for Sample#2, solvent exchanged after reaching the critical point and then supercritically dried. a.) Isotherm. b.) Pore size distribution 172

6.4 Nitrogen adsorption data for Sample #3, dried with standard drying schedule. a.) Isotherm. b.) Pore size distribution. 173

6.5 Nitrogen adsorption data for Sample #4 after 2 weeks extended aging and drying schedule. a.) Isotherm. b.) Pore size distribution 174

6.6 Desorption pore size distributions for HF catalyzed gel dried by four different methods. 176

6.7 Schematic showing the pore modification of a large pore gel aged and dried in the presence of a high surface area "seed" gel. 178

6.8 The change in BET surface area as a function of time for a standard 200Å formula gel aged with 1.6 grams of a high surface area silica gel 180

6.9 BET data for gels aged with and without added donor silica. a.) Pore volume as a function of aging time. b.) Average pore radius for the same gels as a function of aging time 182

6.10 Gelation time versus gelation volume 185

6.11 Surface area and pore volume of silica gels composed of 10 ml of a standard sol diluted with methanol to the indicated volume and allowed to gel 186

6.12 Pore radius versus gelation volume for gels diluted with methanol and allowed to gel at different volumes. 188

7.1 AFM image of large pore gel showing the colloidal texture 192

7.2 AFM image of large pore gel fracture surface showing the colloidal nature of the gel. 193

7.3 SEM photo of the large pore gel fracture surface 195

7.4 SEM photo of the as-cast surface of a dried large pore gel 196

7.5 Nitrogen adsorption data for a typical large pore (200Å) gel. a.) Adsorption and desorption isotherms. b.) The pore size distribution.. 197

7.6 Schematic of how large mesopores pores can appear more cylindrical at high relative pressures during nitrogen adsorption analysis 199

7.7 Stabilization schedule used to heat treat and sinter large pore gels prior to analysis 200

7.8 Pore characteristics of large pore gels as a function of stabilization temperature. a.) Surface area. b.) Pore volume 201

7.9 Pore radius versus stabilization temperature for two series of large pore gels 203

7.10 Large pore gel density as a function of stabilization temperature. a.)Structural density. b.) Bulk density. 204

7.11 Overlaying the nitrogen adsorption data for different stabilization temperatures shows the evolution of pore texture during stabilization 205

7.12 As the gel sinters at higher temperatures, pore volume and pore radius decrease while the pore size distribution broadens 206

7.13 Comparison of pore texture for a variety of pore sizes. a.) Surface area versus stabilization temperature for a variety of pore sizes. b.) Pore radius versus stabilization temperature. (Small pore data from Wallace (Wal91).). 208

7.14 Bulk and structural density as a function of stabilization temperature. a.) Bulk density. b.) Structural density 210

7.15 Microhardness and bulk densities of large pore gels as a function of stabilization temperature 212

7.16 Mercury intrusion data for a typical large pore gel. a.) Intrusion curve. Note the linear portion of the curve at low pressures. b.) Regression analysis on the low pressure elastic portion of curve 213

7.17 The bulk modulus of two large pore gels as a function of stabilization temperature. Values were derived from mercury porosimetry measurements 216

7.18 UV-Visible spectrum for a typical large pore gel. a.) Absorbance plotted versus wavelength. b.) The same spectrum with the absorbance plotted against $1/\lambda^4$ showing the linear relationship characteristic of Rayleigh scattering........ 218

7.19 Scattering slopes and regression parameters for acid catalyzed gels of various pore sizes 220

7.20 Plot of the slope of the scattering curves from figure 7.19 versus the average pore radii of several silica gels with different pore sizes 221

7.21 Absorbance plotted versus $1/\lambda^4$ for a large pore gel stabilized at different temperatures 223

7.22 UV-Visible/NIR absorption spectrum of fully densified large pore gel compared to that of dense Gelsil™. 225

7.23 Comparison of UV-Vis spectra (a), and scattering curves (b), for a dry large pore gel (n_{air}=1.00) the same gel filled with deionized water (n_w=1.33)................. 227

8.1 Optical Constants for Gold 232

8.2 Theoretical absorbance and scattering efficiencies as a function of wavelength for 10 and 40nm gold colloids in silica. 234

8.3 Total attenuation factors for transmitted light for several different particle sizes 235

8.4 Plotting the absorbance vs. $1/\lambda^4$ clearly shows the contribution of the plasmon band vis the matrix scattering contribution.. 237

8.5 Desorption isotherm and pore size distribution for microporous (10Å) 245

8.6 Isotherm and pore distribution for 30Å Au doped gel. 246

8.7 Isotherm and pore distribution for large pore (200 Å) silica gel monolith doped with 250ppm Au. 247

8.8 UV- Visible absorption spectra for 10Å and 30Å Au doped gels (200ppm)....... 249

8.9 UV-Visible absorption spectra for 200Å Au doped gel (250ppm). 250

Abstract of Dissertation Presented to the Graduate School
of the University of Florida in Partial Fulfillment of the
Requirements for the Degree of Doctor of Philosophy

THE DEVELOPMENT AND CHARACTERIZATION OF SOL GEL SUBSTRATES FOR CHEMICAL AND OPTICAL APPLICATIONS

By

Kevin W. Powers

May 1998

Chairman: Dr. Larry L. Hench
Major Department: Materials Science and Engineering

The sol gel process can be used to make monolithic porous glass for various scientific and engineering uses. The porosity of the material imparts a large surface area which is advantageous in applications such as catalyst supports or in the study of surface mediated chemical reactions. The chemical stability and transparency of the porous glass also make it suitable for use in the emerging field of optical sensors.

In this study fluoride catalysis is used to produce sol gel monoliths with pore radii of up to 400 Angstroms, four times larger than any previously reported using conventional drying techniques. Gel monoliths with pore radii of 200 Angstroms were found to have the best combination of surface area, pore volume and optical transparency. Typical monoliths have surface areas of 150 m^2/g and pore volumes of 1.60 cm^3/g with good transparency. The monoliths are chemically stable, have good mechanical strength and can be easily rehydrated without cracking. The substrates are also suitable for sintering into dense high purity silica glass with little tendency towards foaming.

An in-depth study of the catalytic effect of fluoride on the sol gel process is also included. It has been theorized that fluoride serves to expand the coordination sphere of the silicon center making it more subject to nucleophilic attack. In this work an ion-specific fluoride electrode is used to monitor free fluoride concentrations in HF catalyzed sols while silicic acid is added in the form of tetramethoxysilane (TMOS). It is found that fluoride is rapidly bound by the silicic acid in a ratio of four to one, indicating the formation of silicon tetrafluoride. A concurrent decrease in pH suggests that a pentacoordinate species is formed that is more stable than previously thought. A polymerization mechanism is proposed that explains the hydrophobicity of fluoride catalyzed gels and the difficulty in retaining structural fluoride in fluoride catalyzed sol gel glasses.

Finally, several porous monoliths are doped with colloidal gold and the optical properties evaluated as a function of heat treatment. This demonstrates the feasibility of using porous glass nanocomposites in sensors and other optical components.

CHAPTER 1

LOW DENSITY XEROGELS IN THE SPECTRUM OF POROUS GLASSES

Porous silicate glasses are produced by two primary methods. The first method is to produce a phase separated glass with two continuous phases and then leach out one of the phases with an appropriate corrosive fluid. This is how Corning Inc. produces Vycor® brand porous high silica glass. The second method and the primary subject of this report is sol gel type glasses which are produced by the controlled gelation of colloidal silica particles or the hydrolysis and condensation of various silicon alkoxides. The sol gel method of producing porous glasses is by far the more flexible of the two for producing a range of properties in the porous glass product. Surface areas, pore volumes, bulk densities and pore sizes can all be engineered through the manipulation of the reaction conditions and post-gelation thermal treatments.

Porous glasses have several unique characteristics which promise to make them a very significant part of our technological bag of tricks. They can be crafted with large surface areas, pore diameters from 1.5 nm to several microns, pore volumes of up to 95%, and densities from $.005 g/cm^3$ up to the full density of fused silica ($2.2 g/cm^3$). They can be synthesized with 99.99+ % purity through the use of silicon alkoxide precursors and doped with virtually any material that can be introduced as a liquid or a gas. They can be made transparent, translucent or opaque by manipulating the pore size and/or incorporating second phases. High purity silica is stable in all but the most severe aqueous environments and is impervious to most organic solvents. Porous silica is also thermally stable and porous silica matrices can maintain their porosity up to 1000°C (Hen90).

1.1 Vycor® and Phase Separated Glasses

Vycor® is the brand name for the phase separated glass products produced by Corning Incorporated. The production of Vycor® is based on the work of Hood and Nordberg (Hoo38, Hoo42). Vycor® type glasses can be made by taking advantage of the phase separation in the silica-borate-soda system. A multicomponent glass is produced consisting of 65% silica, 27% B_2O_5, and 8% Na_2O which is cast in the desired shape. Upon cooling the glass phase separates into two phases, a silica rich phase and a boron/sodium rich phase. Upon further heat treatment, the phases consolidate into two interconnected phases, the size and morphology of which increase with time and temperature. After cooling, the boron/sodium rich phase is leached out of the glass using a hot dilute acid mixture which reacts with the borate and sodium constituents to form soluble species. This is a time consuming operation especially as the thickness of the sample increases. The silica rich phase remains unaffected by the acid solution. The resulting product is a porous glass consisting of approximately 96% silica, 3% B_2O_5, 1% Na_2O and trace impurities. Once the boron and sodium rich phase is etched out, the product is washed to remove the acid solution and dried. The remaining porous glass has chemical and physical characteristics similar to pure silica. Table 1.1 lists the composition of a typical phase separated porous glass and Table 1.2 depicts some of its properties (Elm92).

1.2 Alkoxide Derived Silica Gels

Although sol gel processing of ceramic materials (silica) traces its history back over 100 years, it has only been within the last few decades that an understanding of the physical and chemical processes has begun to emerge. Much of the resurgence in sol gel

Table 1.1 Composition of typical phase separated Vycor® glass (Elm92).

Composition of Vycor®	
Oxide	Wt/% Composition
SiO_2	96.6%
B_2O_3	2.95%
Na_2O	0.4%
$R_2O_3 + RO_2$	<0.1%

Table 1.2. Typical properties of Corning brand (7930) Vycor® glass (Elm92).

Properties of Vycor®	
Appearance	Opalescent
Refractive Index	1.33
Bulk Density (g/cm^3)	1.5
Pore Volume (%)	28
Avg. Pore Diameter (Å)	50
Specific Surface Area (m^2/g)	200
Modulus of Rupture (MPa)	42
Young's Modulus at 22°C (GPa)	17.6

research has been due to the development and use of silicon alkoxides to produce homogeneous gels with a very fine microstructure. Although a wide variety of silicon alkoxides have been synthesized, two, tetraethoxysilane (TEOS) and tetramethoxy silane (TMOS), are the most widely used in producing silica and multicomponent gels. The alkoxides are ideal precursors for research applications but are expensive, volatile, and toxic; attributes that put them at a disadvantage in many industrial applications. TEOS is the least expensive and safest to work with but is relatively slow to hydrolyze when compared to TMOS. This will be discussed in greater detail in the next chapter.

The sol gel process is a product of several unique aspects of aqueous silica chemistry including the low solubility of silica over a wide pH range, the ease in which a solution can be supersaturated with silica, the large surface charge formed on the surface of colloidal silica in aqueous solutions, and the propensity for silanol groups to undergo the condensation reaction to form highly stable siloxane bonds. In alkoxide derived silica gels a number of variables can be manipulated to customize the properties of the resulting glass. The primary variables include the mole ratio of alkoxide to water (R-ratio), the pH, the solvent system, conditions of gelation, the addition of catalysts or other additives, aging times and temperatures, method of drying, and high temperature (stabilization) treatments. Consequently, porous glasses derived from the sol gel process can be synthesized with a much wider range of surface areas, pore volumes and pore diameters than Vycor® type glasses which are limited by the stoichiometry of the separated phases.

The primary drawback of the sol gel process is the difficulty in drying monolithic, net-shape pieces. Porous glasses of all types are prone to cracking due to the large capillary stresses encountered during the drying process but silica gels with their high surface areas and small pore sizes are particularly prone to fail. Many schemes have been developed to solve this problem including surface modification, drying chemical control additives (DCCAs), various aging treatments and supercritical drying (Hen90). Once dried, residual water or other impurities can become a problem when dense silica components are consolidated at high temperatures. Much of the literature is devoted to understanding the principles involved in the sol gel process in order to address these problems.

1.3 The Surface Area of Porous Glasses

Because of the nanometer scale of their porosity, porous glasses have large specific surface areas. A typical Vycor® type glass as noted in Table 1.2 will have a surface area of around 200 m^2/g. Sol gel derived glasses can have surface areas from less than 100 m^2/g to over 1000 m^2/g. Four grams of the latter contains more surface area than a football field. Indeed, some aerogels have been reported to have surface areas as high as 1700 m^2/g, a value that approaches the theoretical (Fri86). Surface areas of this magnitude create a material in which the bulk physical and chemical properties begin to become dominated by its surface properties. Many surface phenomena that hitherto went unnoticed can now be studied, characterized and applied to new technologies. Such large surface areas , for example, are important in applications such as catalyst substrates, surface mediated chemical processes, and the creation of new insulating materials.

1.4 Pore Volume

The available pore volume of phase separated glasses is limited by the stoichiometric proportions of the constituents and the composition of the boron rich phase which is etched out of the phase separated glass. Thus the pore volume is limited to the general vicinity of 25%. Larger pore volumes can be achieved through etching with hydrofluoric acid solutions; however, this abnormally increases the pore size and increases the length and complexity of the synthesis (Cao94). Sol gel derived glasses provide much more flexibility in terms of selecting and producing the pore volume desired for a specific application. In this study, pore volumes ranging from 25% to 80% are routinely produced in xerogels while porosities as high as 95% have been produced through aerogel technology. Combining the two types of processing can yield pore volumes tailored to any intermediate point.

1.5 Pore Size

Porous glasses are generally characterized by mercury intrusion or nitrogen adsorption which provide relatively accurate surface area and pore volume determinations. Each technique has its own advantages and limitations. Mercury intrusion requires very high pressures to measure small pores and gives little information on the micropore content of a material. By contrast, nitrogen adsorption is limited to pores less than about 0.1 micron in diameter (Gre82, Qua85). Pore sizes are generally computed in terms of the hydraulic pore radius which assumes uniform cylindrical pores, a morphology which seldom occurs in either phase separated glasses or sol gel derived glasses. Even so, the hydraulic pore size is a convenient way of categorizing porous glasses and provides the means for comparing different samples. The average pore size is computed using the following equation:

$$r = \frac{2 \cdot V_p}{S.A.} \tag{1.1}$$

where r is the pore radius, V_p is the specific pore volume and S.A. is the specific surface area of the material. Care must be taken not to take this model too literally as the pores are not usually uniform nor cylindrical in shape. Vycor® type porous glasses generally produce pore sizes in the range of 4 nanometers but can be etched to sizes on the order of 20 nanometers. Xerogels can be produced with a wide range of pore sizes from less than 2 nanometers to nearly 100 nanometers. Larger pore sizes are normally produced through aging or etching treatments as with the phase separated glasses (Wal91). Some aerogels have been reported with macropores in the vicinity of 2-3 microns although these are normally associated with a broad pore size distribution (Win84). Although pore size is a convenient characteristic of a porous glass it should always be considered in context with the pore volume and surface area from which it is derived.

1.6 Consolidation

The objectives of this study grew out of the desire to create and characterize porous silica gel matrices or substrates suitable for use in the production of optical sensors. The desired characteristics included a large surface area, large pore openings, sufficient transparency to visible light, and stability under a wide variety of chemical environments. As work progressed toward these goals, it became apparent that these substrates also showed promise as preforms for densification into fused silica pieces and homogeneous doped silica glasses. The production of net shape dense fused silica fixtures and optical components has been the "Holy Grail" of porous glass producers ever since it was discovered that these glasses could be consolidated into dense glass at temperatures much lower than that required for melt derived glasses (Brin90). Due to the extremely high working temperatures (2000°C) and high viscosity of pure silica, it is difficult and expensive to produce pure silica optics via traditional melt technology. Precision shapes are difficult to form, homogeneity suffers and purity is insufficient due to contamination from refractories and retained water. Thus the consolidation of porous silica glasses at lower temperatures is an attractive alternative.

Vycor® type glass suffers from several drawbacks with respect to making optical components. It still must be cast from a molten state and thus requires high temperatures and energy costs. The borate rich phase must be chemically etched out of the glass, a time consuming and not always successful process. After the etching process is complete, drying the glass is difficult, especially for thick pieces. In addition, Vycor® still contains up to 4% sodium and borate in the final dense product.

Silica gels have always suffered from drawbacks as well, primarily, the inability to dry large net shaped pieces intact. Drying monolithic gels intact is a time consuming and fickle operation. The larger the piece, the more difficult and time consuming it is to dry without cracking or warping. Although thermally densified silica gel pieces are much purer than Vycor®, they too tend to retain water due to their large (hydrated) surface area which can result in bloating (the swelling of the glass at high temperature due to the expansion of trapped water). Even when successfully densified, sol gel derived fused silica can contain a few parts per million water. Though this does not seem like much, it is still insufficient purity for many applications such as fiber optic components or laser optics (Hen90).

1.7 Research Objectives

Due to the remarkable properties of the xerogels described herein, the objectives of this research incorporate the following:

> 1. Develop and characterize a monolithic porous silica gel substrate suitable for use in optical sensors. Such a substrate should have a large surface area, large pores with good permeability, sufficient mechanical strength to survive rehydration forces encountered during doping and during use, environmental stability, and adequate optical transparency in the visible spectrum.
>
> 2. Study the effects of soluble fluoride on the gelation process and determine the mechanism by which fluoride catalysis operates at low pH. Determine the amount of fluoride that can be introduced into the wet gel.
>
> 3. Improve on the ability to create large net shape dried monolithic silica pieces suitable for dehydration treatments and densification into high purity dense fused silica pieces. Study the aging characteristics of porous sol gel matrices to maximize strength and minimize retained water. Homogeneity should be sufficient for use in optical applications.

4. Explore the variables for doping silica gel monoliths with second phases in order to produce nanocomposite materials.

1.8 Chapter Summaries

Chapter 2 sets the stage for the investigations that follow by reviewing the sol gel process as it applies to conventional xerogels. The theory of gelation is reviewed starting with the colloidal properties of silica in aqueous solutions but geared specifically towards the production of silica gels using alkoxide precursors. The theory of aging, drying and consolidation is discussed along with a short synopsis of supercritical drying.

Nitrogen adsorption analysis is the principal tool used to determine the texture of silica gel throughout these investigations. BET theory is often applied to porous materials without a true understanding of the physical process involved and how it can be used to elucidate structure and surface properties. *Chapter 3* takes an in-depth look at nitrogen adsorption and how it can be applied to siliceous materials with emphasis on silica gels. Without such a background fundamental errors can be made -- such as the frequent interpretation that the average pore radius represents the true pore size in these materials.

Chapter 4 explores the limits and mechanisms of fluoride catalysis of TMOS gels fabricated at low pH. This chapter sets the stage for the production of large pore sized HF catalyzed gels. There are some surprising results that lead to new insights into the mechanism of gelation under these conditions.

In *Chapter 5*, the fabrication of large-pore gels is described, hopefully in enough detail to be useful for those wanting to duplicate the process. Larger pores are desirable from the standpoint of lower capillary forces during drying, greater permeability of the processed gels and lower surface areas (hence less retained water) during densification. Although pore diameters of up to 80 nanometers have been fabricated, the optical properties in the visible tend to deteriorate due to Rayleigh scattering. Consequently, emphasis has been concentrated on 40 nanometer substrates. The processing parameters and properties have been well-characterized and are predictable. Although specifically oriented towards the large pore gels, many of the techniques are useful for sol gel processing in general.

Chapter 6 explores some fundamental processing issues; particularly the changes in pore morphology through the aging and drying stages of gel processing. Supercritical CO_2 drying is used to produce aerogels at different points in the aging process. This allows a precise analysis of the pore structures at various stages of aging.

The stabilization and densification of large pore gels are investigated in *Chapter 7* along with some of the physical and optical properties of the final product. Enlarging the pores results in lower bulk densities and generally weaker porous structures. Scattering dominates the optical properties in porous glasses and gels eventually lose their transparency in the visible as the pore sizes increase. For the acid catalyzed system, pore sizes can be estimated based on an empirical scattering curve developed here.

Many of the applications for porous glass substrates depend on the introduction of second phases into the pores of the material. In *Chapter 8* colloidal gold particles are introduced and some of the optical properties are evaluated. Novel properties such as high nonlinear optical coefficients are possible by introducing metal colloids to sol gel derived glasses. The introduction of colloidal metal particles may also be useful in the production of catalyst materials.

1.9 Conclusions

Despite the massive amount of research that has been conducted over the last few decades, sol gel science still has many fruitful areas and potential applications. The use of sol gel technology for the production of high purity silica products is still in need of development. The use of porous substrates in optical sensors and as a route to novel optical materials is in its infancy. The work accomplished here has extended the pore sizes that can be routinely fabricated and demonstrates that with a concerted effort virtually any pore size surface area combination is within reach.

Although they have unique and useful properties, silica gels can also be beautiful. Figure 1.1 is the photo of a 200Å pore radius gel fabricated according to the procedures in Chapter 5. The gel has been filled with liquid nitrogen which is allowed to evaporate at room temperature giving it the appearance of the moon on a cloudy evening.

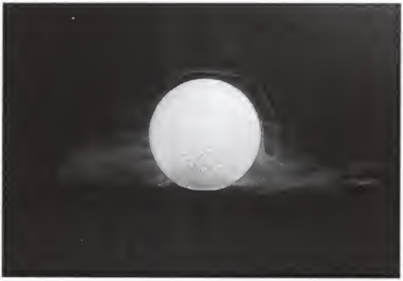

Figure 1.1. The *Sol Gel Moon*. Photo of a standard 200Å pore radius gel as it outgasses after being filled with liquid nitrogen.

CHAPTER 2

THE SOL GEL PROCESS

Sol gel processing of ceramic materials (silica) traces its history back over 100 years to the mid-19th century with the works of Ebelman and Graham and their study of aqueous colloidal suspensions of silica (Ebe46, Gra64). Over the ensuing 15 decades, a great deal of progress has been made in characterizing silica suspensions and in the basic understanding of the physical and chemical processes that occur both in solution and as the liquid to solid transformation takes place. In the 1950s and 1960s, Ralph Iler and his contemporaries conducted an exhaustive investigation into the solution chemistry and colloidal properties of silica leading to his seminal work, The Chemistry of Silica (Iler79). Many commercial applications were derived from Iler's investigations at DuPont including the colloidal silica Ludox, and various other silica products (Ale65).

In the last two decades, great excitement has been generated through the increasing use of silicon alkoxides, primarily tetra-ethoxy silane (TEOS) and tetra-methoxy silane (TMOS), as precursors in producing silica gels and other colloidal products. It is due to this flurry of investigation into silica gels that the study of a wide variety of metal alkoxides and mixed component alkoxides has dramatically increased over the past two decades. Over the last twenty years thousands of journal articles, proceedings, books and other communications have been written regarding the study of sol-gel glasses. More recently Brinker and Scherer have attempted to consolidate the principles of sol gel physics and chemistry in their book Sol Gel Science (Bri90). A more recent source on the latest developments in the science of silica is the book The Colloidal Chemistry of Silica, edited by H.E. Bergna for the American Chemical Society (Berg94a).

As most of the research herein deals with single component silica gels and glasses using alkoxide precursors, the following review of the sol gel process is limited primarily to this topic. The sol gel process involves several unique aspects of aqueous silica chemistry including the solubility of silica as a function of pH, the ease in which a solution can be supersaturated, the large surface charge formed on colloidal silica in aqueous solutions, and the propensity for silanol groups to undergo a condensation reaction to form highly stable siloxane bonds.

2.1 Silica in Aqueous Solutions

In aqueous solutions the sol gel process begins with the solubility of silica. Monosilicic acid, $Si(OH)_4$ has never been isolated. A weak acid, it is only sparingly soluble in water and polymerizes to dimers, trimers and higher oligomeric forms when attempts are made to concentrate it. Ultimately it condenses to the solid phase SiO_2 with which it remains in aqueous equilibrium. This is the basis for the gelation and/or precipitation of SiO_2 monoliths and powders.

In 1855 Struckman determined the solubility of silica in water to be in a range from 100 - 150 ppm at ordinary temperatures (Str55). Over the ensuing years a variety of investigators have arrived at slightly different figures which Iler attributes to the morphological differences in the form of silica tested. Figure 2.1 shows the solubility of amorphous silica versus pH as determined by Alexander (Ale67). Although differing slightly in the absolute values of silica solubility, investigators all agree on the general shape of the curve. The solubility increases somewhat at very low pH or when in equilibrium with small particles or gels with large surface areas. As the pH exceeds 8 to 9, the solubility of silica rises rapidly as is well known by the propensity of silicate glasses to dissolve in strong bases. The solubility can be dramatically affected by the size of the

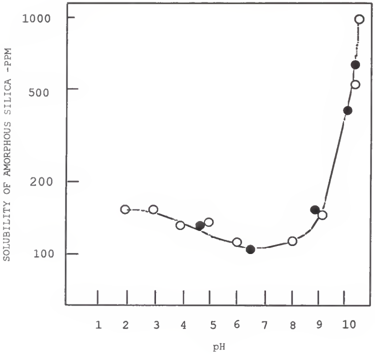

Figure 2.1. Solubility of amorphous silica vs pH: o - Alexander 24°C. • - Cherkinskii and Knyaz'kova 19°C. (Iler79)

colloidal silica particles and or the specific surface area of a silica gel. Figure 2.2 shows the increase in solubility as particle size decreases. Notice that the solubility of silica rises rapidly as the particle size drops below a few nanometers in diameter. Solubility also rises with increasing surface area. Alexander showed that a silica gel with a specific surface area of greater than $600m^2/g$ demonstrated a solubility of 200 ppm at 25°C, nearly twice that of less active forms.(Ale54). As might be expected the solubility also increases (albeit more modestly) at elevated temperatures as depicted in Figure 2.3. In general one can assume that the solubility of amorphous silica in ordinary water at ordinary temperatures is on the order of 120 ppm following the general trends indicated by Figure 2.1. Due to its ability to polymerize into several oligomeric species, the form in which soluble silica exists was the subject of much early study. The silicate species that predominate at different pHs were investigated by Baes and Messmer and are depicted by Figure 2.4. (Bae76). The various oligomeric species are in a dynamic equilibrium with each other. At low pH the predominant species was thought to be monosilicic acid. Dimeric and higher oligimers increase as the pH increases above 8 particularly in concentrated solutions. Monosilicic acid, H_4SiO_4, is stable in water below its solubility limit but has never been isolated. As the solubility is exceeded, the silicic acid monomer is either deposited as amorphous solid silica or, depending on pH, polymerizes by condensation to form soluble oligimeric forms. Monosilicic acid has dissociation constants as determined by Scherban as follows (Sche67):

$$K_1 = [H^+][H_3SiO_4^-]/[H_4SiO_4] = 2 \times 10^{-10}$$
$$K_2 = [H^+][H_2SiO_4^{2-}]/[H_3SiO_4^-] = 2 \times 10^{-12}$$
$$K_3 = [H^+][HSiO_4^{3-}]/[H_2SiO_4^{2-}] = 2 \times 10^{-12}$$
$$K_4 = [H^+][SiO_4^{4-}]/[HSiO_4^{3-}] = 2 \times 10^{-12}$$

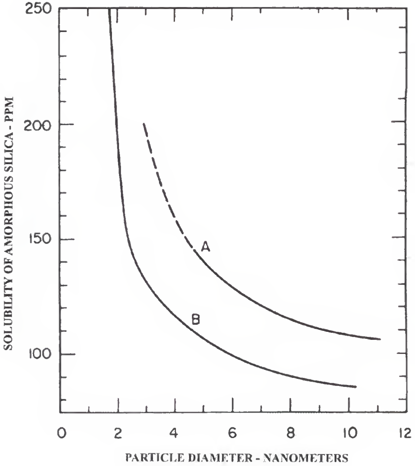

Figure 2.2. Relationship between solubility of amorphous silica in water at 25°C and particle diameter. A - particles made at 80°C - 100°C; B- particles made at 25°C - 50°C at pH 2.2 (Iler79).

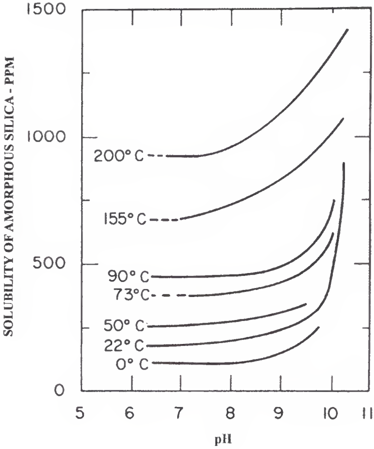

Figure 2.3. Solubility of amorphous silica versus pH at different temperatures. (From Iler after Goto (Iler79).)

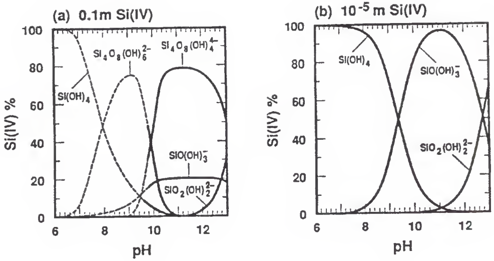

Figure 2.4 Principle forms of soluble silica as a function of pH (Bae76).

Due to the small dissociation constant and the low solubility, soluble silica by itself does not significantly change the pH of solutions. For example, a 100 ppm solution of monosilicic acid at 25°C could be expected to have a pH of only 6.3.

2.1.1 DLVO Theory an the Effect of pH on Stability

Due to the dramatic effect of pH on the stability of silicic acid and colloidal silica solutions, it is useful to consider the effect of pH in more detail. The DLVO theory (developed and named after Derjaguin, Landau, Verway and Overbeek) addresses the stabilization of colloids through the analysis of the various attractive and repulsive forces acting upon small particles in solution. The primary forces attracting particles together are Van der Waals forces while the principal repulsive forces are normally electrostatic in nature. Steric forces also play a role in the stabilization of many colloids. Vander der Waals forces (sometimes called dispersion forces) are attributed to the polarizability of atoms and are inversely proportional to the sixth power of separation between particles. Van der Waals forces include those between two permanent dipoles (Keesom forces), the forces between a permanent dipole and an induced dipole (Debye forces), and those between induced dipoles (London forces). Hydrogen bonding is a particularly strong attraction between dipoles engendered by the small size and lack of electronic shielding around the hydrogen atom. These attractive forces combine to provide the driving force behind the aggregation of colloidal particles. The attractive forces are relatively long range on an atomic scale and can extend to several nanometers from the surface of the particles. The principal repulsive force opposing these Van der Waals forces is electrostatic caused by the surface charge that develops on the colloidal particles in solution. According to DLVO theory, colloidal suspensions are stabilized primarily by these repulsive forces.

In DLVO theory surface charge is developed by the adsorption of charge determining ions (also called potential determining ions) consisting of H^+ and OH^- for most metal oxides. The selective adsorption of these ions is dependent on the nature of the particle surface and the relative concentration of these ions in solution i.e. the pH. Upon developing a charge, the surface naturally attracts an "atmosphere" of counterions of opposite charge which screen the surface by forming a tightly bound layer over the surface. This tightly bound layer is called the Stern layer which terminates at what is called the Helmholtz plane. The Stern layer is characterized by a linear relationship between the electrostatic potential and distance. Outside of this lies the diffuse double layer or Gouy layer where the counterions diffuse more freely. When a colloidal solution of charged particles is subjected to an electric field, they move toward the electrode that is oppositely charged in a process called electrophoresis. The shear plane is the boundary between the "atmosphere" of solvent and counterions that moves with the particle and the bulk of the solution. The potential at the shear plane is dependent on the surface charge and the nature of the counterion atmosphere between the two. This potential can be measured by various techniques and is called the zeta potential (ξ). Due to the intervening counterions, the zeta potential is normally smaller than the surface potential. Figure 2.5 depicts the important elements of DLVO theory with respect to the surface of a particle.

The point of zero charge (PZC) is defined as the pH at which the net surface charge of colloidal particles is zero. This is inclusive of all potential determining ions adsorbed on the surface. The isoelectric point (IEP) is the pH at which the electrophoretic mobility is zero, that is, where the potential at the shear plane (ξ-potential) is zero. The IEP depends not only upon the surface potential of the particle but also upon the nature of the solvent atmosphere around it. Thus in an aqueous solution both the pH and the concentration (and nature) of the counterions affect the IEP. It can also vary with the size and morphology of the colloidal particles. The IEP and zeta potential are very important

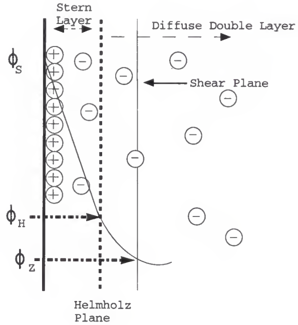

Figure 2.5. Illustration of the major elements of DLVO theory. φ represents the potential at the indicated locations.

in determining the behavior of colloidal systems. In general the PZC and IEP are not equal.

The PZC for silica has been variously measured at a pH between 2 and 3 (DeBu72). It is listed by Parks as 2.5 (Park65). The IEP of silica was found by DeBoer to be between 1 and 1.5. They also noted that this corresponded to the lowest condensation rate between silicic acid monomers (DeBo60). Other authors have variously measured the PZC and IEP of silica to be between a pH of 0.5 and 3.7. Iler has concluded that the average PZC and IEP of various types of silica appear to center around a pH of 2.0±0.5.

The variability is attributed to the likelihood that most measurements are taken in solutions of monosilicic acid mixed with a variety of polymeric forms (Iler79). Much of the controversy surrounding the surface characteristics of silica has to do with its behavior in the vicinity of the IEP. Freundlich was one of the first to point out the anomaly that whereas most lyophobic colloids are least stable at the IEP, silica appears to be unusually stable (Berg94b). Figure 2.6 shows the zeta potential (ξ) of silica as a function of pH while Figure 2.7 shows the effect of pH on gel time for a colloidal silica in water. Note the correlation between the IEP and the pH at which the condensation rate is a minimum. Ordinarily one would expect a maximum coagulation rate at the IEP. The explanation for this anomaly still eludes us but it has been suggested that, because of its small size and unusually small Hamaker constant, silica is stabilized by a layer of water that delays coagulation at its IEP (Col94).

Israelachvili attributes the increased stabilization of silica colloids to a repulsive structural or hydration force that is monotonically varying. He proposes that it arises from strongly H-bonding surface groups, such as hydrated ions or OH^- groups, which modify the H-bonding network of the liquid water adjacent to them. Their effective range is about 3-5 nm, which is about twice the range of the oscillatory solvation force in water. In other words, even in an electrically neutral state such as in the vicinity of the IEP, silica

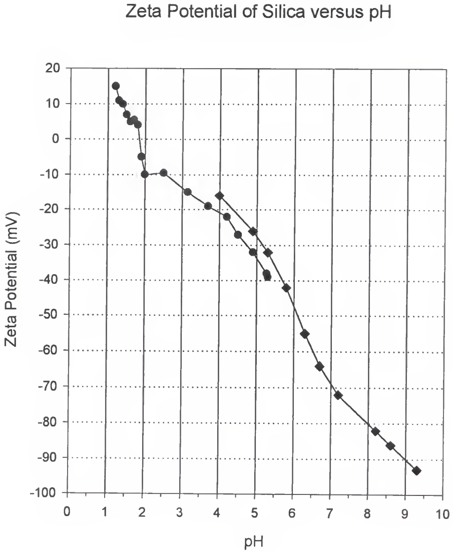

Figure 2.6. Zeta potential versus pH for 1.0 micron Stober silica (Cara96).

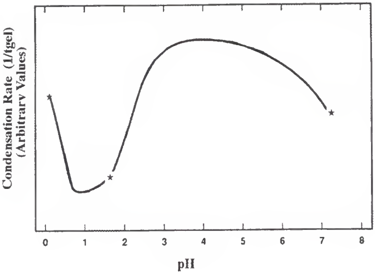

Figure 2.7. Condensation rate versus pH for acid catalyzed silica gel (Bri90).

has such a hydrophilic surface that it forms a thick layer of hydrogen bonded water which provides a repulsive force between particles (Isr92).

In view of the unique properties of water that result from hydrogen bonding, this hypothesis seems reasonable. However, it is still not well understood. Healy recently suggested a model of silica and water based on the formation of surface steric barriers of polysilicate and bound cations which inhibit coagulation (Hea94). He points out that soluble silicates are universal dispersants of many electrostatic colloids which adsorb high densities of aqueous silicate species on their surface and proposes that the mechanisms are more than purely electrostatic.

2.1.2 Colloidal Dispersions and Gels

According to the International Union of Pure and Applied Chemistry (IUPAC) a colloidal dispersion should be defined as a system in which particles of colloidal size of any nature are dispersed in a continuous phase of a different composition or state (Cor88). Colloidal size is generally understood to mean particles that are too small to be affected by gravitational forces ($<1\mu m$) but large enough to be differentiated from solvated species ($>1nm$). Particles in this size range ($1nm - 1\mu m$) are dominated by short range forces such as Van der Waals and surface forces. A stable dispersion of solid colloidal particles in a liquid is called a sol. A gel is defined as a continuous solid skeleton made up of colloidal particles or polymers surrounding a continuous liquid phase. When a gel is dried by evaporation of the liquid phase under normal conditions, the product is called a xerogel.

Due to the surface tension of the solvent, xerogels normally experience significant capillary forces and hence shrinkage during this process. An aerogel is a gel that has been dried by removing the solvent at temperatures above the critical point thus eliminating normal capillary pressures which tend to cause the gel to shrink or fracture. Thus, it is assumed that in an aerogel the structure is much closer to that in the wet state. This feature of aerogels will be used in Chapter 5 to elucidate structural changes during aging.

Silica sols typically have particle sizes in the 5-100nm range and under certain conditions can persist for long periods of time without loss of stability. Silica sols lose their colloidal stability when particles aggregate. This aggregation can be through gelation, coagulation, flocculation or coacervation. Iler (Iler79) defines these terms as follows:

> 1. *Gelling* - Gelling is a process in which the particles are linked together in branched chains that fill the whole volume of sol so that there is no increase in the concentration of silica in any macroscopic region in the medium. Instead, the overall medium becomes viscous and then is solidified by a coherent network of particles that, by capillary action, retains the liquid.
>
> 2. *Coagulation* - Coagulation is the process in which particles come together into relatively close-packed clumps in which the silica is more concentrated than in the original sol so the coagulum settles as a relatively dense precipitate. Industrial precipitated silicas are powders formed when the ultimate silica particles are coagulated as loose aggregates in the aqueous medium, recovered, washed, and dried. A simple way to differentiate between a precipitate and a gel is that a precipitate encloses only a part of the liquid in which it is formed.
>
> 3. *Flocculation* - Flocculated particles are linked together by bridges of the flocculating agent that are sufficiently long so that the aggregated structure remains open and voluminous. It is apparent that these differences will be noted mainly in dilute sols containing only a few percent of silica. In concentrated mixtures one can distinguish a gel, which is rigid, but not between a coagulate and a flocculate.
>
> 4. *Coacervation* - A fourth type of aggregation is coacervation, in which the silica particles are surrounded by an adsorbed layer of material that makes the particles less hydrophilic, but does not form bridges between particles. The particles aggregate as a concentrated liquid phase immiscible with the aqueous phase.

2.1.3 Precipitation of Colloidal Silica

If enough silicic acid is present or a continuous supply is provided, colloidal particles are formed and begin to grow. As the size and concentration of the colloidal particles increase, the sol either gels into a solid mass or the colloids aggregate and precipitate out of solution. The entire process is mediated by the aqueous environment, the most important aspect of which seems to be the pH. The condensation reaction between two silanol groups at first glance appears to resemble the condensation type polymerization that occurs with organic polymers. Investigations by Carmen as far back as 1940 however, indicate that silicic acid polymerizes first into discrete colloidal particles which in turn aggregate into either chains and networks or larger particles depending on the conditions (Car40). Iler summarizes the process in three steps:

1. Polymerization of monosilicic acid to form primary particles.

2. Growth of particles.

3. Linking of particles into chains and networks which are linked to form larger particles which extend throughout the liquid, thickening it into a gel.

Under some conditions, particularly at high pH, the primary particles form larger colloidal aggregates which precipitate out. This occurs for example in the production of monodisperse silica spheres using the Stober process (Stob68). A solution of ammonium hydroxide in a water ethanol solution pH is first prepared after which TEOS is added. After a few minutes the solution begins to turn cloudy as the particles grow large enough to scatter light. The formation of particles is encouraged by a large R ratio (R=moles H_2O/moles TEOS) and a high pH. The combination promotes rapid condensation which encourages the formation of more compact particulates over linear or network-like chains of small primary particles. The ultimate sphere size is controlled by the concentrations of ammonia and water and in some cases temperature.

Figures 2.8 and 2.9 show a series of SEM photographs illustrating the uniformity of the Stober spheres produced by this process. Using TEOS as the primary silica source, spheres up to 1.5 µm can be made. With other alkoxides such as tetrapentyl orthosilicate, spheres up to 2µm have been reported (Bog88). Larger spheres begin to lose their uniformity as radius of curvature increases altering the driving force for growth. Rapid particle formation is enhanced through the *Ostwald ripening* mechanism where larger particles grow at the expense of smaller, more soluble particles with higher surface energy. This is especially true at higher pH due to the greater overall solubility of silica in this environment. A similar effect is produced by neutral pH solutions of NH_4F where the fluoride ion acts in much the same way as the OH^- in promoting condensation.

LaMer and Dinegar explained the growth of monodisperse particles by a nucleation and growth model (LaM50). According to this model, a critical concentration of silicic acid is produced by the rapid hydrolysis and condensation. A burst of nucleation is then produced which rapidly reduces the concentration below C_n. Thus nucleation occurs almost as a discrete step. After the concentration decreases below C_n further nucleation is unlikely and growth of the existing nuclei proceeds uniformly until an equilibrium is reached. It is this single burst of nucleation which confers monodispersity to the colloid. This is consistent with what we know about the catalytic effect of OH^- on the condensation reaction between two silanol groups. Indeed, Alexander produced stable sols of particles only 8 nm in diameter but with over 30% solids loading. Base stabilized sols have also been produced containing 50% by weight of SiO_2 by making particles 20 - 25 nm in diameter and adding an optimum amount of alkali and salt (Iler79).

2.2 Silica Gels Derived from Alkoxides

Today, silica gels and many types of silica powders of high purity are synthesized using silicon alkoxides, most often tetraethoxy orthosilicate (TEOS) and tetramethoxy

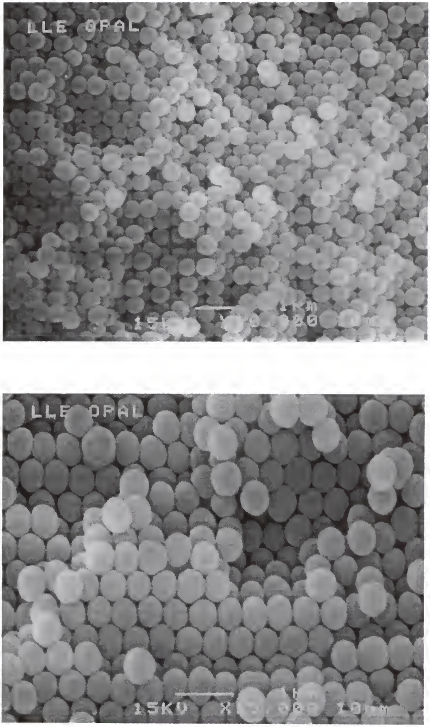

Figure 2.8. Spherical silica particles made by the Stober process and allowed to slowly settle over a one year period to form an opaline material. (Top) - a fracture surface. (Bottom) - surface of opaline compact showing the layered hexagonal close-packed array of spheres.

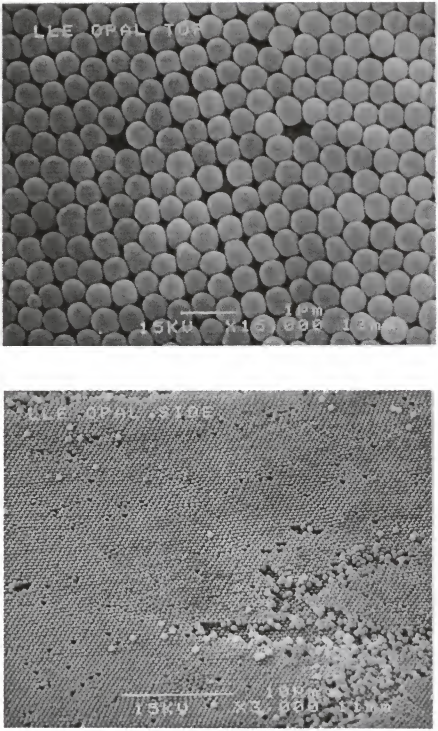

Figure 2.9. Stober surface formed on the side of a polymethylpentane mold with spheres stacked in orderly arrays. Note the stacking faults as layers change from hexagonal close packed to simple cubic. (Bottom) - Same as top but at lower magnification.

orthosilicate (TMOS). Advantages of using these precursors include higher purity and better control over colloid formation and growth. The chemical reactions of these reagents in aqueous environments fall into two primary categories, hydrolysis and condensation.

Hydrolysis

$$\equiv\text{Si-OR} + H_2O \leftrightharpoons \equiv\text{Si-OH} + \text{ROH} \qquad [2.1]$$

Alcoholic Condensation

$$\equiv\text{Si-OR} + \text{HO-Si}\equiv \leftrightharpoons \equiv\text{Si-O-Si}\equiv + \text{ROH} \qquad [2.2]$$

Water Condensation

$$\equiv\text{Si-OH} + \text{HO-Si}\equiv \leftrightharpoons \equiv\text{Si-O-Si}\equiv + H_2O \qquad [2.3]$$

Note that there are two types of condensation, condensation between two silanol groups, or water condensation, and condensation between a silanol and an unreacted alkoxy group, or alcohol condensation. Likewise, depending on the concentrations and conditions, any of these reactions can and do proceed to an appreciable extent in the reverse direction, a process called re-esterification. Reaction rates are governed not only by the reactant concentrations and reaction conditions but also by inductive and steric effects of the alkoxy groups.

2.2.1 Hydrolysis

Hydrolysis is the first chemical reaction step in the sol gel process when using alkoxide precursors. In hydrolysis the silicon alkoxide is separated from the alcoholic ligands to form a supersaturated solution of silicic acid. Hydrolysis occurs by the nucleophilic attack of water on the silicon atom in the silicon alkoxide as demonstrated by isotopic studies using ^{18}O (Kha52).

$$\equiv Si\text{-}OR + H_2{}^{18}O \rightleftharpoons \equiv Si\text{-}{}^{18}OH + ROH \qquad [2.4]$$

This reaction is catalyzed by either acids or bases (McN80). The most common catalysts are mineral acids or ammonium hydroxide, but organic acids, mineral bases, fluorides, hydrogen peroxide and many other compounds have been discovered that catalyze the reaction. Rate constants calculated by Pohl and Osterholz indicate that hydrolysis appears to be specific acid (H^+ion) and specific base (OH^- ion) catalyzed although there have been reports of general base catalysis under some conditions (Poh85). In general, acid catalysis gives a more favorable hydrolysis rate while base catalysis is more favorable for condensation. Steric and inductive factors of the silicon ligands play a strong role in hydrolysis. As the R group on the alkoxide grows larger, the rate constant for hydrolysis decreases. This is particularly true for branched groups. TMOS, with its small methoxy group (≈0.2nm), is particularly well known for its rapid hydrolysis under a variety of conditions, even at neutral pH. TEOS hydrolyses very slowly at a pH of 7 (Ael50). An acid catalyzed solution of TMOS with an excess of water is substantially hydrolyzed within several minutes (with a rapid rise in temperature) whereas complete hydrolysis of a similar TEOS solution may take hours or even days. Consequently, the rate of gelation of TMOS sols is normally considered to be condensation limited while those of TEOS and higher alkoxides is typically limited by the hydrolysis of the precursors. (See Figure 2.10.) The rapid hydrolysis of TMOS makes it hazardous, particularly to the eyes, lungs and mucous membranes. In addition to its higher vapor pressure, TMOS hydrolyzes on contact with moist surfaces forming silica and toxic methanol. TEOS although still hazardous reacts more slowly and produces less toxic ethanol. (In either case, it is

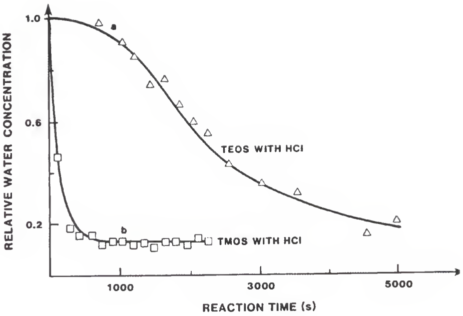

Figure 2.10 Water Concentration versus time of hydrolysis for TEOS and TMOS (Bri90).

advisable to avoid contact with the liquid, work in a hood and protect one's face and lungs with an appropriate breathing apparatus.)

The reaction order of hydrolysis is second order with respect to water and first order with respect to silicate. This is indicative of a bimolecular nucleophilic displacement reaction (S_N2) involving a pentacoordinate (or higher) transition state. Molecular orbital (MO) calculations by Davis and Burgraaf showed a pentacoordinate intermediate with unusual stability (Dav88). This petacoordinate intermediate stretches the silicon oxygen bonds making the alkoxides better leaving groups. In acid catalyzed hydrolysis the alkoxide group is first protonated followed by nucleophilic attack of water on the silicon. Protonation of the alkoxy group withdraws electron density from the silicon making it more subject to nucleophilic attack by water. (See Figure 2.11.)

Inductive effects are also important in hydrolysis. Any electron providing group substituted on the silicon will, under acidic conditions, increase the reaction rate. Electron withdrawing substituents decrease the electron density in the silicon center making it less subject to nucleophilic attack. (See Figure 2.12.)

Under basic conditions, the mechanism is still S_N2 but with the hydroxyl anion acting as the nucleophile. Under base hydrolysis, however, electron withdrawing groups increase reactivity by making the silicon center a better electrophile. This explains why hydrolysis is more favored by acid catalysts and also why the siloxane bond is more vulnerable under basic conditions. Note that under acid conditions one would expect a decrease in reaction rate for each successive hydrolysis (electron withdrawing) while the opposite holds for basic conditions.

For both TEOS and TMOS, except under extreme conditions of pH, the equilibrium lies substantially towards the formation of siloxane (Si-O-Si) bonds under normal conditions of temperature and pressure. As might be deduced, the concentration of water is a key factor, a large excess promoting more rapid hydrolysis. In fact, water has such a significant effect that most literature describes the reaction conditions with a

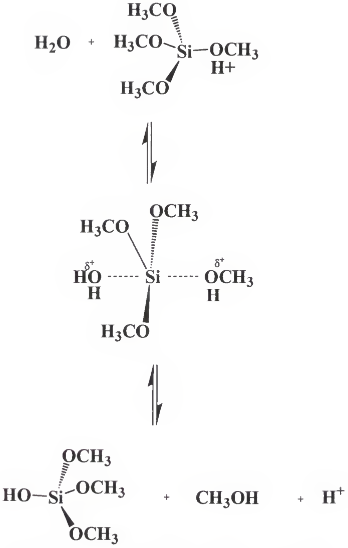

Figure 2.11. S$_N$2 Hydrolysis of tetramethoxysilane.

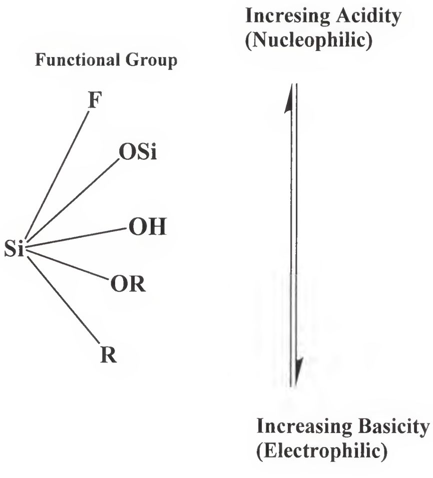

Figure 2.12. Relative acidity of common ligands attached to oligomeric species of silica.

term called the *R-factor* where R = molesH2O/molesTEOS (or TMOS as the case may be). It is important to note that both the hydrolysis and alcoholic condensation rates for TMOS are significantly greater than the corresponding rates for TEOS even though the -OEt substituents of TEOS would be expected to provide greater electron density. It is apparent therefore, that the steric effects are more important in determining the reaction kinetics.

2.2.2 Condensation

As seen in equations [2.2] and [2.3] there are two types of condensation reactions that form siloxane bonds, condensation between silanol groups and condensation between a silanol and an alkoxide group. The former produces a water molecule while the latter results in the respective alcohol. As indicated earlier, the same catalysts employed to increase hydrolysis are also effective for increasing the condensation rate, namely most acids, bases and fluoride. The gel time is often used to represent the overall condensation kinetics for sol gel systems where the gel time $\propto$ 1/(average condensation rate). Using this standard, Figure 2.7 indicates that the overall condensation rate is minimized in the vicinity of pH 1.5. It has been shown that below a pH of about 2 the polymerization rate is proportional to $[H^+]$ while above this pH it is proportional to $[OH^-]$ (Bri90). However the OH^- concentration seems to have the more significant effect. The condensation rate is maximized near neutral pH where significant concentrations of both protonated and deprotonated silanols exist.

At higher pH, base catalyzed condensation has been noted to result in more condensed structures leading to particle formation or, in the case where gelation can be induced, coarser, more particulate gels. Several reasons have been suggested for this behavior. At higher pH silica becomes more soluble as lower order oligimers rather than silicic acid. Thus the basic building blocks of the gel may be larger to begin with. Iler suggested that under conditions where depolymerization is favored, restructuring occurs more readily resulting in the formation of highly condensed colloidal particles (Iler79). It is in this high pH range where depolymerization begins to occur at an appreciable rate leading to reconstruction into more condensed species. Iler also pointed out that for the base catalyzed condensation to occur, the silicon atom has to be attacked by a deprotonated silanol. Siloxane bonds impart a greater acidity to an adjacent silanol than do other silanols.

In other words, polysilicic acid is a stronger acid than monosilicic acid. Consequently, monomers react preferentially with higher polymerized species yielding condensed structures. Finally, larger colloidal particles are stabilized by surface charge which increases with both pH and with particle size resulting in more stable particulate sols at higher pHs. Due to the large zeta potential at higher pHs and the formation of stable colloids, gelation is less likely as pH increases above 8 or 9. Hence large colloids or aggregates tend to form at high pH. The Stober process is a good example of this.

Two kinetic models for polymer growth are the monomer-cluster aggregation (MCA) and the cluster-cluster aggregation (CCA) (Bri90). In MCA, growth occurs by the addition of monomers to higher molecular weight clusters. In CCA growth occurs through the addition of cluster to cluster. Reaction limited conditions indicate that the condensation rate is low enough with respect to diffusion for the cluster or monomer to contact many sites before reacting at the most favorable one. According to Brinker, reaction-limited conditions apply to most silicate synthesis schemes (Bri94). MCA requires a continuous source of monomers, which as we have seen above react preferentially with higher molecular weight species in high pH conditions. Because such growth occurs monomer by monomer, growth sites are all accessible and a dense compact product is produced. ^{29}Si NMR has shown that under neutral to basic conditions, monomer remains available throughout the reaction of the sols (Kel86).

In CCA, on the other hand, monomers are depleted early in the growth process. Consequently, growth must occur between clusters. Due to steric considerations such as the screening of the interior of clusters, highly ramified structures are formed characterized by a mass fractal dimension of $D \approx 2$ (Porod slope$\approx$-2). This structure is most often observed in gels produced by acid catalyzed conditions. In contrast with the basic sols, ^{29}Si NMR shows acidic sols depleted in silica monomers very early in the polymerization process.

Fluoride has a particularly large catalytic effect on silica reactions even at low concentrations. Slightly smaller than the hydroxyl ion, the fluoride ion is even more highly nucleophilic and can be used in an acidic (low OH^-) environment to promote rapid condensation (Isr92). Thus the addition of a small amount of fluoride under acid conditions catalyzes both hydrolysis and condensation, resulting in rapid gel formation at low pH and rapid aggregation at high pHs. Fluoride catalysis is considered in greater depth in Chapter 4.

2.2.3 Re-esterification

The re-esterification of polysiloxanes appears to occur more easily under acidic conditions than under basic conditions (Col94). The rate of re-esterification is only 3.5 to 6 times slower than the condensation rate. This results in acid catalyzed gels containing residual alkoxide groups even though the hydrolysis is nearly complete. Low R ratios and high alcohol content also promote re-esterification via LeChatelier's principle. It is likely that the first step of re-esterification under acidic conditions involves the protonation of the silanol group while in basic condition it involves the deprotonation of an alcohol group. Due to the ease with the silanol is protonated under acidic conditions, this reaction tends to occur more readily under acid catalyzed conditions. Re-esterification of the gel surface is often observed upon drying gels in excess alcohol or after a solvent exchange where water is substantially removed prior to the alcohol.

2.2.4 Solvent Effects

Since most alkoxides are not by themselves water soluble, a cosolvent, (usually an alcohol) is frequently used to ensure the miscibility of the reactants with water. Even in the case where hydrolysis is rapid, homogenization of the solution is due in part to the production of the respective alcohol. Therefore, the presence of a cosolvent must always be considered.

The rapid homogenization of the solution promotes faster hydrolysis by allowing greater contact between the reactants. However, alcohol in excess of that needed for complete mixing slows down the condensation reaction by diluting the reactants and by competing for the active silanol sites (re-esterification). This is seen most clearly in the acid catalyzed (condensation limited) sols such as those employed in Chapters 5 and 6.

2.2.5 Gelation

The gelation process is usually pictured as a cluster growth phenomenon. Clusters grow by polymerization or the aggregation of particles followed by cluster-cluster linkages which eventually lead to the formation of a giant spanning cluster which fills the container. This imparts rigidity to the entire mass such that the sol gel no longer pours when it is tipped. At the gel point, the reaction is by no means completed as there remain many unreacted species and unconnected clusters which continue to react, further increasing the rigidity and stiffness to the mass. Theoretically, the sol is gelled when the last link is formed creating the spanning network. However, the wide variation in the rates of gelation under different conditions make it difficult to determine an exact point of gelation.

The first theory used attempting to describe the gelation process of silica sols was the Flory-Stockmeyer (FS) model borrowed from polymer chemistry (Flo53). In this model, bonds are randomly formed between adjacent nodes on an infinite Cayley tree (or Bethe lattice). The Flory-Stockmeyer model successfully predicts the emergence of an infinite cluster at some critical point but when applied to silicon alkoxide derived sols fails to account for cyclical species which are very prevalent in acid catalyzed reactions. This deficiency in turn, leads to the prediction of a fractal dimension of 4 resulting in a divergent density for large clusters (Bri94). Percolation theory, as developed by Stauffer et. al., allows for cyclic molecules and better describes the aggregation of both particles and polymers far from the gel point (Sta82). As clusters grow, their density decreases as 1/r and their volume fraction increases. Structural properties in the vicinity of the gel point agree much more closely with that predicted by percolation theory than classical FS theory. Brinker and Scherer describe in greater detail the application of these two theories to gelation in their book Sol Gel Science (Bri90).

Gelation can be viewed as a process by which connectivity throughout the sol increases through the linking of larger and larger clusters until one giant "spanning" extends across the entire vessel. The determination of the gel point is an important aspect of sol gel chemistry. As previously mentioned the gel point is often used as a measure of condensation kinetics and represents a critical point in the overall structural evolution of the gel. Consequently, many attempts have been made to define the gel point through rheological means (See for example, Sacks and Sheu (Sac87)). As the sol nears the gel point viscosity increases rapidly and the gel transforms to elastic behavior. Viscoelastic definitions of the gelation point tend to fall short in practical terms due in no small part to the wide variation in the rates of gelation of different systems (from a few seconds to several months) and the difficulty in measuring the viscosity of a gel near the gelation point.

Perhaps the best practical determination is also the most obvious. The gel point can be most simply defined as the point at which the meniscus of a sol in a container no longer remains horizontal when the container is tilted. This definition is well suited to sols which gel within a reasonably short period of time (e.g. a few days) and under most conditions is easily applied.

2.2.6 Aging and Syneresis

NMR and Raman spectroscopy have shown that condensation reactions continue for a long time after gelation as the remaining silicate species continue to react. Polycondensation continues until both free reactive species and reactive sites on the gel network are depleted (Zer86, Orc88). Kelts et al used Si^{29} NMR to demonstrate that a substantial number of Q^2 species remain at gelation and decrease with time. There is a concurrent increase in Q^3 and Q^4 species during aging. (Where Q^n represents a Si atom bonded through n siloxane bonds to other Si atoms.) Thus reactive terminal silanols that are in close proximity reorient and react with one another to form additional network connections (Kel86). As these reactions continue, the network begins to shrink resulting in the expulsion of liquid from the pores, a process called syneresis. The shrinkage of the gel, in turn, brings additional terminal groups into proximity which then react to perpetuate the shrinkage until the network stiffens sufficiently to resist further syneresis. The rate and extent of shrinkage depends on several factors including the density and strength of the original network, the concentration of remaining reactive groups, temperature, the chemical environment, pore structure and even the size of the gel. The rate of syneresis decreases with time as the gel stiffens and the remaining reactive groups are depleted.

At a pH of 2, near the IEP of silica, syneresis is shown to be at a minimum (Vys73). Presumably this is because the uncharged nature of the silica surface at the IEP results in a slow condensation rate (Bri90). This points toward condensation as being the major driving force in syneresis. It has long been known that the rate of shrinkage during syneresis is slower for large gels than small ones. Scherer proposed that as a gel shrinks it creates a compressive load that forces liquid out of the pores. Due to the short diffusion distances, small gels offer less resistance to the escape of the liquid whereas large gels require a steep pressure gradient to force the liquid through the (much longer) network to the surface (Sch92). Syneresis can therefore be viewed as a competition between those forces promoting shrinkage (condensation and consolidation) and those resisting shrinkage (the stiffness of the network, the pressure required to force out the liquid, and depletion of reactive species). Although there are numerous factors, Brinker concludes that, in general, the rate of shrinkage decreases primarily due to the stiffening of the network rather than the depletion of reactive groups (Bri90).

Concurrent with continued polycondensation and syneresis, coarsening or "Ostwald ripening" occurs during aging. This irreversible process occurs through the preferential dissolution of high energy convex surfaces followed by deposition in regions of negative curvature. Thus necks begin to form between primary particles and small pores are filled in at the expense of larger pores. Although coarsening can retard syneresis through the stiffening of the network, it normally does not have a large effect as it is slow relative to those processes contributing to gel shrinkage. Over time however, and particularly at elevated temperatures, coarsening has a marked effect on the pore structure of the gel. As one might expect, coarsening of the gel is dramatically affected by the solubility of silica and is most pronounced at high pH and at higher temperatures.

Alkaline conditions during aging typically decreases the specific surface area dramatically and slightly increases the pore volume. The average pore radius (hydraulic pore radius) increases markedly, primarily due to the lower surface area (Liu92). HF or strong acids can also promote aging with similar results (She65). HF has long been known to dissolve silica through the effectiveness of the F^- ion in breaking siloxane bonds.

The solubility of silica also rises significantly at very low pH albeit not as dramatically as with strong alkalis. Thus coarsening takes place across the spectrum of pH.

Though often overlooked, aging continues during the drying process and can dramatically change the pore structure due to the effects of long drying times, high temperatures and changes in solvent composition. In the production of large silica gel monoliths this is particularly important as drying times must be extended to produce crack free pieces. A large monolith dried over several weeks can produce a pore size 50% greater than a small monolith of the same composition dried in 48 hours. Note also that as a gel dries the solvent composition changes as the more volatile components (normally the alcohols) evaporate first. Thus the solubility of silica increases due to both the higher temperature and a greater percentage of water.

2.2.7 Drying

If monolithic dried silica gels are desired the drying is the most critical and difficult process in their production. This is because the capillary stresses induced by the emptying of the pore network generally result in cracking of the gel unless the conditions and rate of drying are very carefully controlled. Scherer divides the drying process into three stages, the constant rate stage, first falling rate period and second falling rate period (Sch86). These three stages are illustrated in Figure 2.13 by the drying data of an alumina gel studied by Dwivedi (Dwi86).

2.2.7.1 Constant Rate Period

In the first stage the gel network shrinks as the liquid evaporates from the surface. As the name implies, the evaporation per unit area is relatively independent of time. The

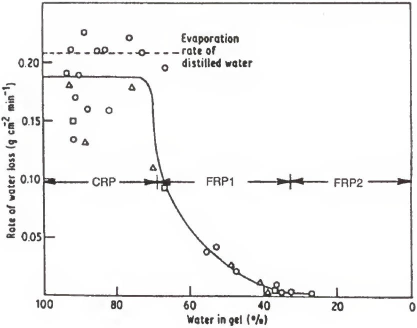

Figure 2.13. Rate of water loss from an alumina gel illustrating the Constant Rate Period (CRP), First Falling Rate Period (FRP1) and Second Falling Rate Period (FRP2) (Dwi86).

forces causing the shrinkage of the gel depend on the liquid vapor surface tension. As the liquid evaporates menisci begin to develop at the surface. Consequently, the liquid is subjected to a tensile stress P given by:

$$P = \frac{-2\gamma_{LV}}{r_m} \qquad [2.5]$$

where γ_{LV} is the liquid/vapor surface tension and r_m is the radius of curvature of the meniscus. (The radius of curvature is defined as negative when the center of curvature is outside of the liquid.) The tension in the liquid is balanced by a corresponding compressive force on the gel network which contracts to prevent the exposure of the solid phase. Thus the liquid-vapor interface remains at the surface of the gel and the rate of liquid loss is substantially constant as the gel shrinks in response to fluid evaporation. The total volume of liquid lost is equal to the decrease in the volume of the gel. As the gel contracts compressive forces eventually build up until the body becomes stiff enough to prevent further shrinkage. This is the end of the constant rate period and the beginning of the first falling rate period, which is characterized by the pores beginning to empty from the surface inward. (See Figure 2.14.)

2.2.7.2 Critical Point

The point at which this transition occurs has variously been called the leatherhard point or the critical point. The latter term is most descriptive in that it is at this point that cracking is most likely to occur. In order for the liquid to penetrate the pores, the radius of the meniscus must equal $r_p/\cos\theta$. This is the point at which the liquid exerts the maximum force on the network

$$P = \frac{-2\gamma_{LV}\cos\theta}{r_p} \qquad [2.6]$$

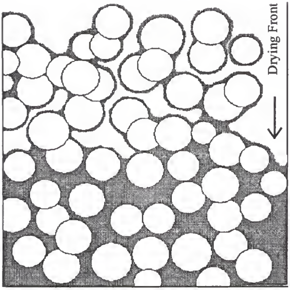

Figure 2.14. Schematic of the first falling rate period. Gel begins to turn opaque as the drying front penetrates the gel.

where θ is the contact angle and r_p is the pore radius. Visually, the onset of the first falling rate period is often recognizable by the appearance of cauliflower-shaped opaque regions which form in areas where isolated pockets of pores remain filled with liquid longer than their surroundings. These opaque areas usually (but not always) progress from the exterior of the gel to the interior until the entire gel is opaque.

2.2.7.3 The First Falling Rate Period

After the critical point, further evaporation drives the meniscus into the body. During the first falling rate period the rate of evaporation decreases as liquid must find its way from the interior of the gel to the surface. The surfaces of the pores that have emptied retain a contiguous film of liquid, a condition referred to as funicular. (See Figure 2.15.)

There are two possible mechanisms by which liquid transport occurs, diffusion of vapor from the remaining filled pores through the empty network to the surface, and fluid flow along the funicular surface. According to Brinker (Bri90), it is generally conceded that the latter mechanism is responsible for the bulk of liquid transfer during this stage of drying. Evaporation occurs at the outer surface due to the lower relative humidity. This creates a gradient in capillary stress from the interior to the exterior surface where the tension of the liquid is the greatest. Liquid therefore flows along the funicular layer according to Darcy's law in which the flux of liquid is proportional to the gradient in pressure in the liquid.

$$J = \frac{-D}{\eta_L} \nabla P \qquad [2.7]$$

The flux, J, is in units of volume per unit area of funicular layer per unit time (m/sec), P_L is

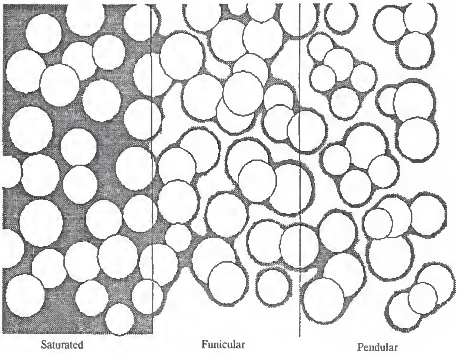

Figure 2.15. Funicular and pendular states in a porous body.

the force per unit area of the liquid (Pa), η_L is the viscosity of the liquid (Pa-sec), and D is the permeability and has units of area (m^2). It is interesting to note that the properties of the funicular layer (normally water) have been shown to be significantly different than those of the bulk solvent (Isr85).

2.2.7.4 Second Falling Rate Period

As the distance from the surface of the gel to the drying front increases the pressure gradient and hence the flux of the liquid decreases. (This is another reason why large gels take longer to dry.) The liquid nearest the exterior of the body eventually begins to enter the pendular state, that is; where the continuity of the surface layer is disrupted forming isolated pockets of liquid. Since the liquid can no longer flow along a continuous path to the surface, it can only migrate to the surface through vapor diffusion.

In very small pores this diffusion is of the Knudsen type where the water molecules collide more frequently with the walls of the pores than with each other (Kau66). Knudsen diffusion is also associated with a reduction in thermal conductivity of the gel. This combined with a low bulk density is what makes aerogels such excellent insulating materials. Exacerbating the reduction in diffusion rate is the strong interaction of the polar water molecules with the highly hydroxylated surface of the pore wall (Suz87). The slow diffusion of vapor through the pore network causes an abrupt decrease in the drying rate which is indicative of the beginning of the second falling rate period.

2.2.7.5 Cracking in Gels During Drying

During the constant rate period the evaporation of liquid causes the network to be compressed as the tension in the liquid increases at the surface. The higher tension at the surface also is responsible for the flow from the interior. In order for the meniscus to remain at the surface, the rate of evaporation ,V_e, must equal the flux of the liquid to the surface given by Darcy's Law:

$$J = \frac{-D}{\eta_L} \nabla P = V_e \qquad [2.7]$$

The lower the permeability, D, the greater the pressure gradient must be to maintain a given evaporation rate. One of the reasons gels are difficult to dry is that the permeability of the gels is usually very low (because of the small pore size), so rapid drying rates produce very steep pressure gradients. The high rate of evaporation (and hence higher tension) of the liquid near the outer surface makes that portion of the network shrink faster than the interior. The steeper ∇P, the greater the difference in shrinkage rate between the exterior and interior, and the more likely the gel is to fracture (Bri90). For the larger pore gels in this study, the greatest propensity for cracking occurs at or just after the critical point (or sometimes during the first falling rate period). It is at this point that the pores begin to empty. Logically, the maximum pressure differential possible is that between an empty pore and a filled pore at the critical point. Here the liquid is under maximum tension and the empty (funicular) pore under none. Therefore as the pores empty the boundary between the empty (funicular) and filled pores creates a stress maximum which can result in the failure of the gel. This stress maximum transits the gel as it empties. In larger pore gels the boundary can be observed by watching the progression of the opaque stage as it travels through the gel. Chapter 6 shows that the rate at which the drying front transits the gel also plays a role in the failure of gels.

2.2.8 Surface Chemistry and Water

In sol gel chemistry the properties of amorphous silica products are greatly affected by the amount and distribution of chemically and/or physically bound water remaining in the product. Water can be retained in silica either in the bulk or on the surface as silanol groups or as physically adsorbed water. The latter tends to be restricted to the surface of the silica and is generally removed by heating in the vicinity of 180°C. Chemisorbed water in the form of surface silanol groups is more persistent and some remains even at high stabilization temperatures. Silanol groups exist in several configurations depending on their location and coordination with other silanols. They can exist as:

> *single silanols* (Q^3) on silica tetrahedra with three siloxane (Si-O-Si bonds).
>
> *geminal silanols* (Q^2) - two silanols connected to the same silica tetrahedra with the remaining two silicon bonds of the siloxane type.
>
> *vincinal silanols* - two silanols (single or geminal) on adjacent silica tetrahedra and hydrogen bonded to one another.
>
> *structurally bound* - or internal silanols retained in the silica bulk.
>
> *silane triols* (Q^1)- postulated and obviously exist at least in a transitory state during condensation and dissolution processes but unverified as a stable surface feature (Berg94a).

The surface silanol groups are the main features of a hydrated silica surface and are responsible for the hydrophilic nature of most silica gels and the colloidal properties of silica powders. (See figure 2.16.) The relative abundance of surface silanol groups depends primarily the degree of hydroxylation of the silica surface. Zhuravlev measured the surface silanol concentrations of a variety of different types of amorphous silica using deuterium exchange and determined the average silanol concentration (α_{OH}) on *fully hydroxylated* surfaces to be 4.9 silanols/nm^2 (Figure 2.17). Measurements by other authors are in substantial agreement with this number. The narrow range of experimental values suggests that this figure is relatively independent of type and history of the amorphous silica. It is also approximately the same as the number of sites available on the

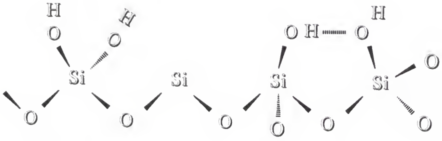

Geminal Silanols (Q^2)

Vincinal Silanols

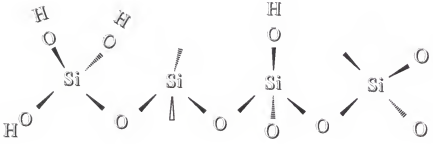

Silane Triol (Q^1)

Isolated (single) Silanol - (Q^3)

Figure 2.16. Different types of silanol groups on the surface of hydroxylated silica.

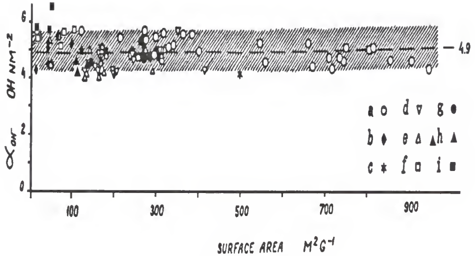

Figure 2.17. Concentration of silanols on the surface of various forms of silica (Zhur87).

(111) surface of cristabolite which has a density and refractive index similar to amorphous silica (Iler79).

As the silica surface is heated, the water content decreases steadily with increasing temperature. Physically adsorbed water is removed at temperatures between 150° and 200 °C at which point the silica surface consists only of silanol groups and surface siloxane bonds. With increasing temperature vincinal silanol groups condense to form strained siloxane bonds. At 450°-500°C the vincinal silanols are gone and the surface consists of single and geminal silanols and strained siloxane bonds. Bergna estimates the ratio of single to geminal silanol groups at this point to be 85:15 (Berg94). Strained siloxane bonds are primarily made up of three membered ring structures and are rapidly rehydroxylated upon exposure to water (Bri88). Thus, up to this point, the dehydroxylation of the surface is considered to be reversible. Above 500°C the strained siloxane bonds begin to relax to form stable siloxane groups (Hen90). Stable siloxane surfaces can also be rehydroxylated albeit much more slowly due to the much higher activation energy required to break the unstrained siloxane bond. The hydrolysis rate of an unstrained four membered ring is approximately 100 times slower than that of a three membered ring (Bri90). As silanols react to form siloxane bonds, the surface becomes progressively more hydrophobic in character.

2.2.9 Stabilization and Densification

Stabilization of a porous silica gel involves reducing the concentration of silanol groups on the surface to the point where rehydroxylation is inhibited. The purpose is to prevent the porous body from readsorbing water or other atmospheric contaminants which can degrade its performance or (in the case of monoliths) result in structural failure. This is normally accomplished through thermal and/or chemical treatments that remove silanols and create a less reactive surface. As the name implies, thermal stabilization consists of heating the silica gel to continue the removal of surface silanol groups. As previously mentioned heat treatments below about 500°C result in surfaces that are easily rehydroxylated. Above 500°C structural relaxation and the increasing elimination of isolated silanol groups produces a surface that becomes progressively less hydrophilic and progressively more difficult to rehydroxylate. Zhuravlev (Zhur94) summarized this process in terms of the fraction of available sites occupied by silanols as follows:

> 1. The temperature threshold corresponding to the removal of physically adsorbed water from the hydroxylated SiO_2 surface lies at 190°C.
>
> 2. The maximum hydroxylated state of the surface of SiO_2 samples is approximately one OH group per Si atom. This equates to an average value of the silanol number (α_{OH}) of 4.6 OH groups per square nanometer. This is a physiochemical constant independent of the type of the amorphous silica used, the method of preparing it, and the structural characteristics.
>
> 3. The kinetic order of the thermal desorption of water in the range 200 - 1100°C requires the pair wise reaction of hydroxyl groups to form siloxane bonds. The degree of coverage with silanol groups, θ_{OH} , in this temperature range varies from 1.0 to ~0.
>
> 4. Over the range $1.0 \geq \theta_{OH} > 0.5$, (corresponding to treatment temperatures of 200 - 500 °C), hydrogen bonding occurs between the OH groups and the activation energy of desorption, E_d, progressively increases from 16.5 to ~25 kcal/mol as the sites become fewer and less favorably oriented. Rehydroxylation, involving the breaking of the siloxane bridges and the formation of new silanol groups, is a rapid non-activated (or weakly activated) process.
>
> 5. As the degree of coverage drops below $\theta_{OH} = 0.5$, the energy of activation, E_d, increases substantially (from ~25 to 50 kcal/mol and probably higher) due to the fact that there remain only isolated OH groups on the SiO_2 surface. In order for the condensation reaction to take place protons must migrate to other active sites resulting in the evolution of H_2O molecules due to the chance interaction of pairs of OH groups. Rehydroxylation of such a surface is a slow and strongly activated process.

6. In addition to surface OH groups, there may exist OH groups inside the silica skeleton and inside fine micropores that have diameters comparable to that of the water molecule. The concentration of such intraskeletal OH groups depends on the method of preparation and subsequent treatment of silica.

Chemical modification of the silica surface by replacing silanol groups with more hydrophobic species is another method of stabilization. For example, fluoride catalyzed gels having a substantial number of silanols substituted by fluoride are less hydrophilic and more stable to atmospheric moisture. Brinker has modified internal pore surfaces by reacting gels with methylated alkoxides to produce hydrophobic surfaces (Bri94).

Densification is brought about by heating the silica to a temperature where viscous flow occurs and the porosity is eliminated to form dense silica glass. As heating continues between approximately 500°C - 1100°C, three processes take place, condensation of silanols with the elimination of water, structural relaxation, and viscous sintering. The first two result in skeletal densification (the structural density of the solid phase of the porous gel) and surface modification. The third results in pore closure and consolidation.

Condensation reactions and the elimination of water continue throughout the process as isolated silanols come into proximity with each other and sufficient activation energy is provided. This occurs only slowly as it is postulated that it requires the diffusion of protons along strained siloxane bonds until an adjacent pair of silanols is formed at which point they condense to form water (Iler79). As the process continues it becomes progressively more difficult for isolated silanols to cover the diffusional distances necessary to react with one another. Additionally, the water must diffuse out of the pore network before it is eliminated entirely. During this process it can recombine with the surface to form silanols. This is one reason why it is impossible to completely eliminate water from the glass by thermal treatments alone.

Structural relaxation begins at about 500° - 600°C and continues throughout the sintering process. The degree of skeletal densification that takes place at intermediate temperatures depends on the starting structural density which can vary from 1.7g/cm^3 for an acid catalyzed TEOS derived gel, to 2.08 g/cm^3 for a base or fluoride catalyzed gel (Hen90b). Elimination of water and relaxation drive the skeletal density toward the equilibrium value of 2.20g/cc for pure silica. At about 800°C viscous sintering commences and continues up to 1100°C, the glass transition temperature for silica. The process of viscous sintering is driven by the reduction of interfacial energy (Sch87). Material moves by viscous flow to reduce the solid vapor interface; pores shrink and are eventually eliminated.

The viscosity of the glass is not constant in most gels but increases as the water content decreases (increasing structural density). Therefore as sintering occurs there is a corresponding increase in viscosity as water is liberated. Therefore, the rate at which sintering occurs is dependent on the pore size, surface area of the gel, and the viscosity; which in turn, depends on the temperature and the amount of water remaining. Acid catalyzed gels characterized by small pore sizes, high surface areas, low skeletal densities and high water content, begin to sinter in the vicinity of 800°C. Coarser particulate gels with high structural density, large pore sizes and low surface area and less water content may not sinter substantially until 1100°C. A rapid heating rate can actually promote densification at lower temperatures due to the lower viscosity effected by a higher water content. This is particularly true in gels with high surface areas and consequently high percentages of chimisorbed water. Lower rates of heating provide more time for water elimination but can increase the temperature required for full consolidation. In practicality the slower rate of heating is preferred since hydroxyl groups that remain in the silica after pore closure can subsequently form water vapor bubbles in the glass, a phenomena known as bloating.

Bloating is a serious problem in the densification of microporous, high surface area gels. Consequently, attempts have been made to reduce the water content of silica gels through a variety of dehydroxylation treatments (Berg94a).

2.2.10 Dehydroxylation Treatments

Thermal dehydroxylation of gels can eliminate bloating and result in clear monoliths but are limited in the amount of water that can be removed. Williams et. al. succeeded in reducing the water content in a borosilicate glass by using extremely high vacuum and holding the gels to just under the sintering temperature for a time (Wil76). Water contents as low as 95 ppm have been achieved by this method.

The propensity towards bloating is not the only reason to eliminate water from dense silica. Optical applications involving transmission in the ultraviolet and infrared require very low levels of retained water, sometimes as low as ppb in some fiber optic applications. Thermal treatments, even under high vacuum, are insufficient to reduce water content to meet these stringent requirements. Chemical dehydration treatments primarily with halogens, can be applied to porous silica during heating to eliminate hydroxyl groups on the surface (Bri90).

The most common dehydrating agents are chlorine containing compounds such as methylated chlorosilanes, carbon tetrachloride or chlorine gas. Dehydroxylation by chlorine relies on the decomposition of the chlorine containing gas to produce chlorine radicals which react with silanol groups to form hydrochloric acid. HCl diffuses out through the pores. By 800°C all of the silanols are replaced and sintering can proceed to full density without the evolution of water. Samples treated with chlorine dehydroxylation agents typically reach full density at higher temperatures than similar untreated glasses due to an increase in viscosity as water is removed (Hen90b).

Figure 2.18 shows the transmission spectrum for commercial Gelsil™, a dense gel-derived, optical glass having undergone chlorine dehydroxylation. Chlorine treated silica retains up to 2% chlorine and although this improves the optical properties dramatically by eliminating water, it can present other problems. In the optical fiber industry, for example, silica preforms must be heated to softening temperature in order for fibers to be

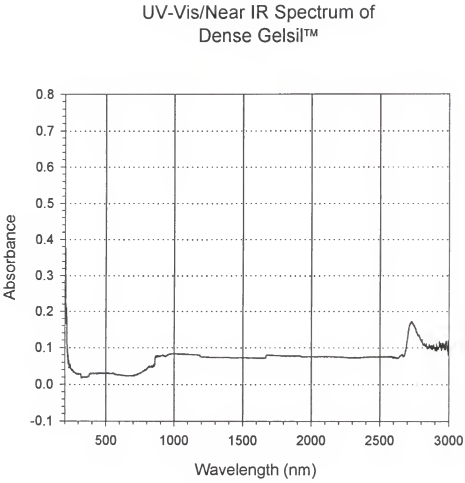

Figure 2.18. UV-Vis-NIR spectrum of dense Gelsil®. The ultra-low water content is a result of chlorine dehydroxylation during sintering.

Gelsil®- Registered U.S. Trademark , Geltech Inc., Orlando Florida.

drawn. Chlorine treated glasses can reboil or foam under these conditions as chlorine gas is generated -- much in the same way water does in hydroxylated glasses. Chloride foaming can be eliminated by replacing chloride with fluoride as the dehydroxylation agent (Rab86).

Fluorine can be introduced by treatment with HF or SiF_4 gas or can be incorporated into the solution in the form of HF, H_2Si_6, NH_4F or alkali fluorides. (The latter also introduces modifiers into the glass). The foaming problem associated with reheating the chlorine treated glasses is eliminated due to the stronger Si-F bonds. Rabinovich has demonstrated that where as little as 0.3% of chlorine results in reboil upon reheating, up to 2% F can be incorporated in silica without encountering this problem. Fluoride is also one of the few additives that can lower the refractive index of silica and thus has generated interest as a cladding material for fiber optic waveguides. (Rab86) Care must be taken in the treatment of porous gels with fluoride as the dehydration agent due to the dangers in handling most fluoride compounds. Additionally, as will be seen in Chapter 4, fluoride will attack siloxane bonds in both solution and in the gaseous state. This facilitates its incorporation into the glass but it is strictly a surface phenomena. Thus it is difficult to incorporate large amounts of fluoride in gel derived glasses.

2.3 Aerogels

Since the subject of this dissertation deals primarily with a system of relatively low density (0.45g/cc) xerogels it is appropriate to briefly mention a few words about aerogels. Aerogels are produced by a sol-gel process substantially identical to the one just described up to the point of drying the gel. Whereas xerogels are normally dried under ambient pressures at elevated temperatures, aerogels circumvent the problem of capillary stresses by using supercritical drying techniques (Fri86). They are generally characterized by low densities and high surface areas. Although aerogels are defined as silica gel bodies that have been supercritically dried; many authors categorize silica gels by their properties calling very low density gel an "aerogel" regardless of its method of manufacture. Some are transparent some are not. Since supercritical drying is a somewhat cumbersome and expensive method of drying gels, research continues towards the development of ambient dried low-density xerogels that have properties more typical of aerogels.

2.3.1 History

Aerogels were first prepared by Steven S. Kistler in 1931 from colloidal gels prepared by the acidic condensation of sodium silicate (Kis31). Discovering that water dissolved the gels under supercritical conditions, Kistler replaced pore liquor with methanol and successfully extracted the supercritical solvent at a temperature of 242°C and a pressure of 1600 psi. The process was commercialized by Kistler at Monsanto Corporation and the resulting product used as an additive or thixotropic agent in cosmetics and toothpaste. Little advancement in the field occurred over the ensuing 30 years. In 1968, a French team led by S. J. Teichner successfully applied Kistler's technique of supercritical drying to a TMOS derived silica gel. This greatly simplified the process of solvent exchange, eliminated alkali impurities and provided more control over the texture and homogeneity of the product. Thus the availability and use of metal alkoxides in sol gel science led to a concurrent resurgence in interest in aerogels which has continued to this day.

The first modern application of aerogel technology was in Cherenkov radiation detectors for high-energy physics experiments. Aerogels can be made with densities ranging from a low of 0.003g/cc to about 0.5g/cc. The low density and transparency of the aerogels resulted in refractive indices near n=1, a prerequisite for the detection of some types of subatomic particles. Additionally, the ultra low thermal conductivity and transparency of low density aerogels shows great promise in their use as thermal insulation. With typical thermal conductivities of 0.017W/mK (R10/inch) transparent aerogels have been investigated as a filler for insulating windows (Hun85). Aerogels doped with carbon black and other additives have demonstrated even better thermal insulation. The recent “Sojourner” mission to Mars makes use of aerogel insulation to reduce weight and protect the rover from temperature extremes (Hov97). The first commercial attempt to produce aerogels in quantity ended in disaster in 1984 when a 3000L autoclave in Sjobo, Sweden developed a leak resulting in an explosion which obliterated the facility (Fri86). It was clear that improvements in both safety and production costs were necessary. In the 1980’s, Arlon Hunt et al.from Lawrence Berkeley Labs pioneered the use of pressurized (liquid) carbon dioxide to replace methanol as the liquid phase. After replacing the solvent with non-flammable CO_2 they found that the gels can be supercritically dried under milder conditions (40°C and 1200 psi) with a commensurate reduction in the hazards and environmental impact (Tew85, Tew86).

2.3.2 Structural Characteristics

The structural characteristics of aerogels can be examined with many of the same techniques used for conventional xerogels. However due to the extremely low density and consequent low strength of the materials several common techniques for probing pore and particle size are of limited value. The most common technique for elucidating surface area and porosity, Nitrogen adsorption, gives the specific surface area of aerogels in the range of about 400 - 1000 m^2/g and porosities on the order of 86 - 97% (Fri87). However for gels containing pores larger than about 1000Å in diameter, BET cannot provide reliable pore volumes, thus the nitrogen adsorption derived porosities and average pore sizes must be confirmed with other methods (Gros88). Due to the low compressive modulus of most aerogels, mercury porosimetry results in compression of the gel without penetration of the mercury (Smi95). Skeletal densities range from 1.70 to 2.10g/cc (fused silica is 2.20g/cc) indicating either hydration of the surface, a micro porous silica backbone or longer average bond lengths (Bro86). Electron micrography has provided some informative imaging but care must be taken to avoid sintering of the gels by the electron beam, even at low current. Small angle X-ray scattering (SAXS), neutron scattering (SANS) and light scattering have been relatively successful in determining structural parameters such as fractal dimension, size of the smallest building block and correlation lengths. The surface of aerogels tends to be covered with methoxy groups when supercritically dried in methanol while silanol groups are more prevalent in the CO_2 dried samples (Hus95). The Young's modulus of low density aerogels can be up to four orders of magnitude smaller than fused silica.

2.4 Summary

The sol gel process offers a wide variety of methods for the fabrication of porous siliceous materials. There are several steps in the process including selection of raw materials, formulation, aging, drying and sintering. By manipulating these various steps, a wide variety of porous gel glasses can be produced. With a firm understanding of chemistry and physics of these processes, gel texture can be tailored to specific tolerances on a nanometer scale. The physical, chemical and optical properties of these materials are giving scientists and engineers a variety of new options in the development of advanced materials and new technologies.

CHAPTER 3

NITROGEN ADSORPTION FOR SURFACE AREA AND POROSITY DETERMINATION

Nitrogen adsorption works on the principle of adsorbing a measured quantity of gas on the surface of a sample at a given temperature and pressure to determine the amount of surface area and in some cases porosity of the sample. It had been known early in the 19th century that certain porous surfaces such as charcoal, could adsorb several times its own volume of various gases (Gre82). This physical adsorption, of gas (adsorbate) on a surface (adsorbent) is dependent on the intermolecular forces between the selected gas and the surface which is under study. These are the same intermolecular attractive and repulsive forces that are responsible for the condensation of gases at low temperatures and high pressures as a consequence of deviations from the ideal gas law.

London's dispersion forces arise from the polarizability of atomic or molecular orbitals surrounding molecules. As fluctuations in electron charge distribution occur in an atom, the resulting electronic field induces or polarizes nearby electron clouds in the opposite direction resulting in a net attraction. If the species possess a dipole moment, dipole - dipole interactions also contribute to the attractive force. The combination of these forces is sometimes referred to as Van der Waals interactions named after Johannes Van der Waals who first attempted to develop an overall description of molecular interactions in gases. Ionic forces are present in charged species but are not ordinarily a factor in gas adsorption. Short range repulsive forces counterbalance dispersion forces and are caused by electrostatic repulsion between electron clouds as they approach one another.

The interaction forces between an adsorbate and surface give rise to the formation of a condensed layer which becomes thicker as the pressure increases towards the saturation pressure of the adsorbate. Nitrogen at its boiling point (77.4K) has a saturation pressure of one atmosphere. The weight of the condensed layer(s) is derived from the volume of adsorbed gas and is used to determine a variety of information concerning the nature of the surface. BET theory was developed by and named for Brunauer, Emmet and Teller due to their pioneering work in the field dating back to the 1930's (Bru40). Modern derivations of the theory provide information concerning the surface area, pore volume and pore size distribution of a powder or porous solid.

3.1 Surface Area--The BET Method

This is the most widely used procedure for the determination of surface area of a solid. It is based on the equation

$$\frac{1}{W[(P_o/P)-1]} = \frac{1}{W_m C} + \frac{C-1}{W_m C}(P/P_o) \qquad [3.1]$$

where W is the weight of gas adsorbed at a relative pressure of $\frac{P}{P_o}$ and W_m is the weight of the adsorbate constituting a monolayer of adsorbed gas. C is called the BET constant and is related to the attractive forces between the surface and the gas. For most solids plotting $\frac{1}{W[(P_o/P)-1]}$ vs $\frac{P}{P_o}$ usually results in a straight line in the region from $.05 < \frac{P}{P_o} < 0.35$. The slope (s) and the intercept (i) of this line can be used to calculate W_m, the weight of the monolayer of adsorbate.

$$s = \frac{C-1}{W_m C} \qquad [3.2]$$

$$i = \frac{1}{W_m C} \qquad [3.3]$$

$$\Rightarrow W_m = \frac{1}{s + i} \qquad [3.4]$$

Given the weight of the monolayer of adsorbate, the surface area of the sample can be calculated using the equation:

$$S_t = {}^{W_m N A_{cs}}\!\!\Big/_{M} \qquad [3.5]$$

where N is Avogadro's number, A_{cs} is the cross sectional area of the adsorbate molecule, and M is the molecular weight of the adsorbate. Nitrogen, the most widely used adsorbate, has a cross sectional area $A_{cs} = 16.2$ Å^2 in a hexagonal close packed arrangement at 77K. Surface areas for solids are usually reported as the specific surface areas, that is, the surface area per gram of sample.

$$S.A. = \frac{S_t}{w\ (\text{grams})} \qquad [3.6]$$

The C constant in the BET equation is related to the interaction between the solid and the adsorbate. Its magnitude can be an indicator of the reliability of the BET data. Low values for C (<50 in the case of silica) indicate lower attraction between adsorbate and the surface. This can lead to multilayer formation before the monolayer is complete and consequent inaccurate surface area approximations. The C constant can be calculated from the slope and intercept of the BET curve (Gre82).

$$C = ({}^{s}\!/_{i}) + 1 \qquad [3.7]$$

3.1.1 Porosity by Gas Adsorption

When analyzing porous materials by gas adsorption pores are generally classified by their diameters. Pores with diameters in excess of 500Å are called "*macropores*". Those with diameters between 20Å and 500Å are termed "*mesopores*" and pores with diameters less than 20Å are "*micropores*". The porosity and pore size distribution of a porous solid are analyzed by adsorbing nitrogen over a range of relative pressures up to the limiting P/Po ratio of 1.0. The total adsorption of nitrogen at a P/Po approaching unity represents the total pore volume of a porous solid.

3.1.2 Adsorption Isotherms

Much information regarding the porosity and surface area of a solid can be gleaned by inspecting the adsorption isotherm. The isotherm is so named because it represents the volume of gas adsorbed at a constant temperature over a range of relative pressures, P/Po. In the case of nitrogen, the solid is placed in a glass tube and immersed in a bath of liquid nitrogen to control the temperature at 77.4K. The pressure above the solid is then regulated by adding or removing gaseous nitrogen until the desired equilibrium pressure is reached. Plotting the quantity of adsorbed gas versus the equilibrium pressure yields the characteristic isotherm for the solid. All isotherms tend to fall into five general types as characterized by Brunauer, Deming, Deming and Teller in 1940 (Bru40). These categories are shown in Figure 3.1.

The *Type I* isotherm, or Langmuir isotherm, is concave to the P/Po axis over its entire span and approaches its limiting value as P/Po approaches 1.0. Type I isotherms are characteristic of microporous solids having a relatively small external surface. Examples of solids giving type I isotherms include activated carbons, molecular sieve zeolites and, as we shall see, some types of silica gels.

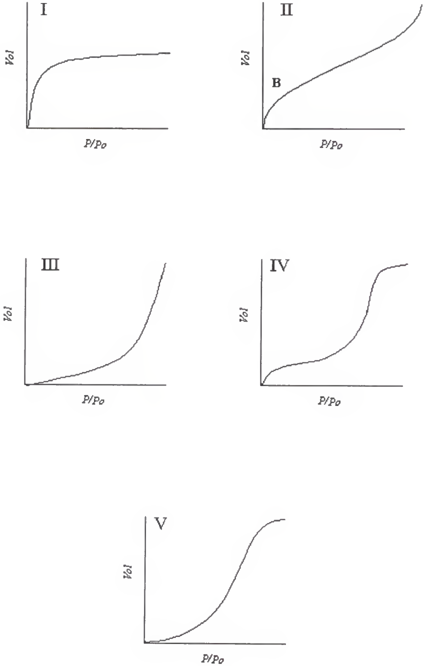

Figure 3.1. The five types of isotherms as classified by Brunauer, Deming, Deming, and Teller (BDDT) (Bru40).

Type II isotherms are exhibited by non-porous or macroporous solids. This type of isotherm represents unrestricted surface adsorption beginning with a monolayer and progressing to multilayers at higher P/Po. Characteristic of the type II isotherm is an inflection point "B" marking the start of a linear central section of the isotherm. This point usually marks the relative pressure at which the monolayer is complete and multilayer adsorption begins.

The *Type III* isotherm is convex to the P/Po axis and has no distinct point B as in the type II. This is representative of a material where the solid-adsorbate interactions are weaker than the adsorbate-adsorbate interactions. This type of isotherm is rare but one example is the adsorption of water vapor on nonporous hydrophobic carbons.

Type IV isotherms are indicative of mesoporous materials. The steep slope at higher relative pressures is associated with capillary condensation in the pores.

Type V isotherms are similar to type III but have mesopores. They are also relatively uncommon.

The desorption isotherms for types I ,III, and IV are reversible, that is, they follow the same path as the adsorption isotherm. Types II and V however are associated with mesoporosity and exhibit hysteresis between the adsorption and desorption curves. The hysteresis is associated with the filling and emptying of the mesopores in the material. DeBoer has identified five characteristic types of hysteresis and associated them with pore shape (Debo64). Figure 3.2 shows examples of DeBoer's classification. Typically the hysteresis loops for all isotherms close at or above a relative pressure of P/Po =0.30.

3.1.3 Pore Size Distribution

The distribution of pore sizes in a porous material is determined through the use of the Kelvin equation which relates the radius of curvature of a pore to the capillary

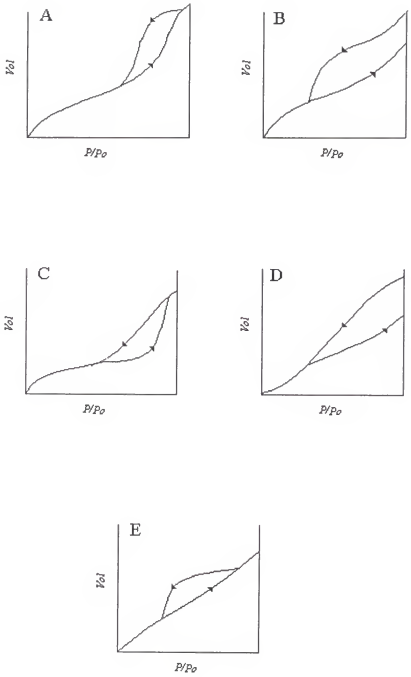

Figure 3.2. DeBoer's five types of hysteresis loops: A. - cylindrical pores; B - slit shaped pores; C - wedge shaped pores with open ends; D - wedge-shaped pores with narrow necks at one or both ends; E - ink-bottle shaped pores.

condensation of liquid nitrogen. The Kelvin equation can be written as

$$r_K = \frac{-2\gamma V_m}{RT \ln(P/P_o)} \qquad [3.8]$$

where

γ= surface tension of nitrogen at 77K (8.85 ergs/cm^2)

V_m= the molar volume of liquid nitrogen (34.7 cm^3/mol)

R = the gas constant (8.314 x 10^7 ergs/deg-mol)

T = boiling point of nitrogen (77.4K)

The Kelvin radius, $r_{K,}$ is the radius of the pore in which condensation occurs at a relative pressure of P/Po. In actuality by the time the relative pressure is high enough to promote capillary condensation, some multilayer adsorption has already occurred on the pore walls. This adsorption reduces the nominal radius of the pore by the thickness of the adsorbed layer. For a monolayer of nitrogen this thickness is 3.54Å. Thus the actual pore radius is the Kelvin radius adjusted by the thickness of the preexisting multilayer on the pore wall:

$$r_p = r_K + t \qquad [3.9]$$

where t is called the statistical thickness of the adsorbed layer. Barrett, Joyner and Halenda developed a method for calculating the pore radius distribution taking into consideration the statistical thickness at the given desorption equilibrium pressure (Bar51). The BJH method is the most common method in use for calculating pore size distributions. The desorption isotherm is normally used for pore size determinations since desorption from mesopores generally occurs at lower relative pressures. It is theorized that the desorption isotherm is closer to thermodynamic equilibrium but as we shall see this is not a simple assumption.

Upon desorption of condensate from a particular pore of Kelvin radius r_K, the volume desorbed consists of the amount emptied from the pore plus the amount of condensate evaporated from the surface of all the pores that have already been emptied. Thus to accurately quantify the pore volume emptied during any incremental decrease in relative pressure, the total area of already emptied pores must be calculated and multiplied by the decrease in statistical thickness over that pressure drop. The BJH method makes use of the following equation to calculate the volume of the emptied pore.

$$V_{pn} = \left(\frac{r_{pavg}}{r_{Kavg}}\right)^2 V_n - \Delta t_n \sum_{j=1}^{n-1} A_j \qquad [3.10]$$

The subscript n in this equation represents the desorption increment being calculated.

V_{pn} = the volume of the current pore increment being emptied.

V_n = the total volume of gas desorbed over increment n.

r_{pavg} = average radius of the pore being emptied.

r_{Kavg} = average Kelvin radius of the pore being emptied.

Δt_n = change in the statistical thickness of the adsorbed multilayer.

A_j = the core area of each pore j emptied prior to the current increment. $A_j = 2V_j/r_{Kavg}(j)$ assuming cylindrical pore geometry.

The incremental volume (Dv) of each desorption step can be plotted against the average pore radius of the interval to yield a graphical representation of the pore size distribution. Since the Kelvin radius is inversely related to the log of the relative pressure, the largest changes in pore radius are measured at higher relative pressures. For example, a relative pressure of P/Po = 0.5 corresponds to a Kelvin radius of 14Å, a P/Po of 0.80 to 42Å, and a P/Po of 0.90 to 90Å as can be seen by the graph in Figure 3.3. Since the volume of a pore scales as the radius cubed, Dv/r or Dv log r is often used to give a more realistic depiction of the proportion of pores of any given radius

In a purely mesoporous material, the average pore radius can be calculated by assuming cylindrical pore shape and using the hydraulic pore radius given by the equation:

$$r_{avg} = \frac{2 \cdot V_p}{S.A.} \qquad [3.11]$$

This equation is not very satisfying since few materials have ideal cylindrical pore shape but is nonetheless useful in making comparisons between materials of similar composition. According to DeBoer's classification of pore shape, a sharp square-shaped hysteresis loop is attributed to cylindrical pores. It should be kept in mind however, that at high relative pressures the adsorbed multilayer will tend to modify the core pore shape into a cylindrical shape as surface asperities are smoothed out. Therefore as irregular pores get larger they tend toward type A (cylindrical) hysteresis regardless of their actual shape.

3.1.4 Microporous Solids

In a microporous solid containing pores no more than a few molecular diameters in width, the potential fields from the surrounding walls overlap. This greatly enhances the interaction energy between the solid and the adsorbate causing increased adsorption at very low relative pressures. Calculations by Gurfein (Gur70) indicate that the enhancement of the energy of adsorption in a microporous material is significant when ratio of the pore diameter to the adsorbate molecule (d_p/d_a) is less than or equal to 3.0. For nitrogen, with a molecular diameter of about 3.5Å, this equates to a pore diameter of

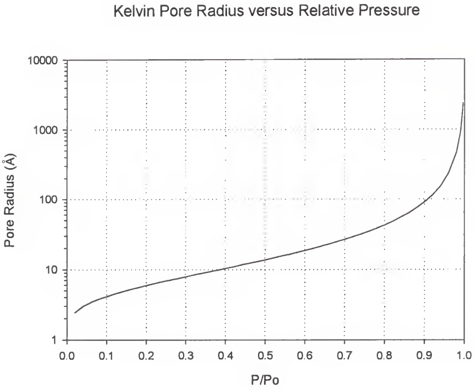

Figure 3.3. The Kelvin pore radius plotted versus relative pressure for nitrogen at 77.4K.

10.5 Å. Sing suggests that cooperative effects such as increased residence time for neighboring adsorbate molecules may raise this value even higher (Gre82). Thus pores in this size regime act much differently than larger pores and have an enhanced attraction for adsorbate. Micropores can be completely filled at very low relative pressures yielding the steep rise and plateau of the Type I isotherm. For microporous materials, the Langmuir equation can be used to calculate the adsorption of a single molecular layer of adsorbate.

$$\frac{W}{W_m} = \frac{C(P/P_o)}{1 + C(P/P_o)} \qquad [3.12]$$

This equation can be rearranged in the form of a straight line.

$$\frac{P/P_o}{W} = \frac{1}{CW_m} + \frac{P/P_o}{W_m} \qquad [3.13]$$

Here the slope $1/W_m$ can be determined by constructing a plot of $\frac{P/P_o}{W}$ verses P/P_o and the area of monolayer coverage calculated by using equations [3.5] and [3.6].

When a material has both micro and mesopores, the characterization becomes more complex. The t-method of DeBoer is useful in differentiating the micropore size and volume in the presence of mesopores (Lip65, DeB65a, DeB65b). The t-plot is a plot of the volume of gas adsorbed versus the statistical thickness of a standard isotherm. The standard isotherm can be derived using either a similar nonporous material or a material with a similar C-constant. For nitrogen and materials with C constants in the range of 50-250, the thickness can be calculated as a function of relative pressure using the following approximation.

$$t(\overset{\circ}{A}) = \left[\frac{13.99}{\log(P_o/P) + .034}\right]^{1/2} \qquad [3.14]$$

This formula calculates the thickness of the nitrogen multilayer as it is deposited at the relative pressure given. For a nonporous material with ordinary surface properties, the t-plot will yield a straight line intercepting the origin with a slope proportional to the surface area (S_t) of the material as depicted in Figure 3.4(a). S_t can be calculated with the following equation:

$$S_t = \frac{V_{ads}^{STP}(15.47)}{t(\mathring{A})} \qquad [3.15]$$

V_{ads}^{STP} represents total the volume of adsorbed gas at the given relative pressure corrected to standard temperature (273K) and pressure (1 atm). The constant, 15.47, is a conversion factor from the gas volume to bulk liquid. In the absence of micropores there is good agreement between the t-method of DeBoer and the BET method of determining surface area. Figure 3.4 illustrates t-plots for materials with different types of pore structure. Figure 3.4(a) shows a t-plot for a dense powder with no porosity. The slope of this plot passes through the origin and like the BET plot, is representative of the total surface area of the material. Microporous materials give a t-plot similar to that in Figure 3.4(b) where most of the adsorption occurs at very low relative pressures and hence the extrapolated linear portion of the plot has a positive intercept on the adsorption axis. Mesoporous materials exhibit a deviation at higher relative pressures corresponding to capillary condensation (Figure 3.4(c)). In Figure 3.4(d) the two linear regions represent the total adsorption at lower t values and the adsorption by micropores at higher t values. Thus the slope of the lower segment represents the total surface area of all pores while that of the upper portion the surface area of micropores only. The intercept (i) of the

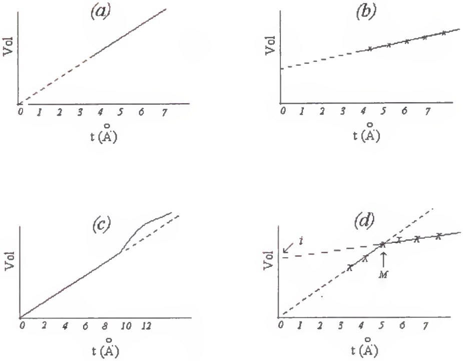

Figure 3.4. (a) t-plot of a nonporous material. (b) t-plot of microporous material. (c) t-plot of mesoporous material. The deviation at high t values indicates capillary condensation. (d) t- plot of a mesoporous material with the presence of micropores. Intercept, i, indicates micropore volume. M indicates radius of micropores.

extrapolated high relative pressure segment, when converted to liquid, is the micropore volume of the material. The intersection (M) of the two straight segments is a good estimate of the size of the micropores. If there is a size distribution of micropores the clean break in the curve will become more rounded. Pores smaller than a radius of 3.5Å cannot be differentiated using the t-plot but their presence may be inferred by the slope of the curve at this point. Slopes which have a positive intercept when extrapolated to cross the adsorption axis indicate such microporosity.

3.1.5 Nonporous Materials

For nonporous powders the surface area can be related directly to the size of the particles if the relative shape factor of the powder is known. For monodisperse spherical powders such as Stober silicas, the relationship is given by:

$$d_P(nm) = \frac{6000}{\rho(g/cm^3) \times SA(m^2/g)} \qquad [3.16]$$

where d_p is the sphere diameter, ρ is the density and SA is the BET specific surface area. For non-uniform powders equation [3.16] must be modified to reflect shape and size distribution which are seldom well characterized. However, comparisons between materials with similar morphologies can help elucidate surface chemistry and thermodynamic properties even when the shape is not known.

3.2 Nitrogen Adsorption Analysis of Silica Gels

Due to its wide variation in surface area and porosity, silica gel has been one of the most thoroughly investigated materials with nitrogen adsorption. It is stable and has a well characterized surface which gives it predictable interactions with nitrogen and other adsorbates. Thus it is a good material for describing the nitrogen adsorption process.

3.2.1 Sample Preparation

The preparation of samples for nitrogen analysis depends to some extent on the type of sample. The sample may be analyzed in bulk or in powder form. For monolithic porous samples it is usually more convenient to grind the sample in a mortar and pestle and analyze it as a powder. The additional surface area introduced by grinding is usually negligible compared to the internal surface area. Sample cells should be tared before introducing the sample. Outgassing is carried out to drive off any adsorbed water in the sample. For silica this can be accomplished by heating to 180° in a vacuum for 12 hours or until the weight stabilizes. It is important that outgassing is completed in a clean environment. Silica gels with small pores are very good "getters" and can absorb organic vapors from the air or from the inside of a dirty vacuum oven. For highly adsorbent samples, care should be taken to minimize moisture absorption when weighing the outgassed sample and during transfer to the instrument. Retained moisture can introduce errors in two ways. It can affect the amount and rate of nitrogen adsorption by blocking small pores or changing the interaction energy between the surface and the adsorbate. This may be reflected in an aberrant C-constant. The second and usually more significant error is in the weight of the sample. The specific surface area and pore volume will be in error in direct proportion to the error in sample weight due to retained moisture.

3.2.2 Interpretation of Results

Care must be exercised in the interpretation of the results of nitrogen adsorption analyses. Modern instrument are getting quite sophisticated and can automatically measure not only the adsorption data but also the density of the sample. For surface area determinations only a few points in the region of P/Po = 0.0 - 0.3 are required. For similar materials a single adsorption point taken at P/Po = 0.3 is often sufficient especially if the C constant is known. The C constant is an important piece of information. For silicas a C-constant of 50-250 is normal. Abnormally low C-constants indicate a low adsorbate-adsorbent interaction energy which can lead incomplete monolayer formation. This invalidates the BET equation which assumes that the monolayer is complete before multilayers form. In particular, surface area analyses with C values that lie below ≈20 should be regarded as questionable. An abnormally high C-constant can be indicative of microporosity in which cooperative adsorption takes place in small pore openings. It may also indicate selective adsorption on particular lattice sites or planes. (i.e. the surface is heterogeneous with respect to the adsorbate). Interpretation of the results from N_2 adsorption is often a simple matter for well behaved powders and porous materials but just as often it requires a bit of sleuthing especially when analyzing a new material.

Special attention should be given to the overall shape of the isotherm and to the C constant. An unexpectedly high or low C constant indicates a deviation from the standard isotherm and can invalidate the results of the analysis.

It is often helpful to reanalyze a sample over a smaller relative pressure range once the region of interest has been identified. For example, a 10 point desorption analysis may show a large Dv between relative pressures of 0.90 and 0.80. These pressures represent Kelvin radii of 89Å and 42Å respectively. All that can be concluded from this information is that pore size responsible for the desorption lies somewhere between these two points. Reanalyzing the sample with more points between these relative pressures enables a more precise estimate of pore size. It also better defines the hysteresis loop in the isotherm which is related to the shape of the pores. This is particularly important in the low relative pressure region for microporous materials and materials with abnormally high (or low) C constants. The BET plot can be nonlinear over the normal range for these materials and the BET range may have to be redefined. Generally, the more points taken in the region of interest, the better.

3.2.3 Adsorbates Other Than Nitrogen

Nitrogen is the adsorbate of choice for most surface area and porosity determinations. For very small (<1 m^2/g) surface areas however, nitrogen is unsuitable due to the narrow range of pressures that comprise the BET region and the magnitude of the correction for the unadsorbed gas over the sample. Over the years a number of other gasses have been considered.

To be suitable for adsorption analysis gases should produce an isotherm with a clear "knee" that is, a clearly definable point B on the type II isotherm. (See Figure 3.1.) This indicates a strong enough attraction between the adsorbate and adsorbent to ensure complete monolayer formation. Adsorbates should also show a relatively uniform attraction for a wide range of materials, be chemically inert towards the adsorbents, have a uniform adsorption cross section and work at a temperature that can be conveniently regulated (e.g. Liq N_2, Liq O_2, CO_2 slush, ice-water, etc.). It should also have a large enough saturation vapor pressure to make measurements over a reasonably wide range of relative pressures. Not surprisingly the Noble gases, specifically argon, xenon and krypton are all good candidates and have been the most widely studied.

The physical properties of argon are not far from those of nitrogen and it is typically used at 77°C. However this is below the triple point of argon (88.8K) leaving a question as to the appropriate reference state (Po). At 77K one would ordinarily reference the saturation vapor pressure of the solid, however when this is done the isotherm approaches the saturation value at an angle rather than asymptotically. Consequently, the saturation pressure of the supercooled liquid has been more favorably used in argon analysis. Another disadvantage of argon is a relatively ill defined knee on the isotherm (low C value) which makes it difficult to determine the monolayer capacity. Despite it being monatomic the cross sectional area of argon particularly on differing adsorbents has not been firmly established. Thus, in lieu of any decided advantages, nitrogen is generally a more suitable adsorbate.

Due to their low saturation vapor pressures, xenon and krypton both can be used to measure much smaller surface areas than nitrogen, a decided advantage for the characterization of many bulk powders. Xenon suffers from a high polarizability which can result in a relatively strong dispersion interaction with the surface. This can lead to localized adsorption and inconsistent monolayer formation, particularly with impure or inhomogeneous surfaces. For low surface area determinations krypton (though not without similar problems) has become the adsorbate of choice.

Krypton has a saturation vapor pressure of about 2 torr over the solid reference state (Triple point = 116K). Thus the correction for unadsorbed gas is small and determinations of surface areas as low as $10 cm^2/g$ can be accomplished. It shares many of the problems encountered with xenon including inconsistent cross sectional areas. Beebe was forced to adopt a cross sectional area of 19.5 $Å^2$ rather than the calculated molecular area of 15.2 $Å^2$ (Bee45). Modern values lie predominantly in the vicinity of 20 $Å^2$. Krypton also displays a wide range of C values indicating significant variation in the degree of localization in different materials. For glass, the C value ranges from 20-80 (silica gel = 80) while some metals have values in excess of 1000. Before using any alternative gas for adsorption analysis it is prudent to calibrate against known standards or run a comparison with nitrogen. Since krypton used to determine surface areas too low for nitrogen analysis, this is often impractical. When such calibration is impossible, the uncertainty can be as high as 20 percent for krypton measurements (Gre82).

3.3 Nitrogen Analysis of Stober Silica Powder

The first example considered here is a commercial monodisperse silica powder synthesized via the Stober method by Geltech® Inc., Orlando, Florida.. The 0.5 micron diameter powder is expected to be nonporous, spherically shaped and of uniform size (nominally 0.5 microns). The powder is similar to that shown in the photo in Figure 2.17 of the last chapter. The powder was prepared and analyzed using the procedures outlined earlier.

The initial analysis yields a surface area of 7.32 m^2/g. Using equation [3.16] and a density = 2.2g/cc a particle diameter of 372 nanometers is calculated, about 25% smaller than the expected value. There are several possible reasons for the discrepancy. The powder may actually be only 372 nanometers in diameter or it may not be monodisperse (i.e. it contains a fraction of smaller sized spheres). The density of the powder may be less than 2.2g/cc or there may be some microporosity in the powder. There may also be surface roughness that gives rise to additional adsorption. A re-analysis of the sample with emphasis in the low pressure region of the isotherm rules out microporosity and helium pycnometry gives the expected value of 2.2g/cc for the density of the powder. The BET plot and isotherm are depicted in Figure 3.5. Note how similar the isotherm is to the Kelvin plot in Figure 3.3.

Nothing is known about the manufacturer's methodology for size measurement but particle sizing techniques are usually based on light scattering and accuracy is seldom better than ±10%. Stober powders are not always perfectly monodisperse and therefore some variation in sphere size is to be expected. Electron microscopy and a statistical analysis of the results would perhaps better characterize the particle size and solve this mystery but this is time consuming and expensive.

This analysis demonstrates the difficulty in analyzing even a simple, "well behaved" powder. It also illustrates that nitrogen adsorption is ill suited as a stand alone particle sizing technique (except perhaps for rough estimates). Unlike Stober spheres, most powders will have considerable size distributions, irregular shapes, and surface roughness further complicating the analysis.

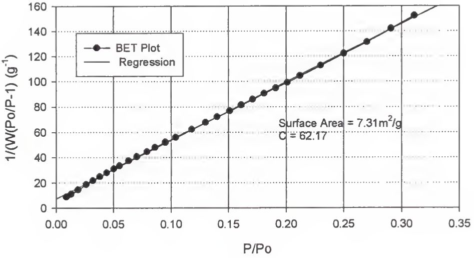
a) BET Plot for 0.50 micron Stober Spheres

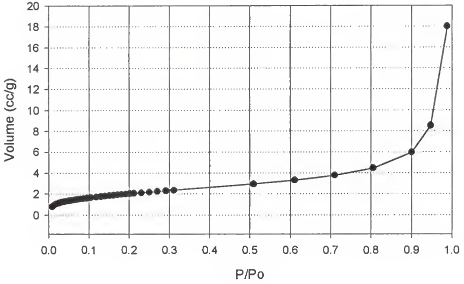
b) Isotherm for Stober Spheres

Figure 3.5. BET data for 500nm diameter Stober spheres. a.) BET plot. b) Isotherm for Stober spheres.

Apart from particle size information nitrogen adsorption does provide the bulk surface area of powders which in itself is valuable information, especially in reactions and processes that are surface mediated, such as catalysis. Very often it is this information rather than the particle size that is most important.

3.4 Microporous Silica Gel

Microporous silica gels can be prepared through the acid catalysis of tetramethoxysilane. Ordinary methods of preparation using R ratios of 8 - 16 generally produce pore sizes in the range of 12 - 15Å. In this preparation solvent extraction is used to decrease the pore radius to around 10Å. Although difficult to dry intact, small monolithic pieces (30 by 7 mm disks) can be produced with pore volumes on the order of 0.2 cc/gram.

The gel analyzed comes from a small monolith produced using a nitric acid catalyzed gel consisting of 20 ml of deionized water, 10ml of 1 normal Nitric acid solution and 60ml of TMOS. The key to this method is to extract as much the methanol as possible from solution before gelation. This is accomplished by hydrolyzing TMOS under acidic conditions at 80°C. The high temperature accelerates the hydrolysis of the TMOS, drives off the product of the hydrolysis (methanol, b.p. 65°C), and accelerates the condensation reaction producing gelation. The removal of the methanol also increases the dielectric strength of the remaining solvent aiding in the charge stabilization of the silica under acidic conditions.

$$Si(OCH_3)_4 + 2H_2O + H^+ \Rightarrow Si(OH)_4 + 4CH_3OH \qquad [3.19]$$

$$2Si(OH)_4 \Rightarrow (OH)_3Si - O - Si(OH)_3 + H_2O \qquad [3.20]$$

All chemicals were reagent grade procured from Fisher Chemical Company except the Tetramethoxysilane which was procured from Aldrich. The water and acid is mixed in a 200 ml Teflon reaction vessel immersed in an 80°C water bath. The TMOS is slowly added and hydrolyzes on contact producing methanol which immediately boils off. When the reaction is completed the mixture is heated for 5 more minutes to ensure the maximum amount of methanol is removed from solution. Stirring is discontinued and the stir bar removed from the solution. The solution is then dispensed into the desired molds with a 60cc plastic syringe and allowed to gel in a quiet location. Gelation occurs in approximately 80 minutes. The gel is allowed to age at room temperature for 2 days followed by aging for 24 hours at 80°C. Drying is carried out in a 50 ml Teflon drying container with a small Teflon septum installed in the tightly sealed top. A small (0.1mm) pinhole is placed in the septum to allow water vapor to escape while maintaining 100% relative humidity in the drying container. The gel is dried for 2 days at 95°C and then slowly ramped up to 180°C over an 18 hour period. After 10 hours at 180°C the gel is cooled to room temperature. The dried gels are slightly yellowish in color and have a bulk density of 1.3g/cc. The gel used in this analysis was stabilized to 840°C using a 10°C ramp rate with a 10 hour hold at 840°C. The product was a clear monolith with some slight crazing on the exterior surface.

The nitrogen adsorption analysis of this microporous silica gel is relatively straightforward. Figure 3.6(a) shows a classic Type A isotherm with a sharp knee occurring at a relative pressure of about 0.30.

Extrapolating the horizontal segment of the isotherm to the volume axis gives the raw volume of 120cc/g which converts to a micropore volume of 0.201 cc/g . The BET surface area in Figure 3.6(b) was calculated over the relative pressure range from .005 to 0.15. The average pore radius calculated by equation [3.11] is 10.16Å. Figure 3.7(a) shows the Langmuir isotherm and Figure 3.7(b) the t-plot. Note that the t-plot indicates a micropore radius in the vicinity of 5Å , the point where the slope changes. Figure 3.8

shows the pore size distributions for the adsorption and desorption isotherms which (as might be expected for a microporous material) are very similar. Care must be taken in interpreting these curves since they are based on the Kelvin equation which has limited value in the micropore region. Both figure 3.6(b) and Figure 3.7 point towards a gaussian shaped pore size distribution with a peak in the vicinity of 5Å in radius. Given that the Kelvin equation in this region generally understates the size of the micropores, it seems more likely that the distribution might be somewhat larger than this (Sing76). This ambiguity demonstrates the difficulty in assigning precise pore sizes in the micropore region. However, it is clear that the sample contains considerable microporosity between 5-10Å in radius with no evidence of mesoporosity.

3.5 Mesoporous Silica Gel

The next sample is a silica gel fabricated to contain both significant microporosity and mesoporosity while maximizing the surface area. This gel was synthesized using a minimum amount of water (R-ratio of 2) and a large excess of methanol. It is theorized that the presence of an excess of methanol produces a more ramified structure and that the lower surface tension of the methanol on drying better preserves the microstructure. This should result in a greater degree of microporosity and a higher surface area than a similar gel synthesized with a higher R-ratio. It was also hoped that the low surface tension of methanol (1/3 that of water) would result in more easily dried monoliths.

The gel is produced by mixing 100ml of methanol, 35 ml of TMOS and 10ml of 3% hydrofluoric acid solution. The methanol and HF is combined in a 200 ml Teflon reaction container at room temperature. The TMOS is then added and the reaction commences. The R- ratio is 2.34, slightly above the stoichiometric minimum. The low R-ratio and high methanol content limits the hydrolysis rate as reflected by a temperature rise

a) Isotherm for Microporous Gel

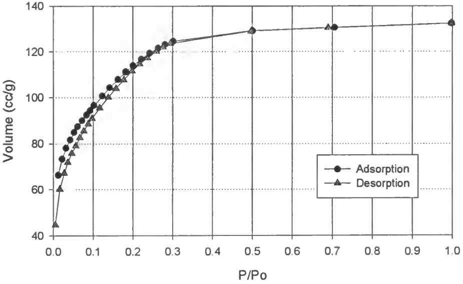

b) BET Plot for Microporous Gel

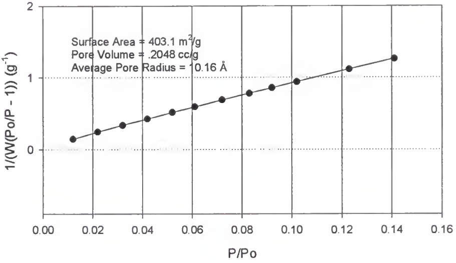

Figure 3.6. Nitrogen adsorption data for microporous gel. a) Isotherms. b) BET plot.

a.) Langmuir Isotherm for Microporous Gel

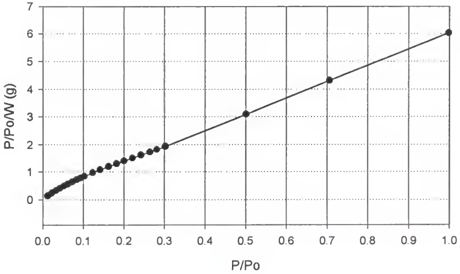

b.) t-plot for Microporous Gel

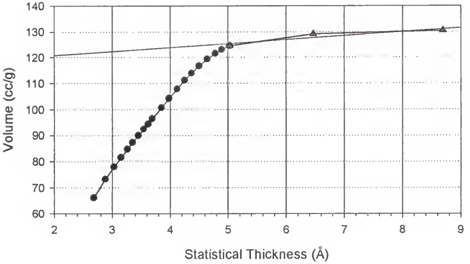

Figure 3.7. Micropore analysis for microporous gel. a.) Langmuir isotherm. b.) t-plot.

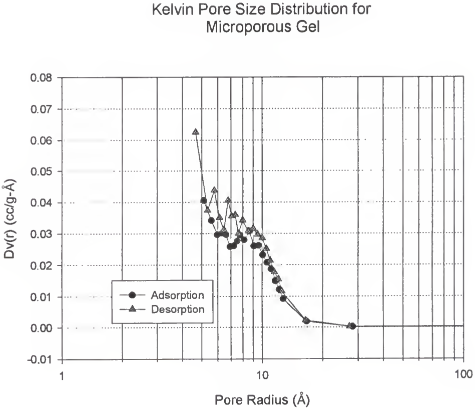

Figure 3.8. Adsorption and desorption pore size distributions for microporous gel.

of only 5°C. The solution gels after 72 minutes and allowed to age at room temperature for 3 days. It is aged at 60°C for 54 hours before drying. Due to the large amount of methanol, the gels can not be aged at higher temperatures without premature drying. The gels are dried at 70°C for 24 hours followed by a slow (10 hour) ramp up to 180°C followed by another 10 hour hold.

Nitrogen adsorption analysis of this sample yields a type II isotherm with the inflection point occurring at low relative pressure as shown in Figure 3.9(a). The BET area is 693 m^2/g which combined with the pore volume gives an average pore radius of 35Å. The surface area is considerably (30%) higher than similar 30 Å gels made with higher R ratios. Figure 3.9(a) shows the adsorption/desorption isotherm and typical hysteresis of mesoporous materials. The hysteresis loop resembles the Type E loop shown in Figure 3.2. This suggests that there exists some ink-bottle type porosity with a fairly broad size distribution in the inkwell. The desorption pore size distribution shown in Figure 3.10(a) has a relatively narrow peak at 37Å and is much sharper than the adsorption distribution. This can be attributed to a smaller pore neck size (37Å) emptying larger interior cavities. Given the relatively broad range of pore/cavity sizes, the proximity of the desorption peak of 37Å with the average pore size of 35Å is probably coincidental.

3.6 Macroporous Silica Gel

This sample is a macroporous silica gel with an average pore radius of 443Å. The gel was synthesized using HF catalysis of an acidic alkoxide solution according to the procedures for the "standard" 200Å formula discussed in Chapter 5. The difference in pore size results from an extended aging schedule specifically designed to increase the pore size. The gel is much larger than the typical samples with a total volume of approximately one liter. The gel was mixed aged and dried in the same 1 liter Teflon™ container. After gelation it was allowed to age at room temperature for 10 days followed

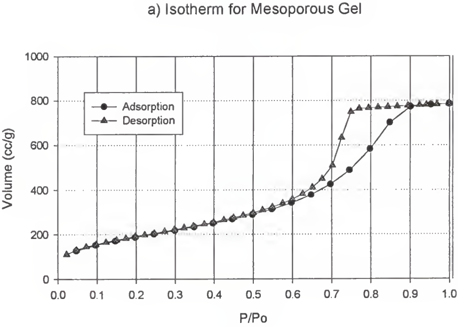

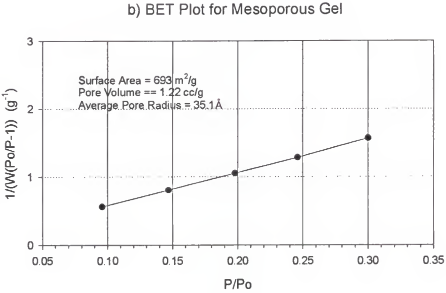

Figure 3.9. BET data for mesoporous gel. a.) Isotherm. b.) BET plot.

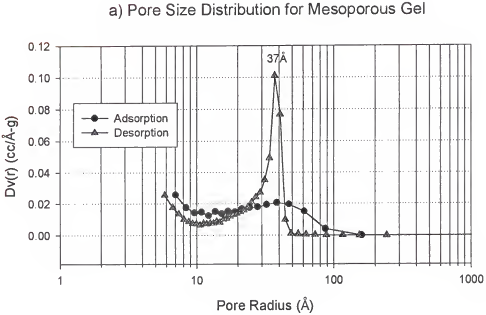

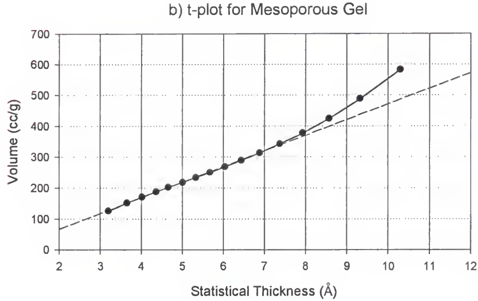

Figure 3.10. Nitrogen adsorption data for mesoporous gel. a) Pore size distribution. b) t-plot. Notice the upward deviation in the t-plot as capillary adsorption begins. Also note that there is some microporosity.

by aging for 24 hours at 80°C. Drying is carried out in the same container with a small Teflon septum installed in the tightly sealed top. A small (0.1mm) pinhole is placed in the septum to allow water vapor to escape while maintaining 100% relative humidity in the drying container. A small amount (50 ml) of deionized water was added to the container to further age and reinforce the gel by Ostwald ripening during the drying process. The gel was dried for 7 days at 95°C and then slowly ramped up to 180°C over an 18 hour period. After 10 hours at 180°C the gel was cooled to room temperature. Although intended to survive as a monolith, the gel fractured on drying into several large pieces which were processed for analysis.

3.6.1 Analysis of Macroporous Silica Gel.

This sample was prepared and analyzed according to standard procedures. A 47-point analysis was made with 24 adsorption and 24 desorption points. The maximum P/Po point was used for both branches of the isotherm. Most of the points were selected in the P/Po range of .900 - .999 since this is the area in which the majority of the capillary condensation occurs for pores greater than 100 Å in radius. Equilibrium time allowed between doses of adsorbate was two minutes. The total analysis time was 21 hours and 32 minutes. The isotherm is depicted in Figure 3.11(a). Note that little adsorption occurs until the relative pressure exceeds .970 at which point the pores begin to fill with condensed adsorbate. By a relative pressure of .992 the pores are filled and the isotherm levels off until the maximum is reached at a relative pressure of .997. The BET analysis shown in Figure 3.11(b) indicates a specific surface area of approximately $80m^2$/gram. The total pore volume is 1.77cc/gram. Using equation [3.13] an average pore radius of 434Å (868Å diameter) is derived.

There are several interesting characteristics of the analysis that are worth noting. The average pore radius is quite large and qualifies the gel as macroporous (greater than

250Å radius according to the generally accepted definition). As such, the bulk of the nitrogen is adsorbed very near the upper limits of the instrument. The accuracey of the pore volume measurement in this range is determined by the precision of the temperature and pressure control in the particular instrument. The hysteresis loop is virtually square shaped and can be clearly recognized as a Type A (according to DeBoer's classification of Figure 3.2) indicating cylindrical shaped pores. The steep vertical rise and fall of the isotherm suggests a narrow pore size distribution. This is more clearly illustrated in Figure 3.12. The difference in the pore sizes calculated from the adsorption verses the desorption isotherm is a common characteristic of nitrogen adsorption in mesoporous materials. Although the reason for the hysteresis loop is still under debate, it has been theorized that the desorption branch is more reliable.

3.6.2 Hysteresis in Nitrogen Adsorption Analysis

Cohan has suggested a mechanism which accounts well for hysteresis observed in Figure 3.12 (Coh38, Gre82). In this model, capillary condensation during adsorption occurs in a pore that is open at both ends and thus experiences a mean radius of curvature that is different from the curvature of a closed capillary. Figure 3.13 illustrates this process. When the pore is filling as in Fig 3.13(a), nitrogen condenses on the surface of the cylinder along its entire radius. The mean curvature r_m introduced in the Kelvin equation is given by

$$\frac{1}{r_m} = \frac{1}{r_1} + \frac{1}{r_2} . \qquad [3.17]$$

When the pore is filling along the sides of the cylinder, r_1 can be represented by the radius of the pore but r_2 is infinite. Thus equation [3.17] reduces to $r_m = r_k$ (where r_k represents the core radius of the pore, that is, the pore radius minus the thickness of the multilayer at this pressure). When the pore is filling or emptying with a hemispherical

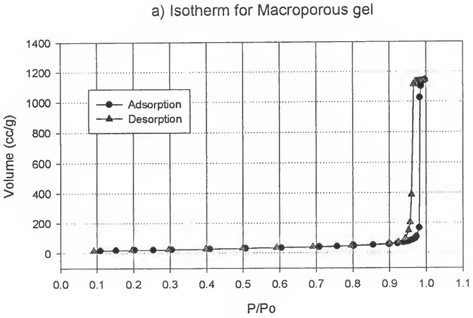

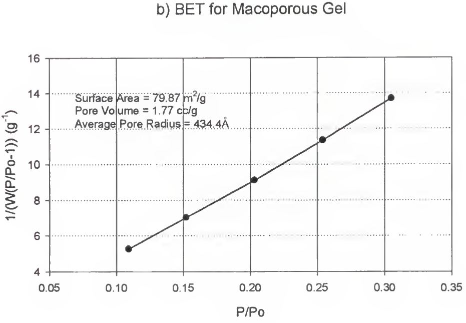

Figure 3.11. BET data for macroporous gel. a.) Isotherm. b.) BET plot.

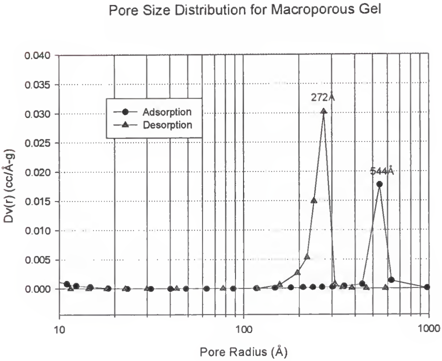

Figure 3.12. Adsorption and desorption pore size distributions for macroporous gel.

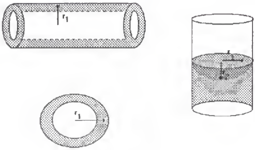

(a) (b)

Figure 3.13. Illustration of capillary condensation in a pore. a.) Cylindrical pore open at both ends filling by condensation on walls. b.) Cylindrical pore filling via a hemispherical meniscus.

meniscus as in Figure 3.13(b), , $r_1 = r_2$,and by equation [3.17], $r_m = 2r_k$. If the Kelvin equation is rewritten in the form of equation [3.18] one can see that the relative pressure required to fill the pore using the cylindrical model will be higher than for a hemispherical meniscus and the calculated pore sizes will differ by a factor of precisely two.

$$\frac{P}{P_o} = \exp(\frac{-2\gamma V_m/RT}{r_m}) \qquad [3.18]$$

Thus for an ideal cylindrical open pore structure, the adsorption isotherm will give a pore size exactly twice that of the desorption isotherm. Figure 3.12 shows that for the macroporous gel this is precisely the case. Although not as dramatic as in this example, the corresponding data is similar for all large mesoporous/ macroporous gels made with this process. Since the desorption process occurs by a capillary mechanism, the open cylinder model strongly supports the use of the desorption isotherm when the Kelvin equation is used for pore size analysis. The square shape of the hysteresis loop is thought to be indicative of cylindrical pores but it should be kept in mind that the pores have a relatively thick multilayer of adsorbate when they begin to fill which makes the inner core more cylindrical in shape than might otherwise be the case. Additionally, in the open cylinder model described above, the radius of curvature decreases as the pores begin to fill, increasing the driving force for condensation. This could account for the sharp vertical rise in the adsorption isotherm as the critical radius is reached.

The conclusion that may be drawn from this analysis is that the larger pore sizes in this sample are best represented by the desorption isotherm. They have a narrow size distribution and according to DeBoer's hysteresis assignments would ordinarily be assigned as type A or cylindrical in shape.

The calculated average pore radius of 434 Å presents a problem however. If the pores are truly cylindrical in shape then the hydraulic pore radius should match fairly closely to the desorption pore radius. Obviously this is not the case. The presence of macropores could account for an unduly large pore volume but it is apparent from the desorption data that there is very little desorption prior to a relative pressure of .966 (corresponding to the 274Å depicted on the desorption pore distribution). Hence, there are few, if any, pores larger than this value.

One way of reconciling these two figures is to assume open ended ink bottle or restricted entry porosity with an entry radius equivalent to the desorption pore size and an interior radius no larger than that of the adsorption pore size. The restricted entry would clearly account for the sharpness of the desorption isotherm but the adsorption isotherm is just as sharp and does not conform to DeBoer's characterization of an ink bottle shape. Under the cylinder model, however, *if the interior radii were no larger than twice that of the entry radii,* one would get just such a sharp rise in the isotherm. As the entrance pores are filled (are sealed off), the mechanism for filling the interior pores would switch from cylinder to meniscus and any interior pores smaller than twice the entrance radius would fill immediately as illustrated in Figure 3.14. This accounts for the rapid filling and emptying of the pores at the two specific points just as the cylinder model predicts but it also accounts for the large average pore radius.

If the open cylinder model of Cohen is the applicable filling mechanism, DeBoer's type E hysteresis loop could only be applied to entry pores small in comparison to interior spaces and interior spaces of a non-uniform size distribution. If the interior spaces are of a uniform size one would always expect a steep vertical rise near the end of the adsorption isotherm as the radius of the interior spaces decreases below a certain critical value and adsorption switches from the cylindrical mechanism to that of a meniscus.

3.7 Vycor® Porous Glass

Vycor is included in this analysis because it has been very well characterized over the years and because its pore structure is closer to the ideal cylindrical shape than silica

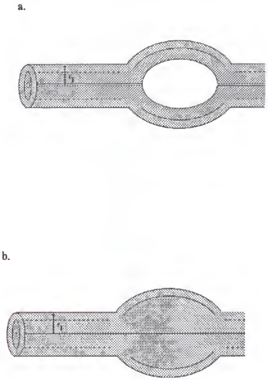

Figure 3.14. As soon as the neck fills up as in (a) the entire ink well will fill up if the well diameter is less than or equal to 1/2 the neck as in (b).

gels. At the same time, the surface structure and degree of hydroxylation is comparable to that of silica gels. (Nord44) Due to its high bulk density, it has greater strength and typically survives rehydration better than silica gels. The sample analyzed is a commercial Vycor 7930 glass produced by Corning, Inc., Corning, New York. Vycor 7930 has a surface area of 105.8 m^2/g and a pore volume of 0.2273 cc/g. The hydraulic pore radius is 43.0 Å. It is interesting to note that the surface area obtained in this analysis is somewhat different from the company literature (200 m^2/g) for 7930 Vycor (Vyc91). Corning suggested that the difference resulted from their use of mercury porosimetry for surface area measurement. This illustrates the wide variation that sometimes occurs between various techniques of analysis. The isotherm in Figure 3.15 is a classic type II with a type A hysteresis loop indicating cylindrical shaped pores. Figure 3.16 shows a very narrow pore size distribution on the desorption curve which is characteristic of Vycor (Elm92). The rest of the analysis is unremarkable save for the pore volume which is a meager 0.2273 cc/g. The low pore volume indicates a high bulk density, (in this case 1.5g/cc), and consequently much greater strength than most silica gels of comparable pore size. The strength of Vycor allows it to be rehydrated more easily than comparable silica gels which have significantly lower bulk densities.

3.8. Aerogel

Much attention has been focused recently on supercritically dried silica gels or aerogels. This drying process eliminates the large capillary pressures encountered during drying by evacuating the solvent above its critical point. Gels can be supercritically dried in either methanol or carbon dioxide. Due to the severe conditions of methanol above its critical point (>190°C and 1600psi) and the danger involved with such a flammable solvent at high temperatures and pressures, CO_2 has come to be the solvent of choice for producing aerogels (Fri92). This particular sample was derived from a 1 step HF catalyzed

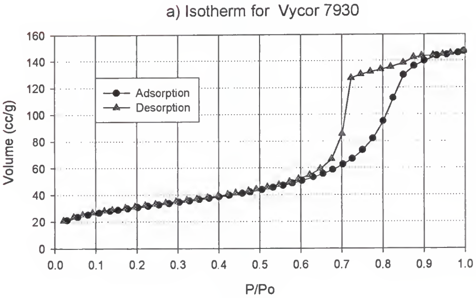

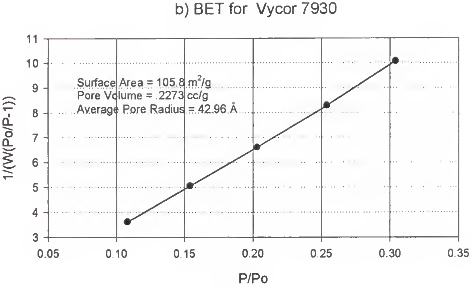

Figure 3.15. BET data for Vycor 7930 porous glass. a.) Isotherm. b.) BET plot.

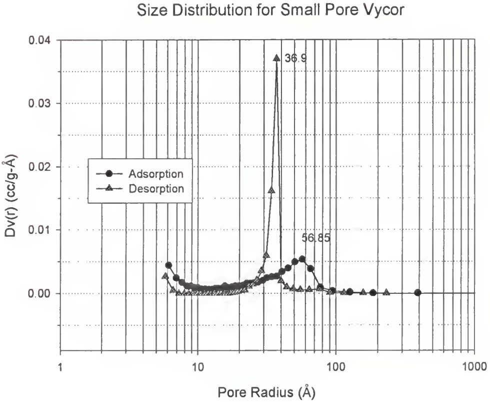

Figure 3.16. Pore size distribution for Vycor 7930 porous glass. Note the extremely narrow desorption pore size distribution.

silica gel supercritically dried with CO_2. The formulation was identical to that of the "standard" formula developed in Chapter 5. The supercritical drying process and preparation of the aerogel is identical to that described in Chapter 6.

The nitrogen adsorption analysis of this aerogel is extremely interesting. As expected of an aerogel it shows a network with a very large pore volume of 5.1 cc/g and a specific surface area of 1020 m^2/g. The average pore radius is 99.9Å. Figure 3.17(a) shows the isotherm and the pore size distributions are depicted in Figure 3.17(b). Note that the desorption pore size distribution is fairly broad and very symmetric. The symmetry is intriguing and may indicate greater uniformity in structure than conventionally dried gels that are subjected to ripening and capillary shrinkage. The upturn in volume at low pressures suggests some microporosity and the t-plot in Figure 3.18 has a very slight downturn at the low end of the plot. This effect is exacerbated by the extremely large surface area of the aerogel.

The negative intercept of the t-plot is problematic. A negative intercept suggests a reduced or incomplete monolayer, just the opposite of the cooperative adsorption in micropores. Ordinarily a negative intercept might be attributable to a low C-constant. However, the C constant in this case is 117.8, well within the normal range for hydrated silica surfaces. What the analysis suggests is that the structure of the gel is made up of a myriad of tiny spherical colloids. Using the measured structural density of 2.01g/cc (measured by He pycnometry) and equation [3.16], and assuming a spherical shape, the particle size for the BET surface area comes out to be 2.94 nm in diameter. With the small radius of curvature of such particles and given the necks between particles, one would expect a lower than normal packing factor for the nitrogen monolayer, hence the negative intercept for the t-plot. As the multilayers form, the curvature and necks begin to even out giving more typical Langmuir adsorption. Long strands or fibrous morphology with interstitial spaces averaging approximately 100 Å would account for the pore size

a) Isotherm for Aerogel

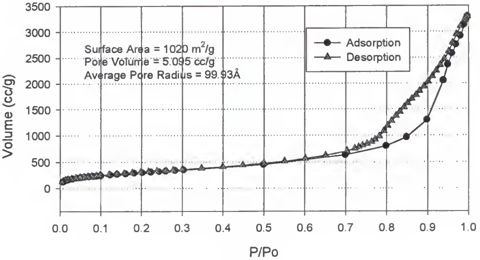

b) Pore Size Distribution for Aerogel

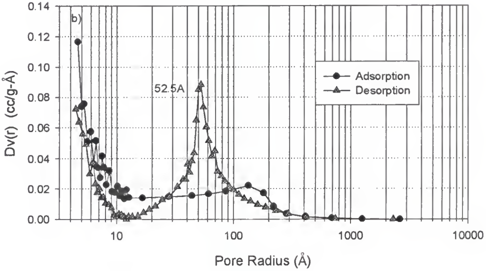

Figure 3.17. Nitrogen adsorption data for an aerogel. a.) Isotherm. b.) Pore size distribution .

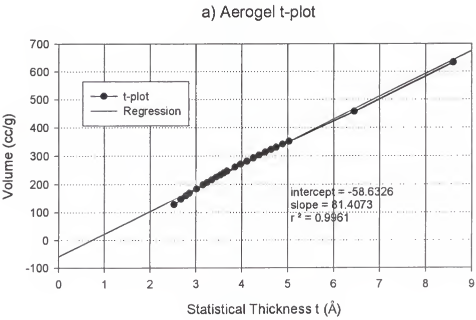
a) Aerogel t-plot

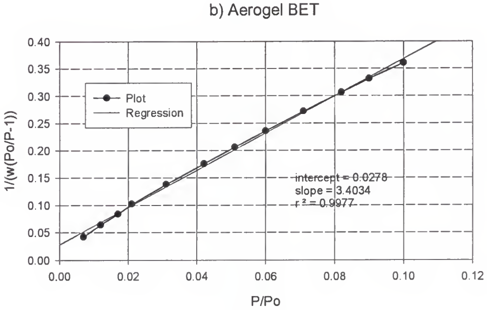
b) Aerogel BET

Figure 3.18. BET data for an aerogel. a.) t-plot. b) BET plot.

distribution depicted in Figure 3.17(b). This is consistent with monomer cluster aggregation (MCA) model described by Brinker (Bri90). The presence of fluoride and acidic conditions enhance the depletion of monomers and the formation of small dense colloidal particles. The well known propensity for silica gels to form primary dense particles of 1-5 nm (in the acid catalyzed reaction) is also consistent with this model (Iler79). This structure is a good demonstration that a large surface area can be the product of pore morphology and not simply the size and number of pores as the average pore radius from equation [3.11] suggests. Interior surfaces of pores can be concave, convex or a combination of the two and the adsorption correspondingly complex.

3.9 Conclusions

The stoichiometry and conditions of gelation are known to have a dramatic effect on the texture and porosity of silica gel monoliths. For most applications it is desirable to have a good understanding of the specific surface area, pore volume, pore shape and pore size distribution. Nitrogen adsorption analysis is an excellent technique for elucidating this information. Accurate and highly reproducible results can be obtained for silica gels and a variety of other porous siliceous materials.

Silicate materials have often been the subject of such studies over the years and their interactions with nitrogen are well characterized. Thus dense powders and mesoporous silicas can be quite reliably analyzed by this method. Microporosity is somewhat more difficult to analyze due to the nature of cooperative forces in the micropores and requires special analytical techniques. Likewise, one must turn to other techniques such as mercury porosimetry for the characterization of large macropores. It is clear however, that understanding the nature of the adsorption process and the information it provides is essential to the correct interpretation of the data. Although the surface area and pore volumes of materials are easily and accurately determined, the exact nature of the porosity can be somewhat more ambiguous and nitrogen adsorption data must be carefully analyzed to give the proper clues for overall pore characterization.

CHAPTER 4

FLUORIDE CATALYSIS OF TMOS DERIVED SILICA GELS

Fluoride has long been known to have a marked catalytic effect on the sol gel reaction under acidic conditions. It has been theorized that fluoride serves to expand the coordination sphere of the silicic acid monomer (or oligimer) making it more subject to nucleophilic attack (Iler79). A pentacoordinate fluorinated species has been proposed as the intermediate. Subsequent research has confirmed that this is almost certainly the case (Rab89, Pop86, Cor86). This chapter presents direct experimental evidence for the existence of a stable anionic hypervalent silicon species involved in the fluoride catalyzed gelation process.

In these experiments an ion-specific fluoride electrode is used to monitor free fluoride concentrations in HF catalyzed sols as silicic acid is added in the form of tetramethoxy silane (TMOS). It is found that fluoride is rapidly bound by the silicic acid in a ratio of approximately four to one, indicative of the formation of multifluorinated silicon complexes. A decrease in the pH provides evidence that anionic hypercoordinate species are formed that are more stable than previously thought. A polymerization scheme is proposed that explains the hydrophobicity of fluoride catalyzed gels and the difficulty in retaining structural fluoride in HF catalyzed sol gel glasses.

4.1 Hypercoordinated Fluoride-Silicon Complexes

Pope and Mackenzie demonstrated that with a TEOS precursor, hydrofluoric acid promoted gelation nearly ten times faster than most mineral acids or bases and 100 times faster than the uncatalyzed reaction (Pop86). The texture of dried HF catalyzed gels typically includes a large pore volume and low surface area, similar to those produced in base catalyzed gels. Thus it is often theorized that the fluoride ion acts similarly to the hydroxide ion in promoting gelation (Bri90). This argument is further supported by the fact that both species are highly electronegative and of similar size. The hydroxide ion has a radius of 1.40 Å and the fluoride ion is slightly smaller at 1.33Å. Most other nucleophilic species (primarily mineral acid counterions) are significantly larger, less electronegative, and have been shown to have little effect on reaction rate (Pop86). Chloride and nitrate for example have radii of 1.81Å and 1.89Å respectively (Huh72). Unfortunately, it is difficult to directly compare the effects of fluoride and hydroxide in aqueous solution since the latter is always present at a concentration which is determined by the pH of the solution. Due to the similarity of the two ions, hydroxide is a major interferent when using the fluoride electrode. Thus fluoride is best studied under acidic conditions.

The effect of hydroxide (pH) has been thoroughly studied and well documented (Bri90). The catalytic effect of both ions is theorized to be due to their ability to expand the coordination sphere of the aqueous silicate species thus making it more susceptible to nucleophilic substitution.

Although well supported by theoretical studies, it is difficult to determine the exact nature of the hypervalent species in the aqueous environment. Most authors characterize it as a fleeting intermediate species in an ongoing polymerization reaction and there are no reported attempts to characterize it directly.

Silicon, with a valence of 4, is known to form primarily tetrahedrally coordinated compounds, however it does form a hexacoordinate species with excess HF in aqueous solution, fluosilicic acid (H_2SiF_6). It is the occurrence of this species (and the similarity of the fluoride and hydroxide ions) that undoubtedly prompted the original speculation that siloxane polymerization was due to a hypervalent intermediate. This view was reinforced by Davis and Burggraf who used molecular orbital calculations (MNDO) to demonstrate that pentacoordinate silicon intermediates are energetically feasible in the gaseous state (Dav88). They concluded that small anions can quite easily increase the coordination sphere of silicon through the involvement of the empty d orbitals. This expansion makes the silicon center more susceptible to nucleophilic substitution.

Later they applied these calculations specifically to base and fluoride catalyzed polymerization reactions between silicic acid species. In this study they used the AM1 model (Austin Method -1) which does a better job of modeling hydrogen bonding in an aqueous environment. They conclude that both hydroxide and fluoride ions are capable of forming a highly stabilized pentacoordinated complex with little or no activation. The subsequent elimination of water (as is necessary for polymerization) is an activated process requiring some 50kcal. Their calculations also support the possible involvement of a hexacoordinate intermediate in base catalyzed condensation (Dav88).

Direct experimental evidence of the hyper-coordinated states is limited. Belot and Corriu et.al. characterized by Si^{29} NMR several hydrido-tetraalkoxysilanes $(HSi(OR)_4)^- K^+$ synthesized by the action of KOR on the trialkoxy silane precursor. They then studied the hydrolysis of the compounds in the presence of water. The evolution of hydrogen gas was evidence of the formation of hydroxy tetraalkoxysilane which corresponds precisely to the type of pentacoordinate species under consideration here. They monitored the subsequent polymerization of the pentacoordinate species and noted many similarities in the gelation of the pentacoordinate hydrido tetraalkoxides with the gelation of acid and base catalyzed silicon tetraalkoxides such as TEOS (Bel90).

4.2 Experimental

In the following series of experiments, the effect of fluoride on gelation is explored using a fluoride electrode to determine the amount of free fluoride in solution. A standard glass pH electrode is used to monitor the hydrogen ion content of solution. The experiments are conducted in acidic conditions. At a pH of 2 with an excess of water (R ratio of 16) hydrolysis of TMOS is very rapid (Kel92). (See Figure 4.1.) This minimizes the influence of hydrolysis on the overall kinetics of the reaction. Consequently, for all but the most concentrated fluoride solutions (where the condensation rate is of the same magnitude as the hydrolysis rate), the gelation time is dependent solely on the condensation reaction.

The pH is measured with a glass pH electrode. Ordinarily, this would be incompatible with an HF solution due to the reaction of HF with the glass membrane. As we shall see however, the concentration of fluoride drops rapidly with the addition of even a small amount of silicic acid (in the form of TMOS) and thus any degradation of the electrode is minimal and of short duration. Low concentrations of fluoride do not affect the use of this electrode (Bon80).

The fluoride electrode is designed to measure the free fluoride ion concentration in solution in a range from 10^{-6} molar (0.02ppm) to saturated. A distinction must be made between the free fluoride concentration and the total fluoride concentration due to the equilibrium of hydrogen fluoride. HF is a weak acid with an acid dissociation constant of $Ka = 6.80\times10^{-4}$ (Bon80).

$$HF_{(aq)} \rightleftharpoons F^-_{(aq)} + H^+_{(aq)} \qquad [4.1]$$

When the fluoride electrode is used to determine *total* fluoride concentrations, the solution must be buffered to pH ≈5.0 in order to free the fluoride bound in the HF and make it available for measurement. This is normally accomplished by using a total ionic strength buffer (TISAB) as was used to calibration the starting concentration of the HF solutions. Under the acidic conditions used in this experiment, however, the total (initial) fluoride concentration is known. Given the free fluoride (F^-) concentration and the hydrogen

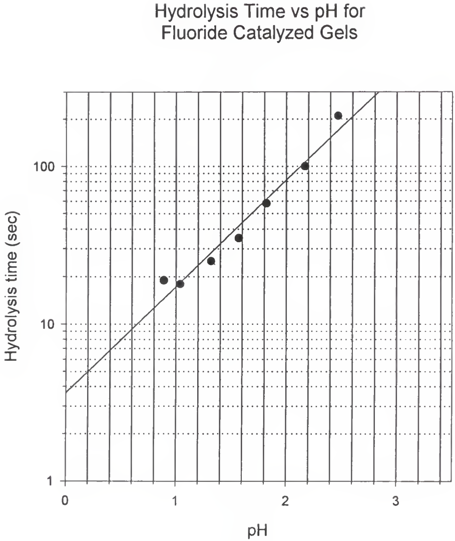

Figure 4.1. Plot of hydrolysis time versus pH for fluoride catalyzed gels. Note that for pH's between 1.0 and 2.0 hydrolysis is very rapid, on the order of a minute or less.

ion (H^+) concentration, the HF concentration can be calculated by using the Ka in equation [4.1]. Fluoride not accounted for by either F^- or HF species must be bound in some manner by the silica in solution. Possibilities include both charged and uncharged species in a variety of hydroxide/fluoride combinations as illustrated in Figure 4.2.

Removal of the fluoride from solution by the formation of a silica complex of any form reduces the amount of free fluoride detected by the electrode. Depending on the number and stability of the silica species, the resulting equilibrium could be rather complex. However, the fluoride concentration will still be directly related to the pH through the HF/F^- equilibrium.

All experiments were conducted in Teflon reaction containers. The hydrofluoric acid solutions were made using Fisher brand 49% HF concentrate diluted in a polypropylene volumetric flask. HF solutions were buffered with TISAB II to a pH of ≈5 for calibration using the fluoride electrode to establish true concentrations. The TMOS was manufactured by ACROS (99%) and procured from Fisher. The fluoride electrode was an ORION model 96-09. It was calibrated before each use with a 0.10 molar standard sodium fluoride solution. A sample calibration curve is depicted in Figure 4.3. The response of the electrode is linear even to very low (10^{-6}M) concentrations of fluoride. The pH electrode was a glass electrode model procured from Fisher. It was calibrated between each measurement using standard buffer solutions of pH 7.00, 4.00, 2.00, and 1.00. A standard 1.00 molar solution of nitric acid from Fisher was used to adjust the initial pH of the solutions.

4.3 HF concentration Versus Gelation Time

The first experiment in this series was conducted to determine the maximum practical concentration of HF that can be used to catalyze a TMOS derived sol and to

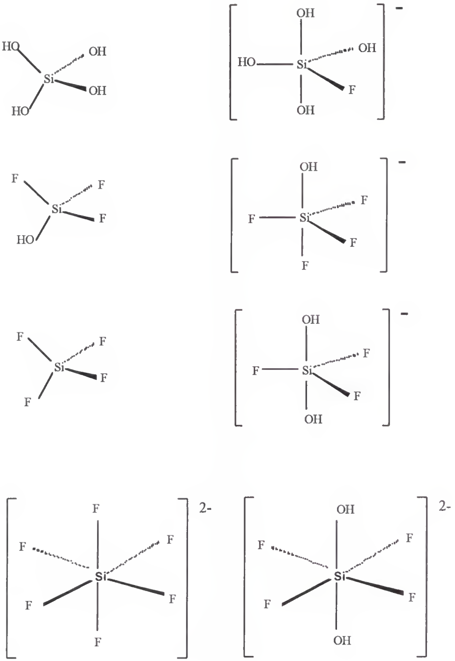

Figure 4.2. Several of the possible combinations of fluoride and hydroxide around the silicon center with tetrahedral, trigonal bypyramidal and octahedral symmetry.

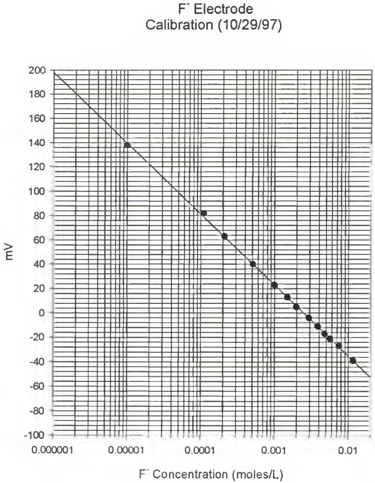

Regression Statistics
Coefficients:
b[0]=-151.812
b[1]=-58.313
r^2=0.9995

Figure 4.3. Calibration curve for the fluoride ion-specific electrode. The electrode response shows good linearity throughout its entire range of sensitivity.

establish the effect of HF concentration on gelation rate under acid conditions. The concentration of the stock HF solution was determined by buffering to a pH of 5 with TISAB and measuring the total fluoride with the fluoride electrode as described previously. Runs were made with concentrations of HF ranging from .00688 molar to 0.4128 M according to Table 4.1. All solutions were cast in polymethylpentane molds. The time of gelation was determined by tipping the mold and observing the reaction of the gel. The error in gel time measurements is estimated to be no more than 5%. Runs were made with HF and TMOS only (pH ≈3.0) and with HF plus TMOS pre-hydrolyzed for 2 minutes in enough nitric acid to bring the initial pH to ≈ 1.5. The initial pH of the HF-only measurements varied from 2.75 (highest concentration) to 3.18 (lowest concentration). For the pre-hydrolyzed solutions the pH varied from 1.40 (high HF concentrations) to 1.75. The variation in pH is a function of the buffering capacity of the aqueous HF system and is discussed in greater detail in Section 4.4.4.

The results of the experiment are recorded in Table 4.1 and displayed graphically in Figure 4.4. As expected, HF concentration has a dramatic effect on the rate of the reaction. Concentrations of HF as little as 0.007 M cause gelation within hours. Concentrations greater than 0.070M cause gelation within minutes. Uncatalyzed TMOS sols (not shown) with the same R ratio take several days to gel. Adjusting the pH of the initial sol to 1.5 with nitric acid causes a more rapid reaction for high concentrations of HF but slower gelation for low HF concentrations. This is because hydrolysis (although very fast for TMOS) becomes rate limiting at high HF concentrations. As the concentration of HF is reduced the reaction becomes condensation limited. Figure 4.5 is a log-log plot of gel time versus HF concentration. It shows the point at which the reaction switches from hydrolysis limited to condensation limited by a change in slope. Although it appears that

Table 4.1. Results of HF concentration versus gel time.

	HF Only		Pre-hydrolyzed	
Molarity of HF	Gel Time (secs)	Gel Rate (sec^{-1})	Gel Time (secs)	Gel Rate (sec^{-1})
.4128	35	.0286	20	.05
.2752	51	.0196	46	.022
.1376	85	.0118	125	.008
.0688	138	.00725	366	2.7e-3
.0344	320	.00313	1320	7.5e-4
.0138	880	.00114	5880	1.7e-4
.00688	1800	.00056	8580	1.2e-4

a. Gel Time versus HF Concentration

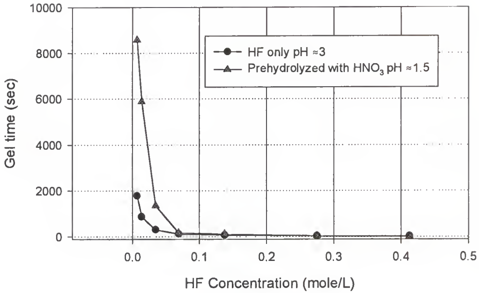

b. Gel Rate versus HF Concentration

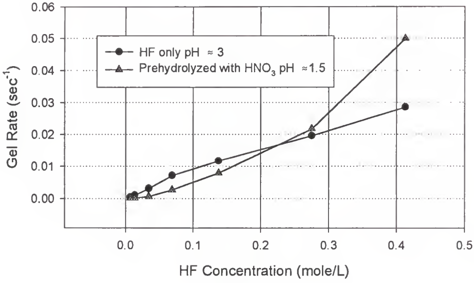

Figure 4.4. The gel time (a) and gel rate (b) of an HF catalyzed TMOS sol as a function of HF concentration. Pre-hydrolyzing the TMOS increases the rate at high HF concentrations where gelation is so fast that it is hydrolysis limited. The lower pH of the pre-hydrolyzed sol slows down the condensation rate at low HF concentrations as in (a).

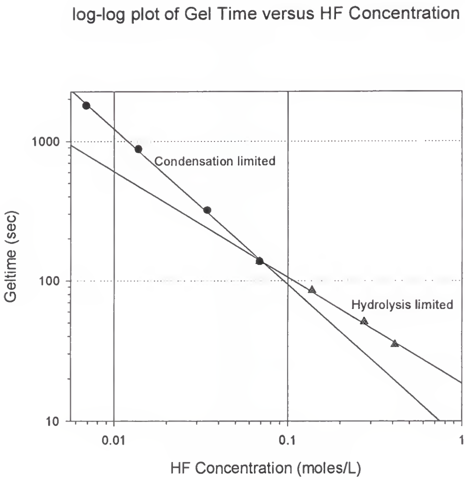

Figure 4.5. Log-log plot of gel time versus HF concentration showing the point at which the reaction changes from hydrolysis limited to condensation limited.

the reaction rate is exponentially related to the concentration of HF, there does not seem to be a simple relationship between the two. Considering the number species involved in the condensation kinetics, this should not be surprising.

4.4 The Fate of Fluoride During Polymerization

This experiment is designed to determine *the fate* of the fluoride introduced as a catalyst in the sol gel reaction. The fluoride electrode is used to monitor the concentration of free fluoride as silicic acid (in the form of TMOS) is added to an HF/HNO_3/water mixture. The concentrations of HF and HNO_3 were selected to correspond with the formula used for the production of large pore monoliths outlined in Chapter 5. The primary question is whether the fluoride introduced as HF remains in the form of *HF* (i.e. the equilibrium of Equation [8.1]), free fluoride (F^-), or a silicon complex of some type. Dimerized (H_2F_2, HF_2^-) species can be neglected due to their very low concentration relative to HF (Bond80). The fluoride ion concentration can be measured directly with the fluoride electrode. The hydrogen ion concentration is determined by measuring the pH. Any fluoride not accounted for by the HF/F^- equilibrium is assumed to be complexed by the silica present in solution.

The second question is, how does the fluoride complex with silica? Does it form a tetrahedral complex through substitution, or one of the hypervalent complexes discussed earlier? The pH of the solution can be used to give some indication of the type of complex formed. For practical reasons, the experiment is repeated in a methanol water mix to determine the effect of methanol in the sol gel system used in Chapter 5.

4.4.1 Experimental.

Three solutions were prepared using 5ml, 10ml, and 20ml of HF (1.376M), 4ml 1N HNO_3, and enough deionized (10MΩ) water to bring the total solution up to 64ml.

This produces solutions with HF concentrations of 0.1075M, 0.2150M and 0.4300M respectively. The solutions were then titrated with TMOS while monitoring the free fluoride concentration and pH.

The temperature of the solution varied by less than 1 °C throughout the titration. TMOS was added in 0.1 ml increments and potentiometric readings were taken of the fluoride concentration and pH after each addition. The fluoride reading stabilized in a few seconds at low concentrations of TMOS but took up to several minutes to stabilize toward the endpoint of the titration. The pH readings tended to drift slightly at higher fluoride concentrations but were very stable after the first few data points (once the fluoride concentrations dropped). The pH electrode was recalibrated several times during the procedure to ensure maximum accuracy. Even so, the first few measurements of pH in each run have a greater uncertainty (±0.05 pH units) than those that follow (± 0.01 pH unit). This does not affect the free fluoride ion (F^-) values derived from the fluoride electrode but may affect the calculated HF concentrations. Fortunately the initial HF concentration (total HF added to the solution) is known with certainty.

4.4.2 Ionic Strength and Activities

The overall ionic strength of the solutions is primarily a function of the added nitric acid since HF is uncharged and makes up the bulk of soluble fluoride at low pH. The ionic strength is defined by the function:

$$I = \frac{1}{2}\sum_i m_i z_i^2 \qquad [4.2]$$

where m is the concentration and z is the charge on the respective ion. For the solutions in question, the initial ionic strength is the same as the molal concentration since all species are 1:1 electrolytes. For all of the solutions the initial ionic strength is .0625 but might rise as high as .1700 depending on the type and charge of the silicon complex formed as

TMOS is added. The activities of the ions can be estimated from the Debye-Huckel expression, which for 1:1 electrolytes is:

$$\log \gamma_{+/-} = -.509\sqrt{I} \qquad [4.3]$$

Using this expression, and the concentrations of HNO_3 and fluoride in the 0.1075M HF solution (the Debye equation is more reliable at lower concentrations), an activity of 0.746 is calculated. This value corresponds reasonably well with the literature value of 0.791 for a 0.1 molal value of nitric acid (CRC70). Assuming HNO_3 is the primary determinant of ionic strength, the uncertainty in ion concentrations associated with activities should be no greater than ±6%.

4.4.3 Results and Discussion

Figure 4.6 is a plot of the moles of free fluoride ion vs the moles of TMOS added as the titration progresses. There are several interesting aspects of the graph. The free fluoride ion concentration decreases almost linearly with the addition of TMOS especially at lower concentrations. The endpoint is the point at which the fluoride ion concentration levels off. The fluoride ion concentration does not level off at zero but rather at a low concentration which appears to be due to an equilibrium with the pH and the silicon species that is/are formed. Figure 4.7 shows the equilibrium portion of the curve in greater detail along with the final pH.

By extrapolating the linear portion of the curves (Figures 4.8 and 4.9) the complexation ratio can be determined for the different concentrations of HF. The initial complexation ratio changes with HF concentration. For the most dilute of the solutions (0.1075M) fluoride complexes with silicic acid in a ratio of approximately 3.5:1. This increases to a 4.2:1 ratio for the 0.2150M solution and a ratio of 5.92 for the most concentrated solutions.

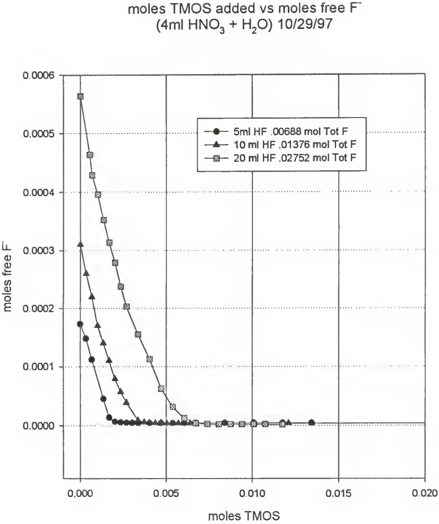

Figure 4.6. Moles of free fluoride versus moles of added TMOS. Results are plotted in terms of moles to emphasize the stoichiometry. The mole ratio at the endpoint is determined by the total moles of HF added (total F in box at top right) divided by the moles of TMOS required to reach the equilibrium level of fluoride.

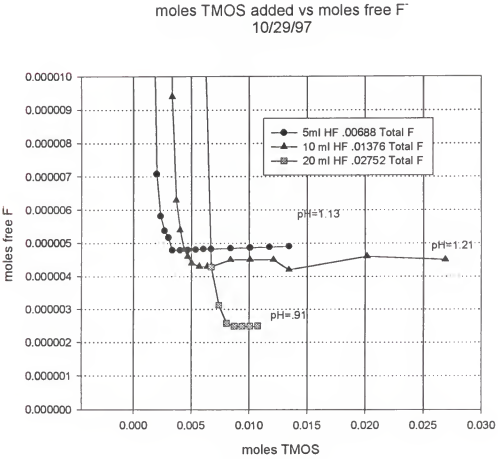

moles TMOS added vs moles free F^-
10/29/97

Figure 4.7. Expanded view of the endpoints of the titrations in Figure 4.6. The higher the initial concentration, the lower the final equilibrium level of fluoride ion.

a.) Free Fluoride vs moles TMOS
for 5ml HF (.00688m) Solution

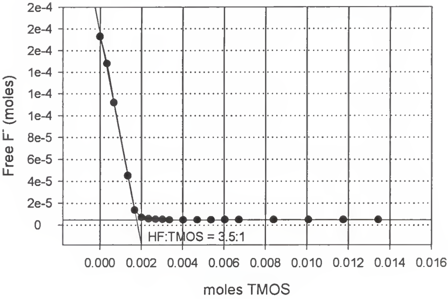

b.) Free Fluoride vs moles TMOS
for 10ml HF (.01376m) Solution

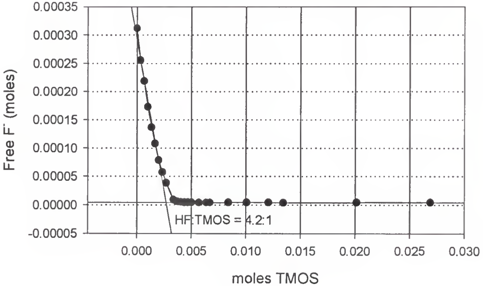

Figure 4.8. If the decrease in fluoride concentration is extrapolated to zero, the complexation ratio of (total) fluoride:TMOS is determined by the x-intercept. a.) Plot of moles free fluoride vs moles TMOS for 5ml HF solution. b.) 10ml HF solution.

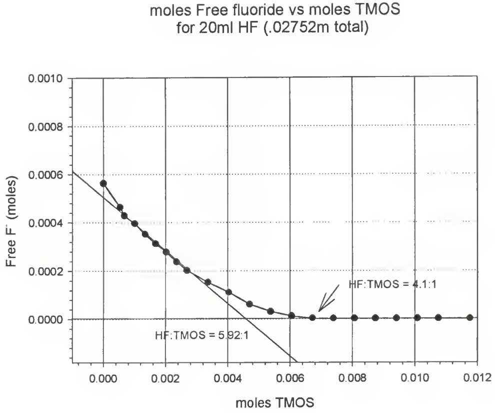

Figure 4.9. Initial complexation ratio for more concentrated solutions is 6:1. As availability of silica increases and the endpoint nears, this drops back to the 4:1 ratio seen in the more dilute solutions. The curvature seen at the beginning of the titration is due to the pH affects on the free fluoride concentration.

These ratios are indicative of the proclivity of silicon to form SiF_4 in the more dilute solutions and H_2SiF_6 in excess HF. Note that the curve tends to flatten out as the endpoint is neared in the most concentrated solution. This indicates that the ability to maintain a 6:1 fluoride ligand ratio is dependent on maintaining *both* an excess of HF *and* a relatively concentrated solution. The more dilute solutions have an initial excess of HF but (as determined by the slope) still do not complex in a 6:1 ratio. The concentrated solution complexes at 6 to 1 but as silicic acid is increased and the endpoint nears, the slope flattens out until the endpoint is reached at a 4:1 complexation ratio. This is congruent with what we know about fluosilicic acid solutions.

4.4.4 Evidence for a Stable Pentavalent Species

The data in Figures 4.6 and 4.7 clearly demonstrate the ability of silicon to form stable hypervalent species with excess fluoride, but this has been long established. What is interesting is the evidence that the hypervalent species incorporates the hydroxide or oxide ligand as TMOS is added. This indicates that there is a competition between the hydroxide and fluoride ligands for the silicon center -- even at low pH! The evidence for a mixed ligand stable hypervalent species is twofold. *The fluoride complexes with silicon reaching a four to one ratio at the endpoint,* and *the pH drops as TMOS is added and the endpoint nears.* The pH drops far lower than can be accounted for by the added nitric and hydrofluoric acid combinations. The only possible source for the additional hydrogen ions is the hypercoordination of the silicic acid complex.

If the fluoride merely substitutes one for one with the hydroxide maintaining tetrahedral coordination, the hydroxide ion released would immediately combine with a free hydrogen ion to form water and the pH would remain stable. The only way for the pH to drop is for the silicic acid to form a *negatively charged* hypervalent species. This removes a counter ion (F^- or OH^-) from solution and results in a lower pH. Figure 4.10 depicts this process. The case for the participation of the hydroxide ligand in this hypervalent complex is a bit more subtle but still compelling. Figures 4.5 and 4.6

indicate that the equilibrium fluoride:silicic acid ratio is in the vicinity of 4:1. Figure 4.7 indicates a 6:1 ratio as long as HF is in excess but as the true endpoint approaches this ratio decreases (slope flattens out) until equilibrium is established in the vicinity of a 4:1 ratio.

When the pH of the solution is plotted versus the TMOS added to the solution (Figure 4.11), it tells an interesting story. The solutions with the higher HF concentrations have a higher initial pH. This is due to the buffering capability of the HF equilibrium. Both the 10ml and 20ml solutions increase in pH initially before dropping. Ordinarily one would expect the pH to decrease due to the formation of the silicon hexafluoride or pentafluoride ions. However, as HF is removed from solution (6 HF for each TMOS) the buffering capacity of the solution actually goes up through the removal of HF from the right side of the equilibrium, hence the rise in pH. This equilibrium is illustrated in Figure 4.12. The reason there is no initial rise in the more dilute (5ml) HF solution is because the buffering capacity of the solution has already been exceeded. Another way of saying this is that silicic acid increases the buffering capacity of HF (pH rises) by removing HF from the right side of the equilibrium. The pH eventually begins to drop but only after the buffering capacity of the F^-/HF system is exceeded. As the silicon begins to form hypervalent species with OH^- in place of the fluoride the pH begins to decrease as previously described.

It is probable that the multiple substitution of fluoride on the silicon center makes it susceptible to nucleophilic attack by water. In this pH range the concentration of OH^- is less than $1x\ 10^{-12}$ moles/liter. It is no wonder polymerization occurs under these conditions. If water is a strong enough nucleophile to hypercoordinate a fluoride substituted silicic acid molecule releasing a H^+, other species such as $SiOH_4$ are likely to be strong enough also. (One might also speculate about the role of other weak nucleophiles such as the NO_3^- which are normally considered spectator ions.) In each

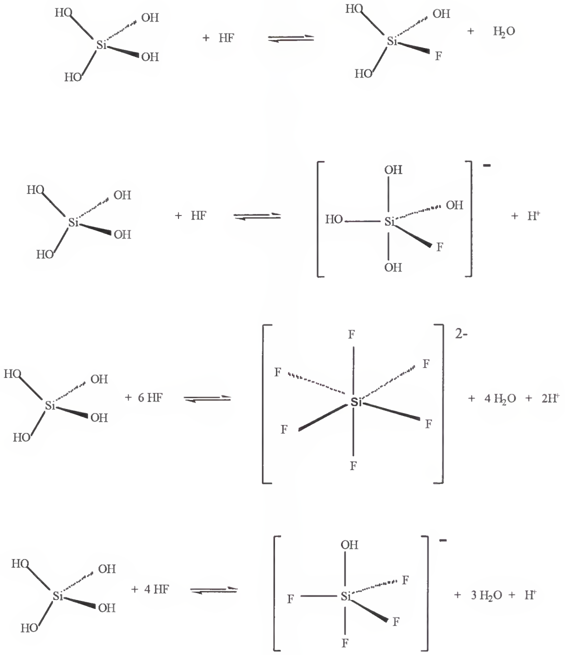

Figure 4.10. Several examples of possible reactions of HF with silicic acid. Substitution reaction (top) produces no change in pH. Reactions that result in charged hypercoordinated species (penta- or hexacoordinated) result in a pH drop.

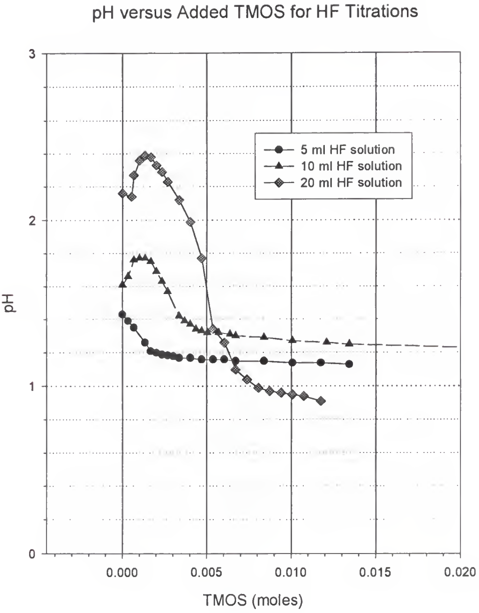

Figure 4.11. The pH of the solution plotted versus the moles of TMOS added. In the more concentrated solutions pH initially rises due to the buffering effect of the high HF concentration. As the buffering capacity is exceeded, pH drops reflecting the formation of negatively charged hypervalent fluorosilicate ions.

a. HIGH CONCENTRATIONS OF HF (6:1) RATIO TO $Si(OH)_4$

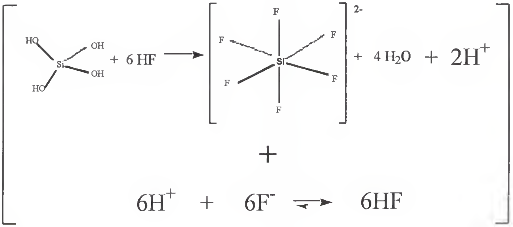

⇓ NET REACTION

$$Si(OH)_4 + 4H^+ + 6F^- \longrightarrow SiF_6^{2-} + 4H_2O \quad pH \uparrow$$

b. LOW CONCENTRATIONS OF HF (4:1) RATIO TO $Si(OH)_4$

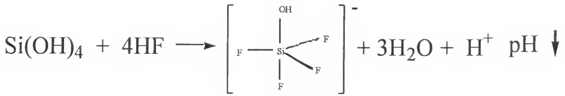

Figure 4.12. At higher HF concentrations pH initially rises before decreasing. a.) Initially the formation of silicon hexafluoride increases the buffering capacity of the solution and the pH rises. b.) Once the buffering capacity of the solution is exceeded the additional silicic acid drives the equilibrium towards the 4:1 fluoride to silicon ratio and the proposed pentacoordinate species depicted. The pH then begins to decrease.

titration, the pH of the solution reaches its minimum coincident with the endpoint of the titration and is relatively stable thereafter.

No matter how much silicic acid is added after the endpoint, the pH and F^- concentration remain the same! This implicates a single (or at least a dominant) species governing the F^- equilibrium in solution. Since the predominant species present at the endpoint is tetrafluorinated, the hydroxytetrafluoride ion (SiF_4OH^-) is a logical candidate. This is by no means the only possibility. Hexacoordinated and/or hydrated species might also play a role in the equilibrium.

Which species actually catalyzes the condensation reaction (i.e. what is the mechanism of polymerization)? If we assume for the moment that SiF_4OH^- is the dominant equilibrium species it should be proportional to F^- through an equilibrium constant (through what might be a rather convoluted equilibrium). The question still remains as to which species, (or combination of species) is responsible for the catalysis of the condensation reaction. The total fluoride ion concentration and its response to the addition of excess TMOS suggests the answer.

4.4.5 Gelation

After the last reading was taken in the titration of the 5ml HF sample, an additional 31 ml of TMOS were rapidly added as is the procedure in a sol gel synthesis. Thus the solution was rapidly saturated with the final 1:16 mole ratio of TMOS:water (R=16). As excess TMOS is added, the solution reacts with a dramatic drop in free fluoride concentration taking about 30 seconds. This is approximately equivalent to the amount of time required for the hydrolysis of the TMOS at this pH. (See Fig 4.1.) After bottoming out, the fluoride concentration begins to recover toward the equilibrium value. This is odd indeed. Why would the free fluoride concentration perturbed by such a dramatic increase in silicic acid spontaneously recover? Shouldn't the silicic acid "soak" up the free fluoride and reach a new equilibrium value? The answer, of course, is that under these conditions the added silicic acid is rapidly polymerized thus removing it from solution and restoring the original equilibrium. Unfortunately the potentiometric determination of the final equilibrium is interrupted by gelation after 3 1/2 minutes! In addition, the hydrolysis of the TMOS is exothermic causing the temperature of the solution to spike up to 50°C. This makes quantitative evaluation of the fluoride and pH unreliable.

The question remains as to the mechanism of the fluoride catalyzed polymerization. The data presented thus far tend to point toward the $SiF_4(OH)^-$ species rather than free fluoride. The final equilibrium values of fluoride concentrations in Figure 4.7 indicate that the free fluoride concentration is lowest for the highest initial HF concentration (highest concentrations of SiF_4OH^-). Thus the solution with the highest equilibrium SiF_4OH^- concentration (lowest F^-) gels the fastest. This implies that *it is not free fluoride that catalyses silica polymerization* but rather the SiF_4OH^- (or some similar multi-fluorinated silica species in the equilibrium).

If the SiF_4OH^- ion is the operative species, a hexacoordinate intermediate is a likely candidate for the condensation reaction. Figure 4.13 depicts a possible mechanism.. Assuming that fluorides are displaced as siloxane bonds form (This is most certainly the case otherwise the polymerization would quickly cease.), they must rapidly combine with the nearest non-(fluoride)-saturated silicic acid molecule available. This is likely to be one in close proximity to the reaction. This results in the fluorides always residing at the surface of the growing colloidal particle. The fact that the equilibrium fluoride concentration and pH remain stable as polymerization proceeds suggests that a single *multivalent* species is responsible. It also implies that the surface of the colloid is highly fluorinated, negatively charged and is itself pentacoordinated. In excess silicic acid therefore *polymerization will take place so as to maximize the concentration of fluoride on the surface*. This is why HF catalyzed gels have a much lower concentration of

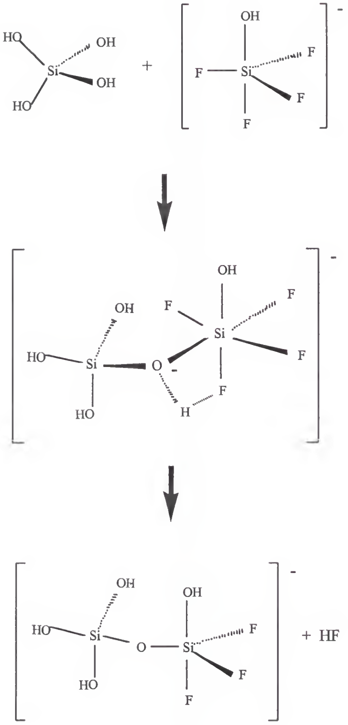

Figure 4.13. Proposed mechanism for HF catalyzed condensation involving a stable pentacoordinate species with a hexacoordinated intermediate.

surface silanols (lower water content), and given enough time, (aging) a much lower surface area. In fact, those catalyzed with large amounts of HF have very hydrophobic surfaces when dry.

4.5 Effect of Solvent on TMOS Titration

Since the byproduct of the hydrolysis reaction is methanol the presence of a mixed solvent system cannot be totally ignored. In addition, the sol gel synthesis of large pore radius HF catalyzed gels (Chapter 5) depends on the addition of methanol to the starting mixture in order to slow down the gel time while retaining a higher HF concentration. In order to gauge the effect of solvent, the TMOS titrations of HF solutions were repeated but with the addition of 50 ml methanol. This is the solvent composition used to produce the "standard" large pore gels in the next chapter. The results are shown in Figure 4.14. The principal effect that can be seen is that the equilibrium fluoride concentration is significantly higher throughout the titration and levels out at a higher equilibrium fluoride concentration. This is counter intuitive (the increased volume should decrease the absolute fluoride concentration) until the effect of pH is considered. The dilution of the sol with methanol results in a higher pH (lower H^+ concentration) which in turn drives the HF equilibrium in equation 4.1 to the left. Apart from the dilution factor, methanol does not appear to affect the shape of the titration curve or the conclusions drawn previously. Methanol definitely slows down the gelation process, however. For example, the 5ml water-only solution gels in 3.5 minutes as opposed to 15 minutes for the methanolic solution. This is partially due to the dilution of the silicic acid component but also argues against the direct involvement of free fluoride as the catalytic agent. *Under acidic conditions it is the concentration of the multi-fluorinated hypervalent silicon that is the principal factor in HF catalysis.*

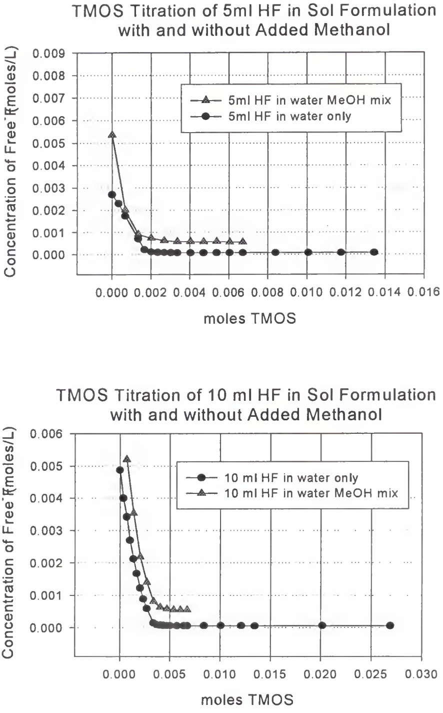

Figure 4.14. The effect of added methanol on the titration of acidified HF solution with TMOS such as occurs in the early stages of HF catalyzed sol gel synthesis.

4.6 Conclusions

Several conclusions can be drawn from these experiments. It must be recognized that the fluoride catalysis of the sol gel reaction involves a complex equilibrium that involves pH, fluoride, HF, and one or more hypervalent fluoride substituted silicic acid species. It appears that the free fluoride ion is not the critical species in the promotion of rapid condensation. Examination of the data indicates that a hypervalent multifluorinated species is most probably the key to the rapid condensation and that the reaction occurs at the surface of the rapidly growing silica colloids. The pentacoordinate SiF_4OH^- species is a good candidate although the evidence is insufficient to confirm this. (For example $H_3SiF_4O_2^-$, a hexacoordinate species would make just as much sense.) If the mechanism proposed in Figure 4.13 is correct, the polymerization takes place on the surface of the growing colloid which is highly fluorinated, negatively charged, and pentacoordinated. Thus polymerization would proceed as to maximize the concentration of fluorides on the surface. (See Figure 4.15.)

This surface polymerization scheme accounts for several observations regarding acidic fluoride catalyzed gels. They tend to be hydrophobic and water poor. It is difficult to retain fluoride in silica glasses that are consolidated from sol gel derived powders or monoliths. During stabilization at high temperatures fluoride is lost as HF and SiF_3 (Nas85).

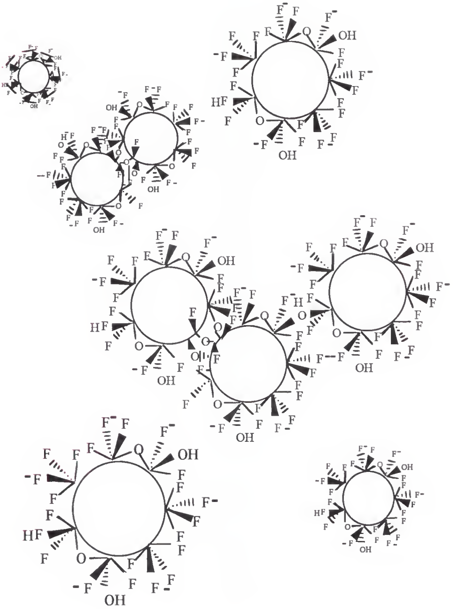

Figure 4.15. Schematic representation of colloidal growth and gelation during HF catalyzed sol gel process synthesis.

CHAPTER 5

SOL GEL PROCESSING OF LARGE PORE MONOLITHS

There are many methods for making large pore silica gels starting from a variety of precursors (Bri90). The term "large pore" is relative but is used here to refer to any gel with a pore radius greater than 10nm. In generally accepted terminology these large pore gels are still considered mesoporous. The gels in this study have pores ranging from 10 to 40 nanometers in radius. What distinguishes these gels from those produced elsewhere is that they can be produced in a single step as monoliths with very narrow pore size distributions. There is no need for base aging or acid etching thus reducing processing time and preserving better homogeneity, pore size distribution and optical properties. Optical transparency in the visible depends on the pore size due to Rayleigh scattering. Air filled monoliths retain a certain degree of optical transparency well into the visible and transmission increases accordingly when they are filled with a solvent or doped with higher refractive index materials.

The size of the pores and large pore volume allows doping with a wide variety of materials to form chemical sensors, solution hosts and nanocomposite materials. Depending on the nature of the dopant, the resulting composite can be used in optical applications in the visible and near IR regions. Unlike smaller pore sizes these large pore gels retain enough strength (relative to capillary forces) to be rehydrated after drying without the failure of the monolith. The ability to rehydrate the gels without high temperature stabilization treatments allows organic and other temperature sensitive dopants to be introduced during gelation and be retained intact in the dried gels. If pre-doping is not required and greater strength is desired the gels can be stabilized at a variety of temperatures up to 1150°C where they generally achieve full density. As stabilization temperature increases pore size remains fairly constant up through 1000°C while pore volume decreases only slightly. Structural hardness increases with increasing stabilization temperature.

5.1 Gel Processing

The flow chart in Figure 5.1 shows the basic steps in producing silica gel monoliths. The first step is to select the silica source. Gels can be made from sodium silicates, colloidal silicas such as Ludox, or a variety of silicon alkoxides. The most common alkoxide precursors are tetraethoxysilane (TEOS) and tetramethoxysilane (TMOS). TMOS was chosen in this system due to its rapid hydrolysis. The use of fluoride as a catalyst (as discussed in Chapter 4) dramatically accelerates the condensation reaction (gelation). Thus it is convenient to have rapid and complete hydrolysis in order to better control the kinetics. All of the gels discussed here are condensation limited. After gelation, the aging and drying steps of the process are the second major determinant of pore size and texture.

It cannot be over emphasized that during drying, as long as there is water in the gel, aging continues. In fact with the higher temperatures involved in drying it may very well be the predominant aging step. This will be explored further in the next chapter. After drying the gels can be used as is or further modified by doping them with the desired material. A big advantage of these large pore monoliths is that they can be doped in the dry state without cracking and redried intact to produce a dried doped gel suitable for immediate use or further stabilization treatments. Stabilization involves heating the dried gels at elevated temperatures to strengthen the gel, change the surface properties or modify the pore volume and pore sizes. As temperatures approach the softening point for silica the pore network collapses due to viscous flow resulting in a fully dense silica (or

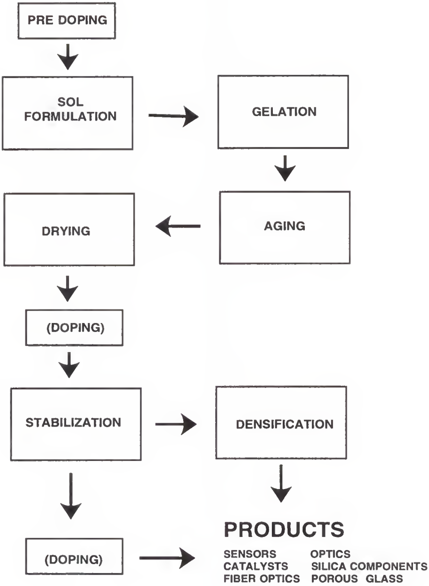

Figure 5.1. Schematic of the basic steps involved in the production of monolithic silica gel products.

doped silica) component. For these large pore gels, dehydroxylation treatments are generally unnecessary.

5.2 Formulation and Mixing

Large pore silica gels can be made by HF catalysis of tetramethoxysilane (TMOS) and water in a nitric acid/methanol solution of pH 2 - 2.5. The molar ratio (R value) of water to TMOS is 16:1. Methanol is added in equal volume proportion to water. The combination of low pH, fluoride catalysis, rapid gelation and the aging/drying processes are responsible for the large pore size. The initial pore texture is controlled primarily by the conditions of gelation, principally the concentration of fluoride, the pH and the R ratio. Table 5.1 presents the formulation for silica gels with a variety of pore sizes. The "standard" formulation used for these studies produced an average pore radius in the vicinity of 200Å, a specific surface area of about 150m^2/g, and a pore volume of about 1.6 cc/g when aged and dried according to the schedule in Figure 5.2. Extended periods of aging or drying, or changes in the pore liquor during aging can significantly affect the pore texture as will be discussed later. Figure 5.3 shows a photograph of a variety of 200Å monoliths. Figures 5.4 and 5.5 show the nitrogen adsorption data for a representative sample of a dried gel.

For HF gels and the larger pore sizes, gelation at room temperature can be very rapid, often on the order of a few minutes. Too rapid a gelation of the sol is undesirable for several reasons including insufficient processing time, poor homogeneity, bubble formation and rapid temperature rise. In extreme cases the latter can actually result in boil off of methanol (B.P. 65°C). Hydrolysis of TMOS is very rapid under acidic conditions. Due to its rapidity, the exothermic reaction can be considered complete when the temperature of the solution peaks and levels off. For the standard large pore system this occurs within 2 minutes. In order to increase the time available for filtering and casting

Table 5.1. Formulations for HF catalyzed TMOS derived monoliths.
* Indicates reactants cooled in an ice bath (≈5°C) prior to mixing.

Pore Radius Å (Nominal)	H_2O (ml)	CH_3OH (ml)	TMOS (ml)	HF (3%) (ml)	HNO_3 (1N) (ml)
30	50	0	35	1.5	10
45	50	0	35	2.5	10
100*	25	50	35	4	4
150*	25	50	35	12.5	4
200*	50	50	35	10	4
250*	50	50	35	12.5	4
400*	50	50	35	(2.25 ml of 25% H_2SiF_6)	0

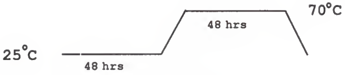

STANDARD AGING SCHEDULE

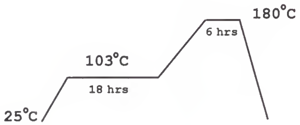

STANDARD DRYING SCHEDULE

Figure 5.2. Standard aging and drying schedules for small monoliths (2.5cm x .7cm) in the large pore system. Larger monoliths require longer drying times but aging schedule is the same.

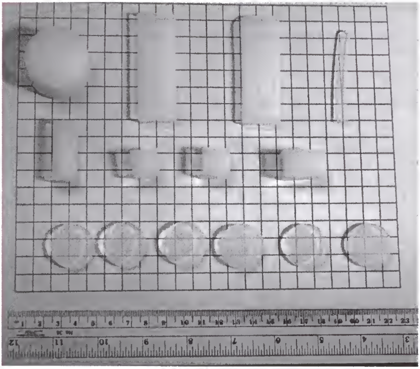

Figure 5.3. A variety of silica gel monoliths made with the “standard” formula for 200 angstrom radius.

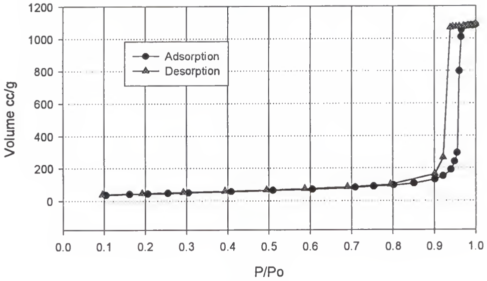

a.) Isotherm for KP70115

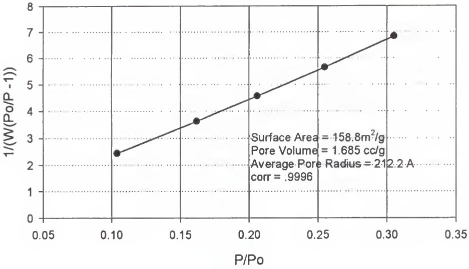

b.) BET for KP70115

Surface Area = 158.8m^2/g
Pore Volume = 1.685 cc/g
Average Pore Radius = 212.2 A
corr = .9996

Figure 5.4. The isotherm (a) and BET plot (b) for a representative silica gel monolith. Gel is made with the standard formula using the aging and drying schedules of Figure 5.2.

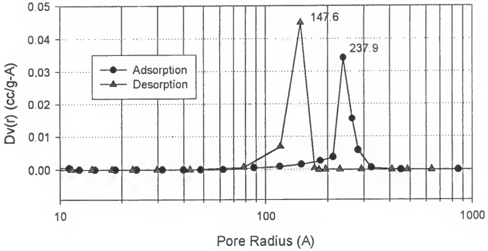

a.) KP70115 Pore Size Distribution

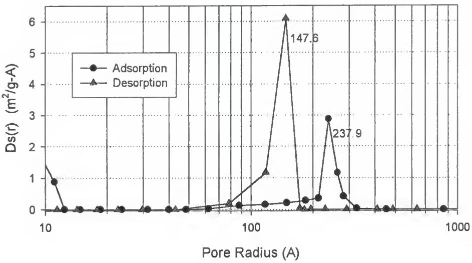

b.) KP70115 Surface Area Distribution

Figure 5.5. Pore size distributions (a) and surface area distributions (b) for the same standard formula gel monolith shown in Figure 5.4. Notice the hysteresis effect between the adsorption and desorption curves. Desorption distributions are usually considered to more closely represent the equilibrium pore size.

the gels, the reactants are generally cooled in an ice bath to 5°C. The heat generated by hydrolysis is just enough to raise the temperature to approximately room temperature (25°C) allowing processing and gelation to occur at a stable temperature.

5.3 Cosolvent

The addition of methanol as a cosolvent has several effects on the sol. It enhances the miscibility of the TMOS and water, raises the pH of the solution slightly, moderates the temperature rise by increasing the total thermal mass of the solution, and slows down the condensation reaction allowing more time for processing the sol. It also increases the total volume of gelation which surprisingly doesn't have much affect on the final gel texture. This result will be discussed further in the next chapter.

5.4 Casting

The sol is allowed to stir for several minutes before being cast into polymethylpentane molds. A variety of methods can be used to effect the transfer but the most convenient found is to use a 60ml polypropylene Luer lock syringe with a 1.0 micron Teflon syringe filter. The sol is filtered to remove any dust or other particles which might serve as crack initiation sites within the gel. It is by no means proven that such particulates increase the failure rate of the monoliths and many gels have been made with good results without filtering. However prudence dictates that when possible filtering should be employed. Likewise, the presence of bubbles within the gel should be avoided whenever possible although the photo in Figure 5.6 demonstrates that bubbles are not always fatal to the gel monolith. With the short time available between mixing and gelation, filtering and casting should be done expeditiously. As the solution approaches the gelation point, the Teflon filter begins to clog and transfer becomes difficult. It is important that enough time is allowed to tightly cap the molds before gelation. If the

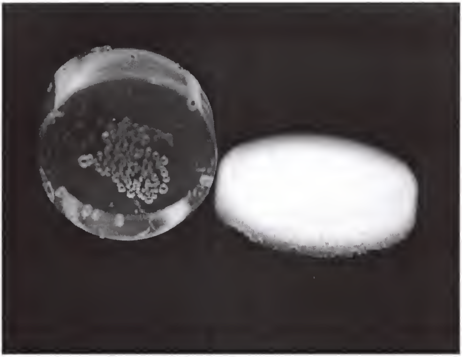

Figure 5.6. Bubbles although undesirable, can survive the drying process as evidenced by this photograph of two dried gel monoliths. The gel on the left has an estimated pore radius of about 20 Å while the one on the right is a standard 200Å gel.

solution gels in the open air evaporation from the surface causes a "lizard skin"- like surface on the gel. Crazing or cracking follow soon after.

5.5 Mold Selection

A wide variety of plastics can be used as molds for nitric acid/HF gels. Polystyrene, polypropylene, polycarbonate, polymethylpentane (PMP), and Teflon® have all been successfully used in this study, however, polymethylpentane (PMP) is preferred. This polymer has a sufficiently smooth surface, is not attacked by TMOS, is strong enough to resist deformation when sealed during the aging process and is very hydrophobic. The latter characteristic is important in minimizing the formation of a meniscus which introduces curvature on the top surface of the gel. In sensitive gels, the meniscus often causes the top edge of the gel to break off around its circumference. Sharp, angular shapes are more difficult to dry intact for reasons which will be discussed later.

Although PMP is stable up to 130°C it generally can not be used for drying due to a tendency to react with the decomposing nitric acid at the end of the drying cycle. Ideally it would be nice to dry the gels in the original mold to avoid the necessity of transferring the fragile gels to a separate drying container. This can be done in PMP if the drying temperature is lowered and the drying time extended however this results in a lower yield of intact gels. High concentrations of nitric acid at elevated temperatures cause the PMP polymer to deteriorate and release organic byproducts into the gels. Consequently, gels are normally transferred to Teflon containers for drying and are brought to a final drying temperature of 180°C. Teflon containers are sometimes used for molds but the Teflon surface is soft and does not produce a very smooth surface. Teflon is also expensive and available only in limited shapes and sizes.

5.6 Aging

After casting, the gels are placed on a stable surface in an undisturbed location to age at room temperature for a minimum of 2 days. Significant syneresis ($\approx 10\%$) occurs within an hour and continues at a lower rate throughout the aging period. The molds are then placed in an oven and aged at 70° for another 24 hours. It is important that the molds be tightly capped during this period since methanol boils at 65°C. Loss of too much solvent during the aging process results in premature drying and failure of the monoliths. This aging step ensures that all unreacted silicic acid monomer is depleted. During aging and drying the gel structure undergoes Ostwald ripening especially at elevated temperatures. The pore liquor has a pH of 2 which also increases solubility of silica. Aging is a major determinant of the final gel structure (along with the formulation and drying method).

5.7 Drying

The drying process used for large pore monoliths is essentially the same as that for other gels. The larger pores, lower capillary stresses and greater permeability allow the process to be shortened to as little as 24 hours for small monoliths (25mm x 7mm). After aging, the wet gels are carefully removed from the molds and washed with deionized water. They are placed in Teflon drying containers filled with water. The function of the water is to cushion the fragile gel as it sinks to the bottom of the drying container. The water is then carefully poured out leaving only the wet gel in the bottom. The container is sealed and a small pinhole placed in a Teflon® septum. The purpose of the pinhole is to maintain a condition of near 100% humidity around the gel while it is drying. Larger monoliths are more difficult to handle and consequently are most often cast and dried in the same Teflon container.

5.7.1 Drying Schedule

The drying schedule varies depending on the size of the monolith. Once the gel has survived the opaque stage, it is insensitive to the rate of further drying. After this stage is over, the gels are brought a final temperature of 180°C as this is the temperature at which most physically adsorbed water is removed. Further heating begins the stabilization process wherein proximate silanol groups condense to form water which then diffuses out of the gel.

Larger monoliths of the same basic formulation generally have lower surface areas, larger pore volumes and larger average pore sizes. Figure 5.7 is a comparison of the nitrogen adsorption analysis of three different size monoliths made with the same basic formulation. The difference in pore structure is only indirectly related to the size of the monolith. The primary determinant is the length of time the gel is subjected to the high temperature aqueous environment. Larger gels take longer to dry, hence age for a longer period, resulting in larger pores and lower surface areas. Larger pores exert less capillary pressure, hence shrinkage during drying is less resulting in a larger pore volume which also contributes to a larger average pore radius. Figure 5.8 shows a disk dried in 24 hours contrasted with a large 75mm by 75mm cylinder which took 2 weeks to dry. Drying time is influenced by the size of the monolith as the water must flow/diffuse over a longer path-length in larger pieces and there is less external surface area in proportion to gel volume.

5.7.2 Drying Intact Monoliths

The maximum stress on the gel occurs at the critical point i.e. the point at which the liquid begins to penetrate the pores. This is also the point at which the gels begin to turn opaque. One might initially speculate that a larger monolith should better survive the drying process since the tension applied by the liquid is applied over a longer path i.e. the center of the gel to the drying front. With the advent of large pore monoliths however, it

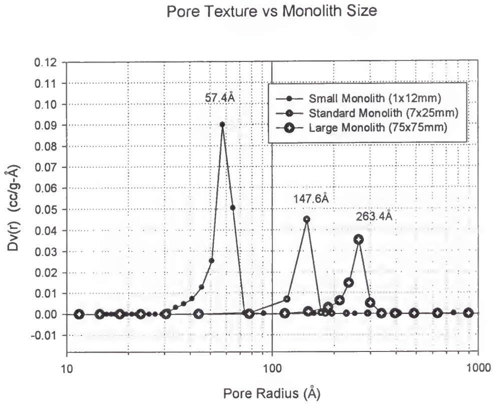

Figure 5.7. Desorption pore size distributions for three gels made with the same formulation but with different pore textures due to differences in drying schedules. The small monolith was dried in 24 hours at 60°C. The standard monolith was dried at 103°C for 24 hours and the large monolith was dried at 95°C for 2 weeks. All were treated with a 6 hour hold at a final temperature of 180°C.

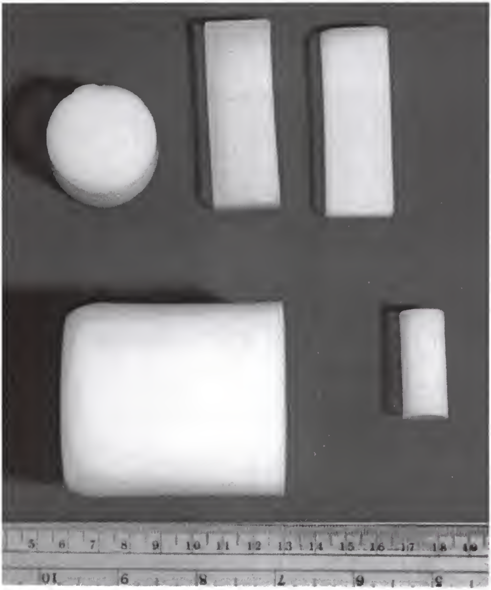

Figure 5.8. Several different size silica monoliths made with the same formulation but dried with different schedules. The small rectangular monoliths on the upper right were dried using the normal schedule while the 2 larger cylinders on the left were subject to much longer drying times. The largest cylinder took over 2 weeks to dry.

has become apparent that the actual stress front extends over a relatively short distance centered in the vicinity of the drying front (identified by the movement of the opaque stage). Large pore gels can be rehydrated without failure and the drying front and opaque stage observed under ambient conditions. Generally, the monolith will dry from the outside towards the center but this is not always the case as can be seen by Figure 5.9 where the opaque stage has started in the interior of the gel. Contrary to popular opinion it has also been observed that drying a gel *too slowly* can cause failure just as drying it too quickly. The rehydration characteristics of the large pore gels give an indication as to why this may occur.

5.8 Rehydration and Doping Gel Monoliths

The best way to rehydrate a gel is by immersing only the bottom of the gel in liquid. This allows the air in the pore network to escape through the top of the gel as demonstrated in Figure 5.10. Rehydration is usually rapid and without incident. If the gel is completely immersed in water, it will rehydrate more slowly since the air must diffuse out through the already filled pores. Experience has proven that the threshold pore size for the successful rehydration of dried gels is in the vicinity of 70 -80Å. Gels with smaller pores can be stabilized at high temperatures to impart greater stability towards water. Thus smaller pore stabilized gels can often be rehydrated without failure.

If, however, rehydration is interrupted for too long a period the gel will crack in the vicinity of the demarcation between the rehydrated and dry areas of the gel. The fracture occurs after a delay (up to several minutes depending on the speed of rehydration) attributable to the equilibration of the hydrated portion of the gel. This characteristic suggests that a maximum degree of stress is produced between the fully hydrated and empty or funicular areas within the gel. It also suggests a time related dependence. If the rehydration front is kept moving cracking is avoided. If it moves too slowly or stops, the

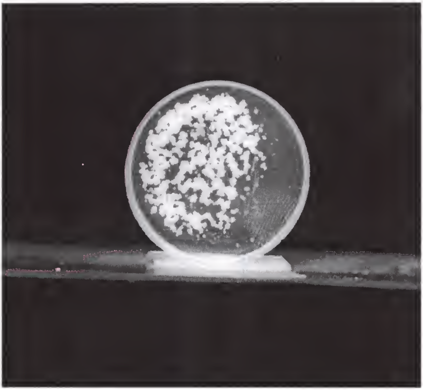

Figure 5.9. Large pore gel just beginning to enter the opaque stage during drying. Notice the cauliflower shaped opaque areas beginning to form in the interior of the gel.

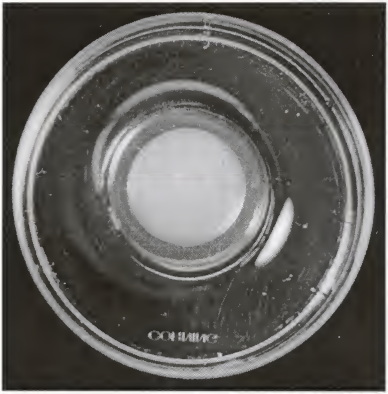

Figure 5.10. Large pore gel being rehydrated with water in a plastic dish. Notice the reduction in optical scattering as the liquid penetrates the gel.

gel cracks. Figure 5.11 is a series of photos illustrating what happens when the rehydration of a large pore gel is interrupted. Notice that although cracks extend out into the dry portion of the gel, the fracture surface itself occurs almost precisely along the rehydration boundary. Although there are significant differences between the drying scenario and the rehydration of gels, experience has shown that gels dried too slowly are prone to failure just as gels dried too quickly. In fact, a rehydrated gel can be placed in a drying container and rapidly redried at 103°C without failure while the same gel if left to dry slowly at ambient temperature almost invariably will fail.

Once a gel has been rehydrated and removed from the solution it begins to dry. Opaque areas soon begin to appear and grow as water evaporates from the surface of the gel. The last two frames in Figure 5.11 show the opaque area begin to spread as the rehydrated portion of the gel begins to dry. Opaque areas have even been observed to begin in the center of a gel. Once the gel is entirely opaque it becomes insensitive to drying rate. As drying continues the gel (depending on pore size and scattering) once again becomes transparent or translucent.

5.9 Stabilization and Densification

The stabilization of large pore gels is very similar to their smaller pore cousins except that pore shrinkage and closure occurs at a higher temperature. There is little change in pore texture up to about 1000°C at which point densification begins. Due to their lower specific surface areas (typically 150 m^2/g vs 500 m^2/g for a 45Å gel) large pore gel monoliths are less hydrophilic and retain less water than higher surface area gels. A typical 200Å pore radius gel will pick up approximately 2% by weight in water vapor from the atmosphere as opposed to more than 6% for a 45Å gel. The greater permeability of large pore gels also allows water vapor to more readily escape during stabilization and consolidation. In addition, large pore matrices consolidate at higher temperatures than

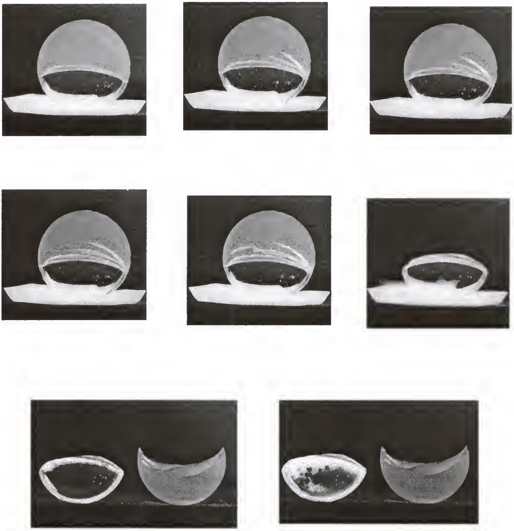

Figure 5.11. Series of photos illustrating what happens when rehydration of a large pore monolith is interrupted. Photos were taken approximately one minute apart after rehydration was interrupted by the removal of the water source. Although several cracks propagate into the dry portion of the gel, the fracture plane is precisely along the rehydration front. Note also the beginning of the opaque stage in the last two frames.

smaller pore gels. Consequently, the large pore monoliths can be brought to full density under ambient atmosphere without dehydroxylation treatments. Figure 5.12 shows the densification schedule for the system. Full density is normally achieved by heating the gels to 1150°C - 1200°C. Bloating can still be a problem with larger size pieces if the heating rate is too rapid but for the typical 2 x 0.7cm disks it is infrequent. The effects of stabilization and densification treatments on pore texture discussed in more detail in Chapter 7.

Dried monoliths are also machinable. They are relatively soft and can be cut dry with ordinary tools (such as a small band saw, or lathe) or shaped with a grinding wheel. They can then be densified as described above. Thus larger more intricately shaped pieces can be cut from a standard shaped cylinder (or even from larger fragments of a failed monolith).

5.10 Conclusions

The large pore gel system described here shows promise in several areas such as optical sensor substrates, catalyst supports and as preforms for dense high purity silica components. In the smaller size range (up to about 2.5cm by 1cm) they are easily manufactured with excellent yields (approx. 90%). Larger sizes are still difficult to produce. At a pore radius of 200Å, they retain enough transparency to be useful in optical sensing applications, can be easily rehydrated and redried without failure, and can be reliably brought to full density. The relatively large pore size imparts good permeability and the large pore volume permits doping with a wide variety of materials. As shall be seen in the next chapter, the pore volume and surface area can also be modified in either direction.

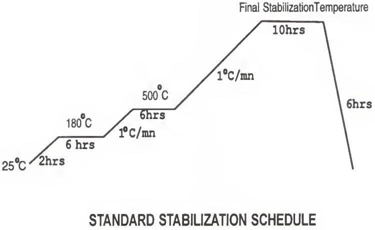
Final StabilizationTemperature
10hrs
1°C/mn
500°C
6hrs
180°C
1°C/mn
6 hrs
25°C
2hrs
6hrs
STANDARD STABILIZATION SCHEDULE

Figure 5.12. Standard densification schedule for large pore monoliths.

CHAPTER 6

VARIATION OF PORE SIZE BY AGING AND DRYING

The following experiments examine the modification of pore morphology through aging and drying treatments. Traditionally, aging has been used to strengthen the gel before drying and extended aging treatments have been used to increase the final pore size of the gel. Aging in high pH solutions (base aging) has been employed to increase the solubility of silica and accelerate the Ostwald ripening process. Gel monoliths in the 100Å pore radius range have been routinely produced through this method (Liu91). It has been difficult to follow the evolution of the pore structure through the aging process since there is no easy way to freeze the pore morphology and remove the solvent without further modification of the pores.

Conventional drying of gels dramatically alters the pore structure since it is essentially a form of high temperature aging up to the point at which the pores become pendular. The pore structure is also modified during the drying process through capillary pressures which create a compressive stress on the gel causing it to shrink. As the gel shrinks it continues to age in what is usually a high temperature acidic aqueous environment. The final pore structure is not determined until the pores begin to empty of solvent to reveal a dry gel.

In the first experiment, supercritical drying is used to elucidate the change in pore structure at several steps throughout the aging process. The assumption is made that by exchanging the pore solvent with methanol, the aging process is arrested due to the low solubility of silica in methanol. Supercritical drying is then used to remove the solvent leaving the pore structure relatively unchanged. The dried gel can then be analyzed by nitrogen adsorption to ascertain the surface area, pore size and distribution. By analyzing the gel at several points, a picture of the aging process can be constructed.

The second experiment examines the concept of aging silica gels in an acid environment in combination with a silica "donor" consisting of a high surface area silica gel. This explores the possibility of adding additional silica to the gel during aging to increase the strength and bulk density while *decreasing* the pore size. Though the pore size change is in the opposite direction, the objective is the same -- to increase the strength and survival of gel monoliths.

The third experiment deals with the effect of gelation volume on the ultimate pore size of the gel. A fixed amount of sol is diluted to increase the volume of the gel while keeping the same solids content. At first one is inclined to think that increasing the gelation volume should increase the pore volume and hence the average pore radius. This turns out not to be the case.

6.1 The Evolution of Pore Structure During Aging and Drying

In this experiment the change in the pore structure of a standard large pore gel is determined at several steps in the aging and drying process through the use of supercritical CO_2 drying. The gel formulation was that of the "standard 200Å" formulation as recorded in Table 5.1 in the last chapter. Four samples were analyzed at four different stages of aging/drying.

6.1.1 Experimental

The starting solution was cooled to 15°C. Upon addition of the TMOS, the temperature rose to 31.5°C. After 8 minutes 10ml of sol was filtered into several 15ml PMP molds. The remainder of the sol was left to gel in the Teflon reaction container and aged and dried separately. After two hours and forty five minutes one gel was immersed in 250 milliliters of Fisher Optima grade 99.9% methanol with magnetic stirring in order to replace the pore liquor with methanol. The remaining gels were aged for 2 days at room temperature followed by 24 hours at 70°C.

The first gel was left in methanol for two days to allow adequate time for the solvent in the pores to equilibrate. The methanol was changed daily in order to reduce the amount of residual water in the pore liquor. The percentage of water in the equilibrated solvent was calculated to be no more than 1.5% by weight. The gel was then removed and supercritically dried in a SAMDRI 780 critical point CO_2 dryer designed primarily for drying biological samples for electron microscopy.

After solvent exchange, the 20mm x 22mm cylindrical gel was placed in a specially constructed sample holder in the sample chamber of the critical point dryer. The sample chamber was cooled to 10°C and filled with liquid carbon dioxide. The sample chamber was kept between 0°C and 10°C and the CO_2 was purged and replaced every 10 minutes for 6 hours. The chamber was then heated to above 31° C and allowed to equilibrate. The pressure of the chamber was 1150 psi at this point. After 10 minutes the chamber was slowly purged of CO_2 over a period of 30 minutes. The resultant gel was then removed for analysis by nitrogen adsorption. Mercury and helium pycnometry was used to determine the bulk and structural densities of the aerogel.

The second sample was aged normally as described in the previous chapter and dried up to the critical point. The critical point was identified by observing when the opaque stage had just begun to form on the surface of the gel. The sample was then removed from drying and immersed in methanol for solvent exchange. After the solvent was exchanged with methanol the gel was supercritically dried as described above. The intact gel was analyzed similarly to the first.

Sample number three was derived by subjecting the gel to a normal aging and drying schedule. It survived the drying procedure intact and was analyzed as described above.

The last sample was taken from the large monolith which was subjected to an extended drying schedule lasting 2 weeks. The large (600ml) monolith broke into several large pieces which were analyzed to determine pore structure. Figure 6.1 outlines the aging and drying schedules for each of the samples tested.

6.1.2 Results and Discussion

Table 6.1 shows the variation in surface area, pore volume and average pore radius for each of the samples. Figures 6.2 through 6.5 show the isotherms and pore radius distributions of the four samples. As might be expected, the surface area decreases dramatically as the aging process continues. The most significant drop in surface area is between sample #1 and sample #2. This is understandable as it is during this time frame that the bulk of the aging process occurs. At the critical point (sample #2) all of the low temperature aging is completed and a significant amount of time has been spent at the drying temperature of 103 °C.

Consistent with acid catalysis of silicon alkoxides, the gel likely consists of small (3nm) colloidal particles immediately after gelation. Particles this small can be expected to have significantly greater solubility than bulk silica. This combined with high temperatures can be expected to accelerate the Ostwald ripening of the internal surface of the gel. As the aging process continues the texture of the gel coarsens and the ripening process slows. Samples 3 and 4 show a more moderate decrease in surface area only because the bulk of the aging process is completed by these stages.

The pore volume depends primarily on how the gel is dried. Sample one is characteristic of aerogels with a very large surface area and a large pore volume. Surprisingly, however, the average pore radius is only about 100Å. By the time the gel reaches the critical point in sample 2 most of the aging process is over and most of the shrinkage has been completed. The analysis of sample 2 closely resembles the pore

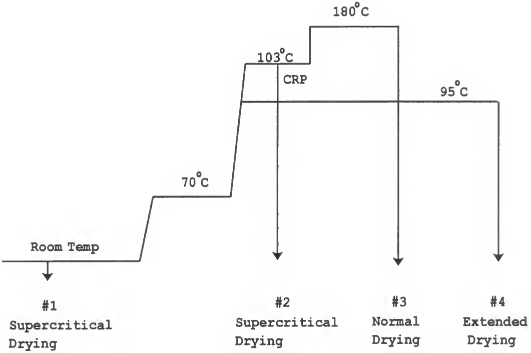

Figure 6.1. Schematic of aging and drying schedule for four gels taken from the same large pore formulation. Sample #1 was supercritically dried shortly after gelation. Sample #2 was supercritically dried after reaching the critical point (CRP) in the normal drying schedule. Sample #3 was analyzed after a standard drying schedule and sample #4 after extended drying due to the large bulk of the gel monolith.

Table 6.1. Pore characteristics of standard 200Å gels at various stages of aging/drying.

Sample	Surface Area (m^2/g)	Pore Volume (cc/g)	Average Pore Radius (Å)	Adsorption Peak Radius (Å)	Desorption Peak Radius (Å)
Sample #1 2:45 hrs Supercritical Drying	1020	5.095	99.93	(133.6) broad	52.5
Sample #2 Critical Point Supercritical Drying	186.1	1.97	211.4	231.6	135.9
Sample #3 Normal Aging and Drying	158.5	1.59	200.7	280.0	152.3
Sample #4 Extended Drying Schedule (2 weeks)	101.6	1.90	373.3	675.4	263.4

a.) Isotherm for Sample #1 (KP70826)
Post Gelation Aerogel

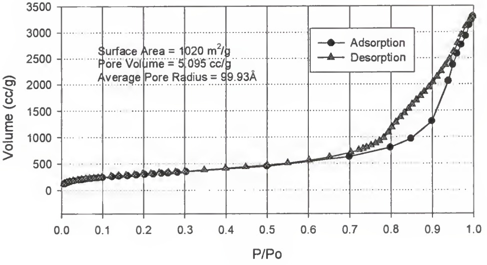

b.) Pore Size Distribution

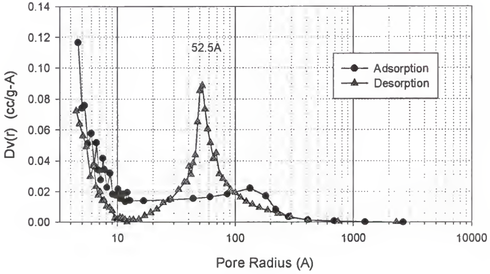

Figure 6.2. Nitrogen adsorption data for sample #1 (KP70826) solvent exchanged shortly after gelation and supercritically dried. a.) Isotherm. b.) Pore size distribution.

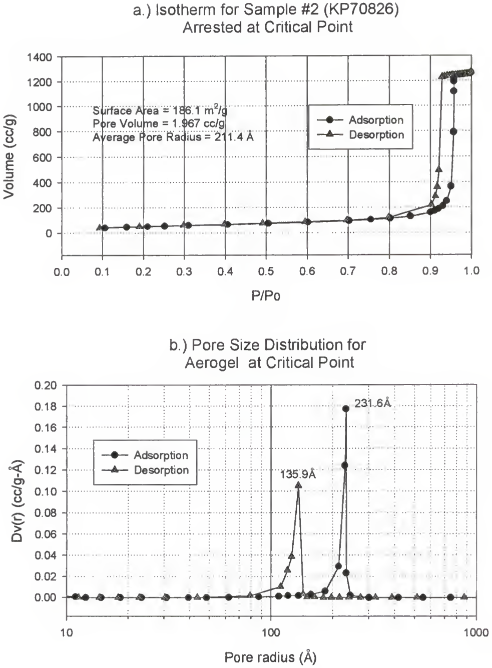

Figure 6.3. Nitrogen adsorption data for Sample#2, solvent exchanged after reaching the critical point and then supercritically dried. a.) Isotherm. b.) Pore size distribution.

a.) Isotherm for Sample #3 (KP70826)
Standard Drying Schedule

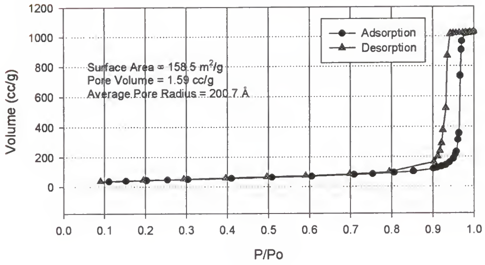

b.) Pore Size distribution for KP70826
Standard Drying Schedule

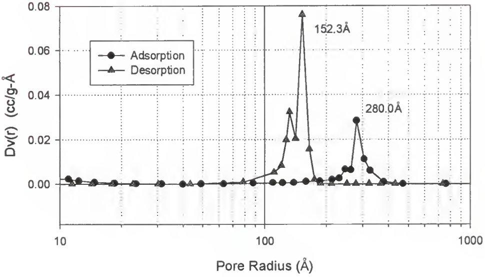

Figure 6.4. Nitrogen adsorption data for Sample #3, dried with standard drying schedule. a.) Isotherm. b.) Pore size distribution.

a.) Isotherm For Sample #4 (KP70826)
After Extended Aging

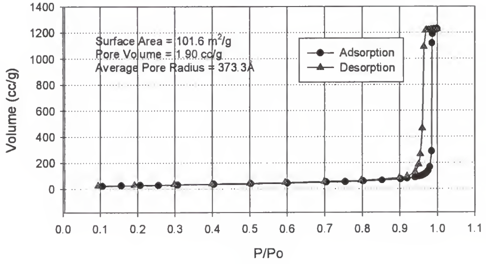

b.) KP70826 Extended Aging
Pore Size Distribution

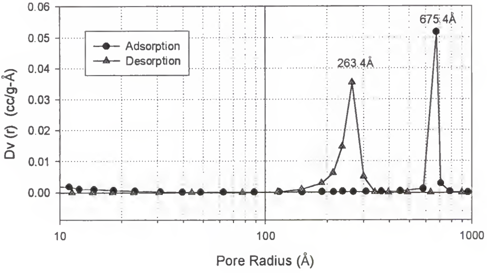

Figure 6.5. Nitrogen adsorption data for Sample #4 after 2 weeks extended aging and drying schedule. a.) Isotherm. b.) Pore size distribution.

structure of sample 3 even though they were dried by different means. The resemblance between the two gels substantiates the two assumptions made at the beginning of this experiment (i.e., that aging slows or ceases upon replacing the solvent with alcohol and that the supercritical drying process preserves the pore morphology of the gel at the time of solvent exchange). The increase in pore volume with extended aging seen in sample 4 can be attributed to the increased stiffness of the gel network as aging continues. With a stiffer network, the gel shrinks less on drying resulting in a larger pore volume.

Since the average pore radius is a ratio between the pore volume and the surface area assuming cylindrical pore shapes, it is not always representative of the actual size of the pore openings but can vary with the pore size distribution (pore volume increases as the square of the radius), pore shape (ink bottle shaped pores produce larger volumes with the same entry diameter) and the surface roughness (surface areas increase rapidly with surface roughness). Thus the average pore radius almost always falls above the peak desorption pore radius which more closely represents the pore entry size.

The isotherms for the four samples show the effect of the aging process on the adsorption of nitrogen and infer the changes that occur as aging proceeds. The isotherm for sample one (Figure 6.2) shows a broad adsorption/desorption range indicative of either a broad range of pore sizes or, using a colloidal model, considerable variability in the curvature of colloidal clusters. As the aging/drying time increases, there is a distinct steepening of the isotherms, displacement towards higher relative pressure and a narrower adsorption-desorption gap.

The pore size distributions paint a similar picture. As aging continues, the pore size gets larger and the distribution tends to become more narrow. Particularly notable is the change in the pore size distribution between sample 1 and sample 2 in which the bulk of the aging process has already taken place. Figure 6.6 shows the pore size distributions for all four samples on the same axis for comparison.

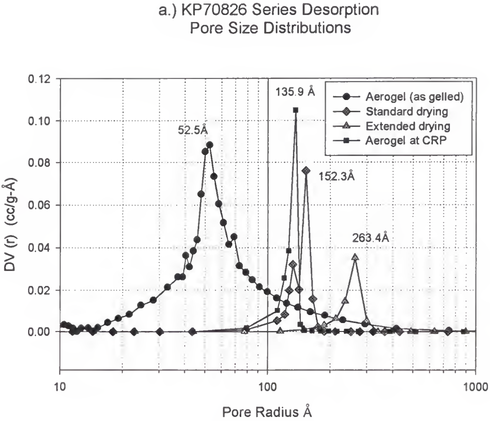

Figure 6.6. Desorption pore size distributions for HF catalyzed gel dried by four different methods. Supercritical CO_2 drying was applied to two gels, one shortly after gelation and the other at the critical point. The third gel was dried with the standard drying schedule and the last was part of a large monolith dried over a period of two weeks.

6.1.3 Conclusions

This experiment demonstrates the usefulness of critical point drying in determining the pore morphology of silica gels as it changes in response to the aging and drying process. The pore structure of gels in the early stages of aging can be preserved by methanol replacement, and then analyzed by nitrogen adsorption after supercritical drying. Results demonstrate a classical Ostwald aging process whereby the surface area decreases with time, temperature and the increased water concentration. The pore volume is dependent primarily on the capillary induced shrinkage of the gel monolith which in turn is dependent on the size of the pores, the stiffness of the network and the drying method.

6.2 Pore Size Modification by Sacrificial Aging

In the course of several attempts to reinforce gel monoliths, it was discovered that aging a gel in the presence of a sacrificial silica donor resulted in smaller pore sizes and denser gel monoliths. Figure 6.7 is a diagram of the process as applied in a preliminary experiment. The large pore gel is modified toward higher surface area, smaller pore volume and a smaller pore radius while the seed gel shows decreased surface area, larger pore volume and a larger average pore radius (as would be expected through Ostwald ripening). Figure 6.8 shows the pore size distribution of both gels before and after the aging treatment. Note that although the pore size distribution of the seed gel grows larger, that of the large pore gel gets dramatically smaller.

This procedure represents a possible avenue for increasing the surface area of dried xerogels by incorporating an additional source of silica in the aging process. There are at least two possible causes for the effect. It's possible that silica is being deposited from the seed gel into the gel being aged in such a way as to increase the surface area (and possibly increasing the thickness of the pore walls). Another possibility is that the presence of the seed silica serves only to retard the aging of the gel as it is dried. As evidenced by the

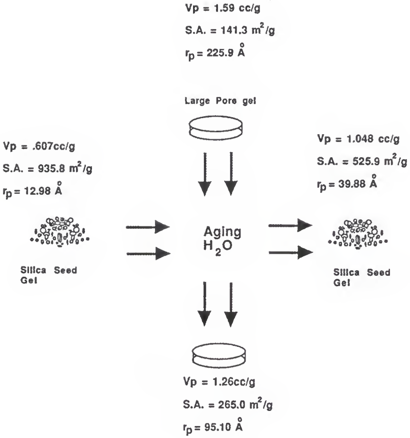

Figure 6.7. Schematic showing the pore modification of a large pore gel aged and dried in the presence of a high surface area "seed" gel.

experiment in section 6.2, the wet gels start out with a very large surface area (1020 m^2/g in the case of sample 1) which dramatically decreases during the aging and drying process. Thus higher surface areas are either being created by aging with a silica “donor” or simply preserved throughout aging process. In either case, the result is a dried gel with a greater surface area and smaller pore volume. The following experiment examines the aging of a 200Å formulation using a high surface area silica gel donor.

6.2.1 Experimental

In this experiment a standard 200Å batch of gels was prepared according to the same procedures in section 6.1.1. They were cast in 60ml PMP containers with Polypropylene screw on caps, aged at room temperature for 2 days and then aged at 70° C for 24 hours per standard procedure. Each gel consisted of 15ml of sol which has a nominal silica content of 1.5 grams. The seed gel was a commercial silica gel powder produced by Aldrich. Nitrogen adsorption was performed to characterize the seed gel. It had a surface area of 400m^2/g, a pore volume of 0.7618 cc/g and an average pore radius of 38.05Å. Twelve aged gels were separated into two groups of six each. To each gel of the first group was added 1.6 grams of seed gel and 40 ml of deionized water. The second group served as the control group and was aged under the identical conditions without the seed silica. Since the aged gels still contained pore liquor from the gelation process the resulting solutions were acidic with a pH of 1.85±.06.

All of the gels were tightly capped to prevent evaporation and placed in an oven at a constant temperature of 90°C to age. They were aged for varying amounts of time up to a maximum of 200 hours. After aging, the gels were cooled, washed in deionized water and placed in a Teflon drying container. The standard drying schedule depicted in Figure 6.2 was used to dry the gels.

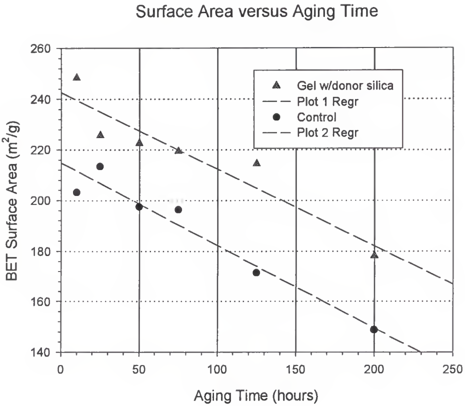

Figure 6.8. The change in BET surface area as a function of time for a standard 200Å formula gel aged with 1.6 grams of a high surface area silica gel. The control is from the same batch but aged without the seed gel.

6.2.2 Results and Conclusions

Figure 6.8 shows the change in surface area of the gels with respect to aging time. The surface area for the gels aged with the high S.A. silica seed is significantly larger than that of the control gels throughout the aging process. Both the silica seeded gels and the control gels show a decrease of surface area with aging time as one might expect from the Ostwald ripening process. The general slope of the curves for both sets of gels is similar.

The plots of pore volume and average pore radius shown in Figure 6.9 are less definitive. The pore volume after drying is not directly related to the change in surface area but is determined to a large extent by the pore size (capillary forces), stiffness of the gel at the critical point, and the conditions of drying. There are several interesting aspects of the pore volume curves. The gels aged with the silica donor have smaller pore volumes in all cases. This can be indicative of seed silica being deposited in the gels and thus physically reducing the pore volume or simply the result of increased shrinkage during drying. However, contrary to this trend one would expect the deposition of additional silica in the gel to fortify the pore walls and fill in high radius necks between particles thus increasing the stiffness of the gel. This would tend to increase the pore volume during drying. The other interesting aspect of the pore volume plot is the way in which the pore volume of both the seeded gels and the control gels mirror one another throughout the aging process. Random variance in aging or drying conditions would not tend to produce curves of identical shapes as depicted. The maximum pore volume at 50 hours is the most intriguing and may indicate a point of particular significance. The average pore radius shows a general trend upward with aging time. Since the average pore radius is determined by the ratio of pore volume to surface area, it looks very similar to the pore volume plot. Because of the large number of variables in the aging and drying process, it

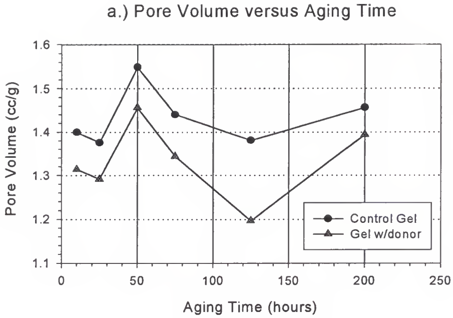

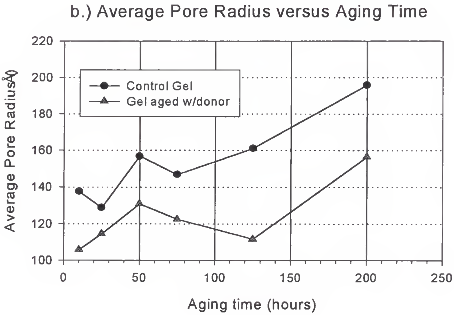

Figure 6.9. BET data for gels aged with and without added donor silica. a.) Pore volume as a function of aging time. b.) Average pore radius for the same gels as a function of aging time.

is difficult to draw firm conclusions regarding the addition of seed silica to the aging solution. It is clear that doing so results in a higher surface area gel with a lower pore volume and consequent smaller pore radius. It is not immediately clear that this is due to the deposition of silica from the donor gel. This experiment was performed on very fragile wet gels which could not be accurately weighed before and after aging. Although the transfer of silica from the seed gel to the aging gels could account for the changes observed, they might also be due to a simple retardation of the aging process due to a higher concentration of soluble silica. Consequently, the experiment was repeated using dried gels rehydrated with a simulated pore liquor.

The second experiment was conducted using the same procedures and aging times as the first. The gels in the second experiment were first dried and weighed so that any deposition of silica during aging could be detected. After aging the gels were redried and weighed. In all cases, the weight of the redried gels was nearly identical or slightly less (0 to -3%) than the initial weight indicating that there was no gain of silica.

Based on these results it can be concluded that *the smaller pore size observed for gels aged with a sacrificial silica source is due to a retardation of the aging process and not to the deposition of additional silica*.

6.3 Effect of Gelation Volume on Pore Texture

In this experiment the gelation volume of a silica gel monolith is altered by adding methanol in different amounts to a fixed quantity of sol, allowing the resulting solution to gel, and then subjecting the gel to a standard aging and drying schedule. Each gel has the same amount of solid silica and the same initial chemical environment. By diluting the sol with methanol, the gelation time is increased as is the volume of the wet gel. After aging and drying, the gels are analyzed to determine the effect of gelation volume on the final pore texture.

6.3.1 Experimental

In this experiment the standard 200Å pore radius formula was again used. The starting solution was cooled to 16°C and the temperature rose to 35°C after the addition of the TMOS. After 5 minutes of mixing, 10 milliliters of sol was filtered into 60ml PMP molds. 99.9% methanol (Fisher Scientific) was added to each jar in increments of 1 milliliter and the molds were tightly capped and then set aside to gel. Gelation volumes ranged from 10ml to 20ml. All of the gels contained the same amount of silica solids. As expected the dilution of the sol slowed down the gel time in direct proportion to the added methanol as depicted in Figure 6.10. The solutions had all gelled within 2 hours and were subsequently aged for 2 days at room temperature. After room temperature aging, the gels were placed in an oven and aged for another 24 hours at 70°C. Due to the mechanical weakness and high methanol content of the gels they were left in the PMP containers and heated at 70° until dry. One gel (20ml gelation volume) was dried under standard conditions (see figure 5.2) to assess the effect of the unconventional drying schedule. They were they transferred to Teflon containers and heated to 180°C to drive off physically adsorbed water and residual nitric acid before BET analysis.

6.3.2 Results and Discussion

Figure 6.11 shows the results of the nitrogen adsorption pore texture analysis of the gels with the surface areas and pore volumes plotted as a function of gelation volume. It is clear that within the limits of nitrogen analysis (approximately ±5%), there is no significant change in either of these values as the gelation volume is varied through the addition of methanol. The gelation volume varies by factors of up to twice the initial volume, however by the time the gels are dried, they all achieve roughly the same surface area and volume. During the drying process, the gels shrink as the pore liquor evaporates

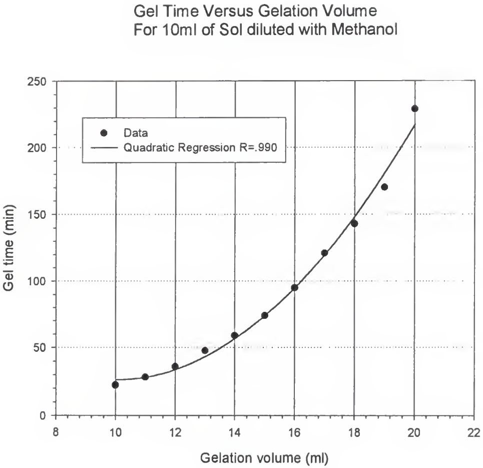

Figure 6.10. Gelation time versus gelation volume. Approximately 5 minutes after mixing, 10 milliliters of sol was diluted with methanol to the indicated volume and allowed to gel.

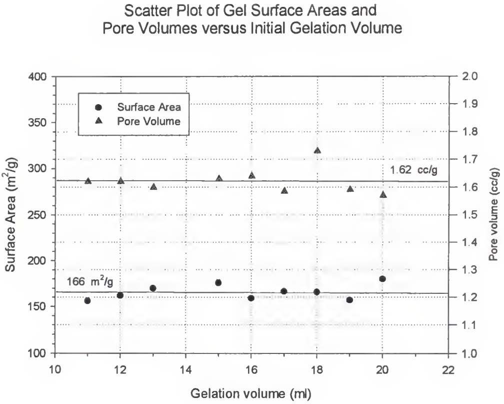

Figure 6.11. Surface area and pore volume of silica gels composed of 10 ml of a standard sol diluted with methanol to the indicated volume and allowed to gel. Gels were all aged according to the standard schedule in Figure 5.2.

until such time as the stiffness of the silica network is sufficient to resist the capillary pressures. As discussed in Chapter 2, when the gels reach the critical point the liquid meniscus begins to penetrate the pores. This is the beginning of the opaque stage. For these gels, such a large decrease in volume during drying necessitates a dramatic rearrangement of the aggregates - essentially a collapse of the structure into the smaller volume. The pore radius is plotted versus the gelation volume in Figure 6.12. All of the gels (except the 20ml which was dried at higher temperature) have average pore radii within 15Å of the mean at 198.3Å.

The relative uniformity of surface area is also significant. If one views the gel as a colloidal body of uniform sized colloidal spheres or aggregates, the surface area could be expected to change due to Ostwald ripening at a rate dependent on the size of the colloids and the solubility of the silica in solution. This rate would be similar under similar conditions of aging and drying regardless of the initial arrangement of the colloids

6.3.3 Conclusions

These results suggest the following scenario. The gels are made up of colloidal particles which during the aging process form agglomerates and are subjected to Ostwald ripening. As stress is applied by capillary forces, these aged agglomerates collapse into a randomly packed structure which is further strengthened (coalesced) by additional aging as the gel dries at elevated temperatures. When the gel achieves sufficient strength, the collapse of the network ceases, the pores empty of liquid and the final pore structure is preserved in the dry gel.

The interesting aspect of this scenario is that such a collapse requires fracture of whatever necks may have already formed between agglomerates. Thus the shrinkage of the gel can be viewed as a process by which the necks between agglomerates progressively collapse and are reformed (by Ostwald ripening) until the network strength reaches a

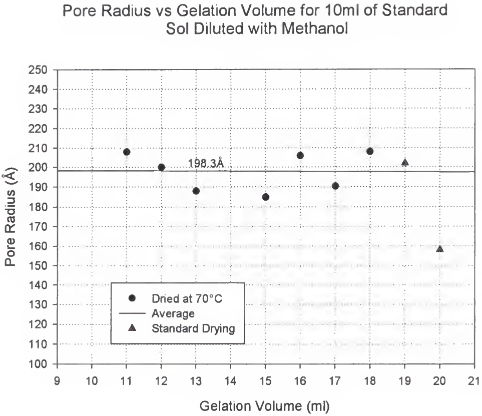

Figure 6.12. Pore radius versus gelation volume for gels diluted with methanol and allowed to gel at different volumes.

critical value (the critical point), at which point the gel is strong enough to resist the capillary pressures of the penetrating liquid. If this is indeed the case, it is no wonder why silica gels are so difficult to dry intact! This scenario also suggests a strategy for strengthening gels. If the gel is brought to the critical point and allowed to age predominantly at this minimum volume, it may be possible to produce gels more resistant to fracture.

CHAPTER 7

PROPERTIES OF LARGE PORE ACID CATALYZED GELS

The large pore gels discussed in the last two chapters have properties that are essentially extensions of those reported for similarly synthesized gels of smaller pore size. Hench and West have done an extensive investigation into the properties of acid catalyzed silica gels in pore sizes ranging from 12Å to 90Å in pore radius (Hen90a, Ara95). These will be cited for comparison purposes. The difference in the large pore gels is a much larger pore size than previously achieved, a corresponding decrease in bulk density and greater pore stability at high temperatures.

The texture of dried and stabilized HF derived silica gels is primarily measured by BET as discussed previously in Chapter 3. The texture of wet gels as elucidated through the use of SAXS, SANS and Si^{29} NMR gives insight regarding the development of the gel structure but the results of supercritical drying of HF gels in Chapter 5 indicate that for a given gel formulation it is often the aging and drying process that is the principal determinant of the final dried glass product (Orc86, Orc87). The behavior of gels of various pore sizes towards stabilization and densification is similar but due to differences in texture and surface properties (such as degree of hydroxylation) it occurs at different temperatures.

The mechanical properties of the dried and stabilized gels tends to be a function primarily of the bulk density. Large pore gels have a progressively lower bulk density and hence tend to be weaker than smaller pore sizes. However, they still retain enough strength to be useful for a variety of applications. Microhardness is used to monitor the change in the porous gel strength as the gels are stabilized at different temperatures. Since the properties of bulk silica are well known, and silica gels are essentially a composite of silica and air, the hardness and bulk density are directly related. For low density gels such as the “standard” large pore system examined here, mercury porosimetry can be used to directly measure the bulk modulus of dried and stabilized gels up to the point where densification becomes significant.

Optical properties of silica gels are dominated by the scattering properties of the gels which tend to be related to the pore size. There is a temptation to view silica gel monoliths as a concentration of silica spheres of different sizes, however this view is overly simplistic as it neglects multiple and cooperative scattering effects. Turbidity of the gels is a useful concept that can be empirically derived and used to predict the average pore size of gel monoliths. At present it can be applied only to those gel systems which are fabricated under similar conditions. Residual reagents or adsorbed water on the gel surfaces are apt to affect the turbidity profile.

The environmental stability and chemical properties of monolithic silica gels is primarily a function of texture and heat treatment. It has long been recognized that gels are hygroscopic in proportion to their surface area and (surface) silanol concentration (Wal91). Atmospheric humidity is deleterious to the long term stability of gel monoliths which tend to crack over time in ambient environments even when stabilized at high temperatures. The large pore gels with their lower surface areas and large pore sizes absorb less moisture and are much more stable in ambient conditions over long periods.

7.1 Texture of Large Pore Gels

The texture of HF catalyzed gels has been compared to that of base catalyzed gels as being more colloidal in nature than acid catalyzed gels which tend to have a more ramified texture (Bri90). The results of this investigation confirm that for this gel system,

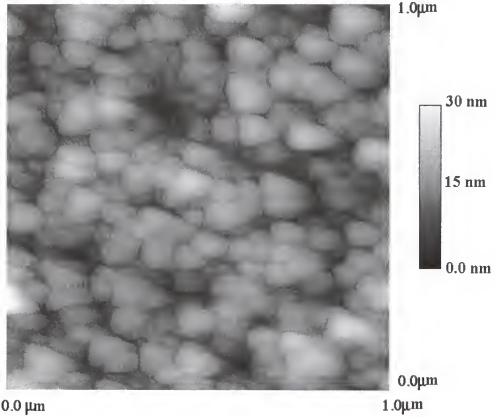

Figure 7.1. AFM image of large pore gel showing the colloidal texture.

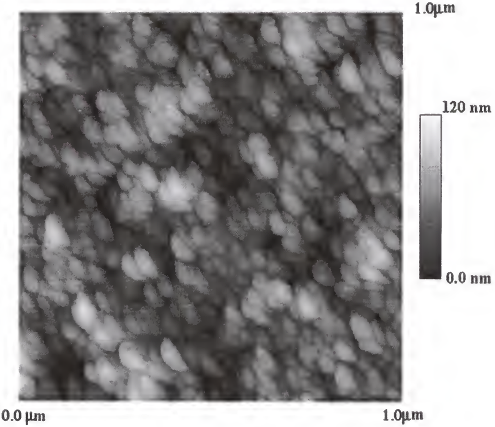

Figure 7.2. AFM image of large pore gel fracture surface showing the colloidal nature of the gel.

the dried gels do indeed appear colloidal. The "standard" large pore gel of Chapters 5 and 6, once dried, consists of relatively large colloidal particles or aggregates 50 to 70 nm in diameter as evidenced by the Atomic Force Microscope (AFM) images in Figures 7.1 and 7.2. The images were taken on a Nanoscope Atomic Force Microscope built by Digital Instruments. The images are taken of uncoated fracture surfaces of gels from two different batches made using the standard 200 Å formula and dried at 180°C. The images were made in tapping mode with a one square micron scan size. The colloidal appearance is confirmed by the high resolution SEM photos of another as-dried large pore gel shown in Figures 7.3 and 7.4. The spheres in the AFM image appear slightly oblate, a common artifact in AFM images. No corresponding oblateness is observed in the high resolution SEM images. The fracture surface in Figure 7.3 shows the same colloidal nature on a similar scale. The as-cast surface of this gel is shown in Figure 7.4. with what appears to be surface microcracks between colloidal aggregates. The BET analysis of the gels are all similar with average pore diameters in the vicinity of 200Å. The BET data for the dried gel imaged in the SEM photos is shown in Figure 7.5 as an example. Gels made with this formulation typically have surface areas of 160±10 m^2/g, pore volumes of 1.65±.05 cc/g and average pore radii of 200±20 Å.

Neither the AFM or the SEM images can adequately depict the size and the shape of the pores themselves but it is probable that fracture occurs coincident with the pore location. Consequently, the image is representative of the morphology of the pore walls. It is apparent from the size and shape of the colloidal particles that the pores cannot be (perfectly) cylindrical in shape yet the BET isotherm in Figure 7.5 has a very distinct Type A (cylindrical) hysteresis loop. This phenomenon was discussed in Chapter 3 with respect to a large pore gel that had been extensively aged. At the high relative pressures (>0.90) necessary for the adsorption of nitrogen for these large pores, there will be a relatively thick layer of adsorbed nitrogen over the entire surface of the pores. The exact thickness of the statistical layer at this pressure will vary according to the curvature of the

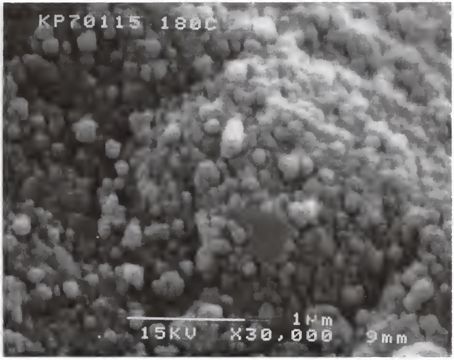

Figure 7.3. SEM photo of the large pore gel fracture surface.

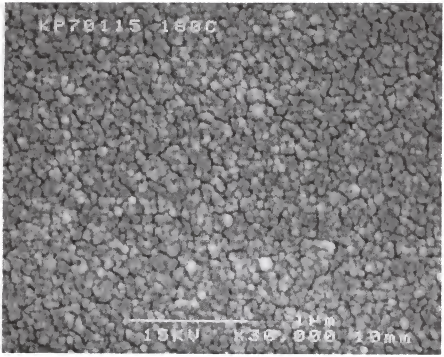

Figure 7.4. SEM photo of the as-cast surface of a dried large pore gel.

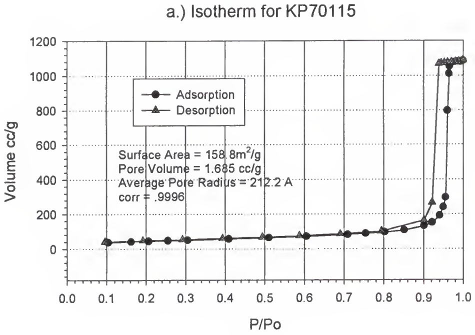

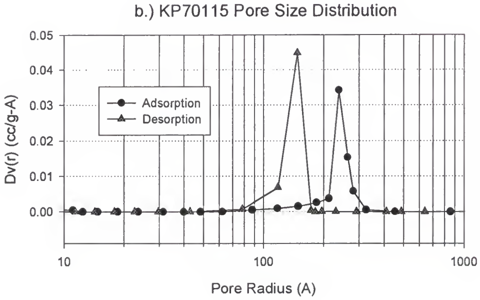

Figure 7.5. Nitrogen adsorption data for a typical large pore (200Å) gel. a.) Adsorption and desorption isotherms. b.) The pore size distribution.

surfaces. Thus in the necks between particles (with negative curvature), it will be thicker and over the convex shapes of the particles it will be thinner. The overall effect is to drive the adsorbate-covered interior of the pore towards a cylindrical shape as the relative pressure increases. Ultimately, the curvature of the "core" of the pore that drives the adsorption of nitrogen as the relative pressure increases. This process is illustrated in Figure 7.6 and explains why the pores appear more cylindrical as they get larger.

7.2 Large Pore Gel Texture as a Function of Heat Treatment

Two batches of large pore gels were selected to study the effect of stabilization treatments on the evolution of the pore texture. Both batches were made according to the formulation in Chapter 5, and aged and dried with the schedule in Figure 5.2. Seven 25mm by 6mm samples were selected from each batch and stabilized at different temperatures under ambient conditions according to the schedule in Figure 7.7. All were held at temperature for 10 hours prior to cooling. BET data was collected on the Autosorb 6 manufactured by Quantachrome Inc. using the procedures outlined in Chapter 3. Bulk density was determined by mercury pycnometry after 12 hours of outgassing at 160°C in a vacuum oven. Structural density was determined by helium pycnometry using a helium micropycnometer (Model QPY-1) manufactured by Quantachrome, Corporation. Measurements were reproducible to ±3%. Since the large pore gels can be rehydrated without cracking, water pycnometry was used to cross-check the pore volume given by nitrogen adsorption. Pore volumes measured in this manner were usually slightly lower than nitrogen adsorption measurements but all agreed to within ±7%.

7.2.1 Results and Discussion

Figure 7.8 shows the change in surface area and pore volume as a function of stabilization temperature. The surface area of the large pore gels remains relatively

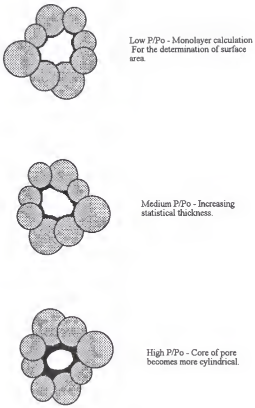
Low P/Po - Monolayer calculation For the determination of surface area.
Medium P/Po - Increasing statistical thickness.
High P/Po - Core of pore becomes more cylindrical.

Figure 7.6. Schematic of how large mesopores pores can appear more cylindrical at high relative pressures during nitrogen adsorption analysis.

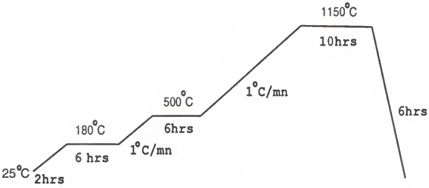

STANDARD DENSIFICATION SCHEDULE

Figure 7.7. Stabilization schedule used to heat treat and sinter large pore gels prior to analysis.

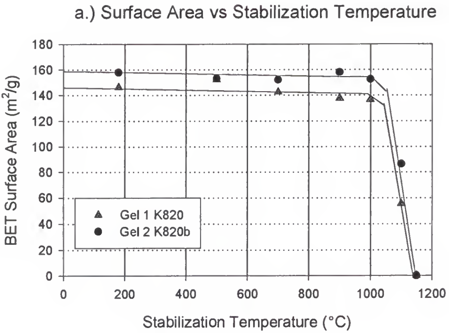

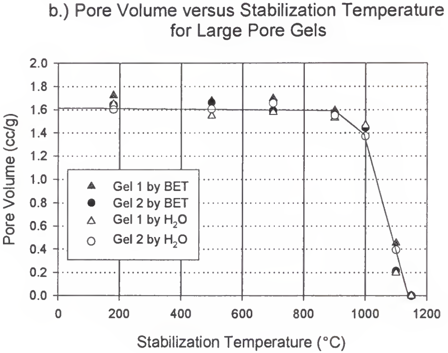

Figure 7.8. Pore characteristics of large pore gels as a function of stabilization temperature. a.) Surface area. b.) Pore volume.

constant until stabilization temperatures in the vicinity of 1000°C at which point there is a rapid drop as the gels begin to densify. The pore volume in figure 7.8(b) shows a similar trend but there is some contraction of the gel starting between 900 and 1000°C. The change in pore volume (contraction) is reflected in the average pore radius plotted versus temperature in Figure 7.9. Figure 7.10 shows the changes in structural density and bulk density as a function of temperature. Structural density measurements show a slight rise in the mid temperature region before dropping towards the 2.20 g/cc literature value for fused silica (Var94). As we shall see in the next section, this is consistent with trends established by other investigators. Bulk density begins to rise in the vicinity of 1000°C reaching the bulk silica value of 2.20 g/cc by 1150°C. It is apparent from these trends that for this heating schedule (i.e. 1°C heating rates and a 10 hr hold at temperature) sintering commences in the vicinity of 1000°C but requires up to 1150°C for full densification. Although there is a slight contraction in the 1000°C samples, the pore structure remains virtually unchanged until temperatures exceed 1000° C as shown by overlaying the plots of the desorption pore size distribution. (Figure 7.11(a)) The isotherms plotted in Figure 7.11(b) demonstrate that even after sintering commences, the pores still display a cylindrical shape. As sintering occurs there is a drop in pore volume and a decrease in pore size with a corresponding broadening of the pore size distribution. (Figure 7.12) Heating the glass to 1150°C brings about full densification producing a clear hard glass with no porosity and with the density of fused silica.

It is important to remember that for silica gels, the heating rate can affect the sintering characteristics of the gel glass. The viscosity of the silica during densification is significantly lowered by the presence of chemically adsorbed water, primarily in the form of surface silanols on the pore walls. The water content is governed by several factors including gel formulation, texture, and the heating rate during densification. The average concentration of surface silanols on fully hydroxylated silica surfaces established by

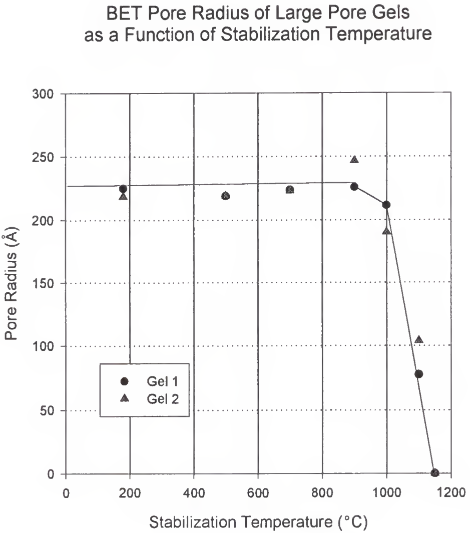

Figure 7.9. Pore radius versus stabilization temperature for two series of large pore gels.

a.) Structural Density of Large Pore Gel versus Stabilization Temperature

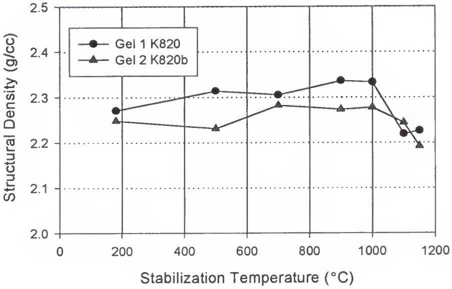

b.) Bulk Density versus Stabilization Temperature

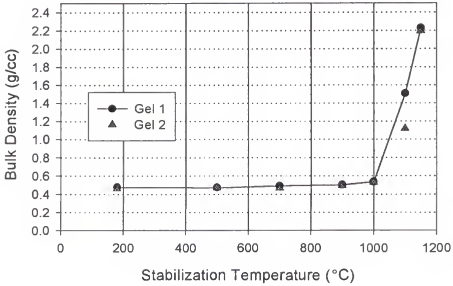

Figure 7.10. Large pore gel density as a function of stabilization temperature. a.) Structural density. b.) Bulk density.

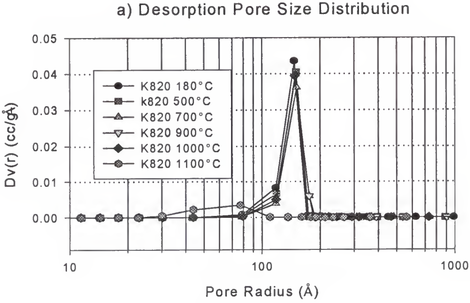

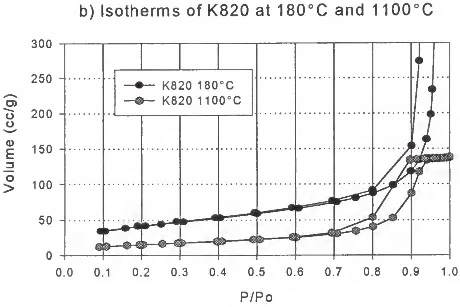

Figure 7.11. Overlaying the nitrogen adsorption data for different stabilization temperatures shows the evolution of pore texture during stabilization. a.) Overlay of the desorption pore size distributions demonstrates that there is little change in pore texture until sintering begins above 1000°C. b.) Comparison of isotherms of a dry gel and a gel stabilized at 1100°C shows that cylindrical hysteresis is preserved even after sintering commences.

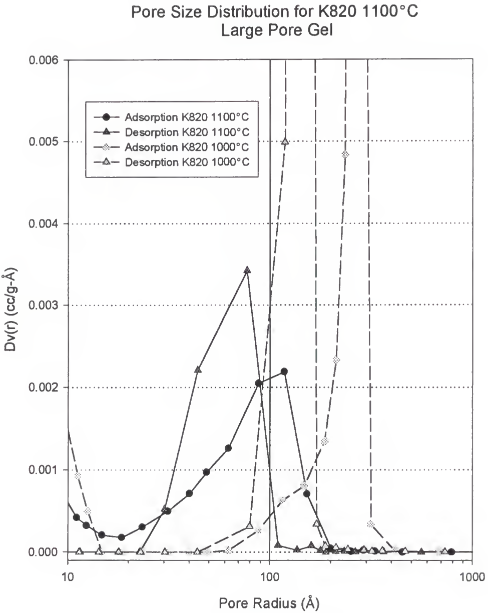

Figure 7.12. As the gel sinters at higher temperatures, pore volume and pore radius decrease while the pore size distribution broadens.

Zhuravlev is 5 silanols/nm^2 (Zhu94). Thus gels with low relative surface area should have a proportionally lower water content. Surface area is also the principal thermodynamic driving force in the sintering process. Large pore gels with a lower surface area inherently have less water and a lower driving force towards densification. In addition, the large pores and greater permeability of these gels allow the escape of water released during heating, particularly if the heating rate is slow. Fluoride content also contributes to higher densification temperatures, primarily through the displacement of water. In fact fluoride has been promulgated as an alternative to chlorine dehydration treatments due to the tendency for chloride treated glasses to reboil at higher temperatures (Rab86b). As discussed in Chapter 4, the fluoride content of the HF catalyzed gels is concentrated on the surface of the pores displacing the silanol groups.

7.2.2 Comparisons to Smaller Pored Silica Gels

Wallace and Hench conducted a detailed study of the effect of stabilization treatments on the pore texture and surface properties of acid and HF catalyzed gels of smaller pore size (Wal91). Their work incorporated gels with pore radii of 12Å through 90Å. Their gels were prepared in a similar fashion to the large pore system described here but differed in the details of solvent mixtures, pH and gelation temperature . The 12 Å gels were made without HF catalyst. The details of the heat treatment were slightly different with a faster heating rate (5°C) between 12 hour isothermal holds. Still, the fabrication and heat treatments are similar enough to make a direct comparison between gels of different pore size.

Figure 7.13 shows the data for surface area and average pore radius plotted alongside the large pore data. The surface area of the 12Å gels decreases more or less monotonically with increasing temperature. It is perhaps significant that this is the only gel of the series with no added fluoride and of course has the highest initial surface area by a.) Surface Area versus Stabilization Temperature

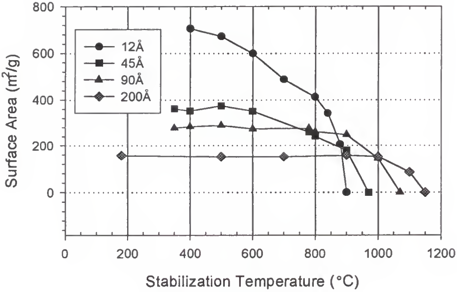

b.) Average Pore Radius versus Stabilization Temperature

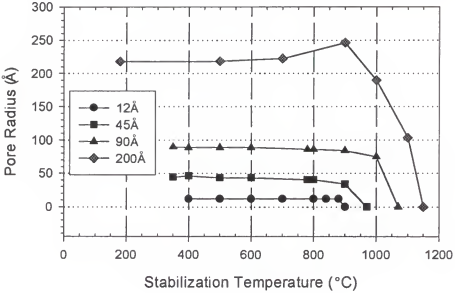

Figure 7.13. Comparison of pore texture for a variety of pore sizes. a.) Surface area versus stabilization temperature for a variety of pore sizes. b.) Pore radius versus stabilization temperature. (Small pore data from Wallace (Wal91).)

far. The HF gels all appear to have a stable surface area up to the temperature at which sintering begins. The sintering temperature is clearly related to the surface area/pore size. Figure 7.13(b) shows the data plotted as a function of pore radius rather than surface area while Figure 7.14(a) shows the change in bulk density as a function of stabilization temperature for the four pore sizes. Again, the 200Å series gel is consolidated at the highest temperature. The increased time spent at higher temperature facilitates the removal of water from the gel surface and allows densification under ambient conditions without bloating.

7.2.3 Conclusions

It is hard to say whether the large pore system here represents the maximum pore size one can achieve with xerogels using conventional processing. Attempts to increase pore size further using still greater concentrations of fluoride have produced pore sizes as large as 350Å. However, the increase is primarily a function of reduced surface area. The pore volumes are only marginally higher. The same increase can be accomplished by simply aging the 200Å system for extended periods. This strategy has produced monoliths with pore radii as great as 450Å. In both cases the increase in pore size results in a dramatic loss in transparency thus limiting the use of such gels as optical substrates.

It is significant that if the silica gel is to be used as a porous substrate (as for example in a catalyst support), the large pores extend the temperature range to which the gel can be operated albeit at the sacrifice of surface area. For catalyst supports there is the added advantage however, of significantly greater permeability due to the large pore size.

7.3 Microhardness of Porous Monoliths

Microhardness measurements were conducted on the large pore gel samples at each of the stabilization temperatures discussed in the previous section. The instrument

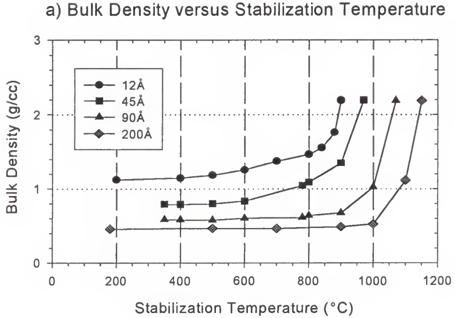

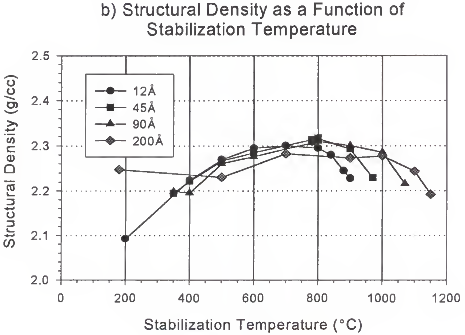

Figure 7.14. Bulk and structural density as a function of stabilization temperature.
a.) Bulk density. b.) Structural density.

was a "Micromet" microhardness tester manufactured by Leco, Inc.. Hardness values were measured using a Knoop diamond shaped indentor using a load of 10 grams and a indentation time of 15 seconds. Ten measurements were made at different locations on each sample. There was considerable variation (±8%) in the measurements made on the low bulk density porous substrates (those stabilized at < 1000°C). This can be attributed to the low strength of the material (near the limits of the instrument) and the porous nature of the glass surface . Similar problems were encountered by Orcel when testing porous silica gels (Orc87). Qualitatively, the microhardness measurements can be used to demonstrate the relationship between mechanical strength and bulk density as sintering commences at 1000°C. In Figure 7.15 the microhardness and bulk densities of two large pore samples are plotted as a function of stabilization temperature. As expected the microhardness of the material increases with bulk density as sintering begins at 1000°C.

7.4 Mercury Porosimetry

Mercury porosimetry measurements were initially made in an attempt to verify pore texture, however it was discovered that the porous monoliths were too compressible to provide accurate pore size measurements. Mercury porosimetry was accomplished using a 0-60kpsi mercury intrusion porosimeter manufactured by Quantachrome Corporation. Samples were outgassed for 12 hours at 160°C under a vacuum and filled with clean mercury in the instrument's fill apparatus. A contact angle of 140° was used for computing pore information. Figure 7.16 is a typical intrusion curve made on a sample stabilized at 500°C. Initially it appears that there is a broad distribution of macropores culminating with a sharp rise in volume at a pressure of 12kpsi. This pressure corresponds to a pore radius of 90Å. Total pore volume of the sample is computed to be 1.49 cc/g. These results are dramatically different from the BET results of 218Å pores and a 1.66cc/g

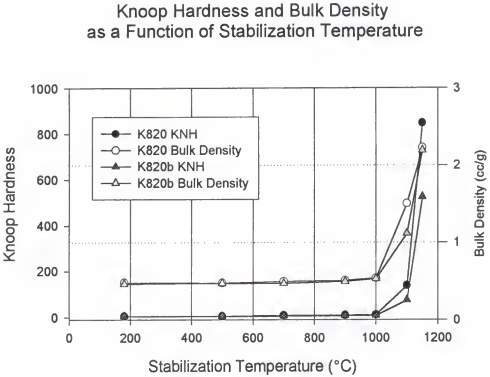

Figure 7.15. Microhardness and bulk densities of large pore gels as a function of stabilization temperature.

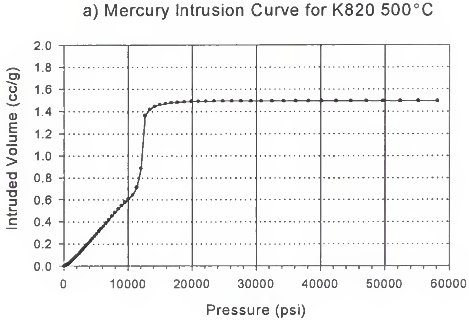

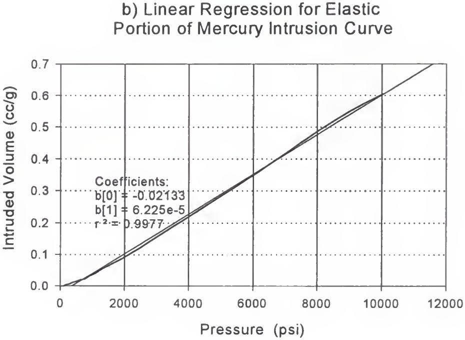

Figure 7.16. a.) Mercury intrusion curve for a typical large pore gel. Note the linear portion of the curve at low pressures where the gel is being elastically compressed. b.) Regression analysis for the elastic portion of the intrusion curve can be used to calculate bulk modulus.

pore volume determined as by nitrogen adsorption. What actually occurs is the isostatic compression of the gel as the pressure of the mercury rises. At 12kpsi the gel stiffness increases to the point at which mercury can intrude and the gel structure relaxes as the pressure on the inside of the gel equalizes with the surroundings. Consequently, the pore size represents the size of the compressed pores (actually the necks) at the intrusion pressure. The pore volume is approximately 10% lower when measured by mercury porosimetry which can be indicative of some irreversible (inelastic) compression of the sample.

Although unsuitable for making pore texture measurements on these samples, the compression of the sample at low pressures does make it possible to estimate the bulk modulus of the gel samples. The bulk modulus K is defined as the ratio of the applied isotropic pressure to the dilatation of the material:

$$P_{iso} = \nabla \cdot K \qquad [7.1]$$

where the dilatation ∇ is defined as the change in volume divided by the volume , or $\nabla=\Delta V/V$. Assuming no mercury intrudes into the pores, the change in volume is measured directly by the mercury porosimeter. The slope of the linear portion of the intrusion curve below ≈12kpsi is proportional to the bulk modulus. The lack of mercury intrusion at pressures below 12kpsi was verified in two ways. There is no residual mercury in samples that do not exceed this pressure. The extrusion curve follows the intrusion curve with little or no hysteresis at pressures below the critical penetration pressure. The fact that the compression is linear below the critical intrusion pressure is also an indicator that the change in volume is due to compression rather than intrusion. (See Figure 7.16(b).)

The bulk modulus can be calculated for large pore gels stabilized at temperatures at or below 1000°C. Above this temperature sintering commences, the pore size and pore volume decrease and the bulk modulus rises dramatically. For samples treated at 1100°C the elastic region is small and is not very linear. Consequently, measurements on these samples are unreliable. For the fully dense samples, the bulk modulus is too high to be measured by this technique.

The results of the measurements are shown in Figure 7.17. Note that despite the similarities in pore texture there is a significant difference in bulk modulus between the two batches with batch K820b higher in all cases. In both cases there is a jump in the modulus starting at about 500°C. This suggests that the degree of surface hydroxylation (chemisorbed water) may have an influence on the modulus. In any case it is clear that the porous substrates have a much lower modulus than that of fused silica (Zar91).

7.5 Optical Scattering in Large Pore Monoliths

Due to the small scale of inhomogeneity (pore size) in the porous sol-gel glasses, their optical properties are dominated by Rayleigh-Gans type scattering. Rayleigh scattering is caused by the diffraction of light off of scattering centers which are small ($<\lambda/4\pi$) with respect to the wavelength of light. The pore sizes of acid catalyzed silica gels normally range between 2.0 and 40 nanometers in diameter which falls in the Rayleigh range for wavelengths in the visible and ultraviolet portions of the spectrum. Large pore gels with pore diameters of 40nm are translucent and have a distinct bluish tinge when viewed from the side but appear yellow to amber colored when viewed in transmission. This is due to the scattering of the smaller wavelengths to the side as light passes through the gels. It is the same phenomenon that causes the sun to appear orange during the sunset (viewed in transmission through the dust filled atmosphere) while the sky appears blue due to the scattered light. Although light scattering has little effect on the physical or chemical properties of the porous gels, it is important when contemplating the use of porous gels for optical sensors, high surface area photocatalysts, or transparent insulating materials. Figure 7.18(a) shows the UV-Visible absorbance spectrum of a typical large pore silica gel (as-dried) monolith. UV-Visible spectra were recorded using a Lambda-9

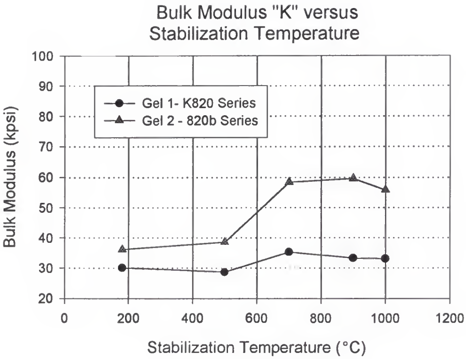

Figure 7.17. The bulk modulus of two large pore gels as a function of stabilization temperature. Values were derived from mercury porosimetry measurements.

UV-Visible-NIR spectrometer manufactured by Perkin-Elmer. Typical samples were monolithic disks approximately 25 mm in diameter and 6 mm thick. The sample surfaces were "as cast". The spectra were not corrected for specular reflectance at the surfaces. For the porous samples the maximum loss due to reflectance is estimated to be less than 2% (based on the refractive index of the sample with highest bulk density).

7.5.1 The Rayleigh Equation

According to Rayleigh, simple scattering of light by particles that are small with respect to the wavelength of light ($d \leq \lambda/4\pi$) can be viewed as a diffraction phenomenon. Such scattering as described by Rayleigh is proportional to the reciprocal of the fourth power of the wavelength ($1/\lambda^4$) according to the following equation:

$$\frac{I_S}{I_O} = \frac{16\pi^2 V^2 N}{d^2 \lambda^4}\left[\frac{n^2 - 1}{n^2 + 2}\right]^2 (1 + \cos^2 \theta) \qquad [7.2]$$

where

I_S = intensity of the scattered light
I_O = incident intensity
d = distance of the detector from the scattering center
λ = wavelength of incident light
N = number of scattering centers
n = ratio of refractive index of scattering center to the matrix
V = volume of scattering center
θ = angle of observation

The Rayleigh equation holds very well for dilute solutions of spherical particles in a homogeneous medium. However, porous silica gel is not such a well-characterized system. Although the primary particles in the initial sol are thought to be spherical colloids, by the time gelation, aging and drying occur these particles have aggregated to a high density of fractal interconnected surfaces throughout the gel. *One cannot assume* a.) UV-Visible Absorbance of as-dried Large Pore Gel

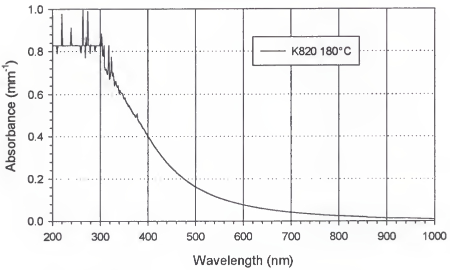

b.) Absorbance versus $1/\lambda^4$ for Large Pore Gel

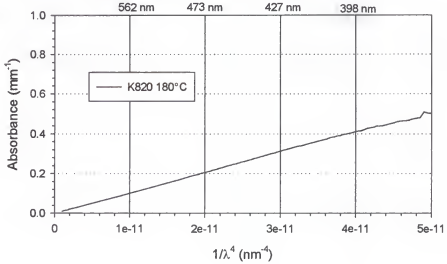

Figure 7.18. UV-Visible spectrum for a typical large pore gel. a.) Absorbance plotted versus wavelength. b.) The same spectrum with the absorbance plotted against $1/\lambda^4$ showing the linear relationship characteristic of Rayleigh scattering.

independent scattering events, single scattering events or smooth spherical scattering surfaces in this material. In spite of these drawbacks, one can see from Figure 7.18(b) that plotting the absorbance of a silica gel against the reciprocal of the fourth power of wavelength produces a straight line. Although the details relating to the nature of the scattering surfaces are unknown, it is without question Rayleigh-type scattering.

7.5.2 Turbidity and Scattering from Sol Gel Glass

Turbidity is defined as the total amount of scattering per unit volume, or the loss in intensity of the primary beam as it passes through the scattering volume (Ker69). It is actually the turbidity of the material that is measured by the UV-Visible spectrometer when a porous sol gel sample is analyzed. Since the cross-sectional area of the beam and the distance to the detector are invariant for the spectrometer used, the scattering volume depends only upon the thickness of the sample. Therefore gels of different pore sizes can be compared and the results interpreted in terms of the density and the texture of the gel. Figure 7.19 displays the Rayleigh slope for several gel monoliths of different pore sizes. All of the gels are acid catalyzed but the conditions of gelation, solvent concentrations and HF concentrations vary. All were dried at 180° C. It was found that the slope decreased with decreasing average pore size and that the relationship between pore size and scattering is approximately linear. (See Figure 7.20.) This suggests the following empirical relationship.

$$\frac{\tau}{l} = \frac{B \cdot R_p}{\lambda^4} \cdot \left(\frac{n^2 - 1}{n^2 + 2}\right)^2 \qquad [7.3]$$

where

τ/l = specific turbidity in mm^{-1} .

B= empirical constant (equal to the slope/ in Figure 7.20).

R_p = average pore radius in nanometers.

n = relative refractive index of the scattering surface (n solid phase/n medium).

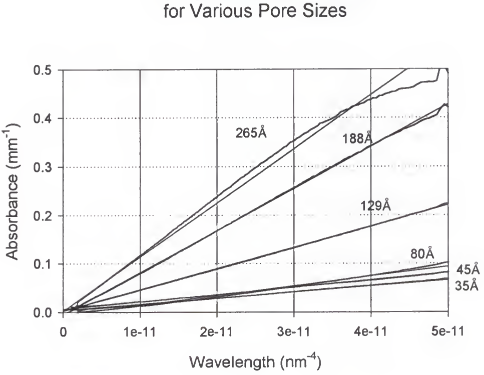

35Å

Coefficients:
b[0]=4.7247e-3
b[1]=1219e+6
r ²=0.9655

45Å

Coefficients:
b[0]=6.6807e-3
b[1]=1492e+64
r ²=0.9873

80Å

Coefficients:
b[0]=-5.4798e-3
b[1]=1979e+6
r ²=0.9938

129Å

Coefficients:
b[0]=2.4341e-3
b[1]=4369e+6
r ²=0.9998

188Å

Coefficients:
b[0]=-4.7915e-3
b[1]=8650e+6
r ²=0.9997

265Å

Coefficients:
b[0]=2.22107e-3
b[1]=1.1127e+10
r ²=0.9929

Figure 7.19. Scattering slopes and regression parameters for acid catalyzed gels of various pore sizes.

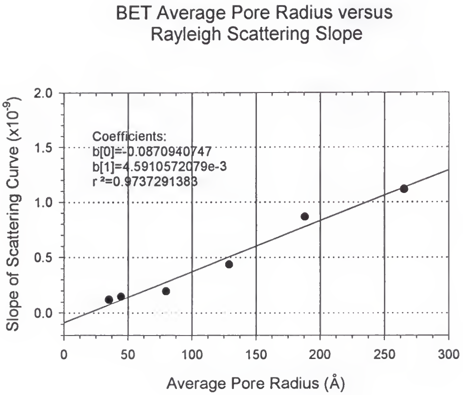

Figure 7.20. Plot of the slope of the scattering curves from figure 7.19 versus the average pore radii of several silica gels with different pore sizes.

It is somewhat curious that there should be a linear relationship between the average pore radius and the turbidity. Remember from Chapter 3 that average pore radius is a property that is defined by assuming cylindrical pore structure.

$$R_p = \frac{2 \cdot V_p}{S.A.} \tag{7.3}$$

It is used as a convenient way to compare pores since the actual pore shape is most certainly not perfectly cylindrical. However, given that the average pore radius is a ratio between the pore volume and the specific surface area, it makes intuitive sense that for a given interaction volume, the size of the scattering center (V in equation [7.2]) is directly proportional to R_p and the number of scattering centers (N) inversely proportional to R_p. Thus the term ($V^2 \cdot N$) in equation [7.2] reduces to a constant times the pore radius R_p. There is more to it than simply the size and number of the pores, however. Pore morphology plays a distinct role in the value of the constant B, as will be discussed in the next section.

7.5.3 Optical Scattering During Sintering

As large pore gels are subjected to different stabilization temperatures, the slope of the turbidity plot remains relatively constant up to the point at which sintering begins. Figure 7.21 shows the Absorbance plotted a function of $1/\lambda^4$ for a gel at several different stabilization temperatures. Minor differences in the slope at temperatures between 180°C and 900°C can be explained by the change in the surface condition due to the dehydration of the gel. The pore structure (pore volume, surface area, and pore radius) remains relatively constant and so does the scattering slope until sintering begins at 1000°C. At this point, the average pore radius begins to decrease but the scattering begins to increase dramatically! The reason for the increase in scattering efficiency for the partially sintered samples is unclear but it is not a function of pore size. The pore size decreases during the

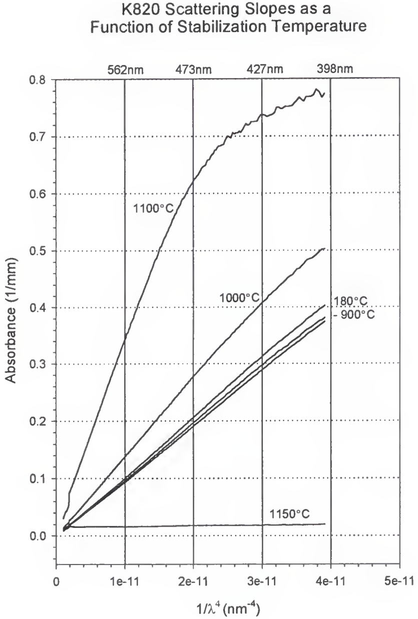

Figure 7.21. Absorbance plotted versus $1/\lambda^4$ for large pore gel stabilized at different temperatures.

sintering process. It must be a result of the changing pore morphology.

Although the pores are getting smaller, the volume elements of interconnected solid glass are growing larger. It is likely that these scattering centers eventually exceed the $\lambda/4\pi$ size limit for Rayleigh scattering and the more general Mie theory must be applied. Thus equation [7.3] is no longer valid.

7.6 Fully Dense Large Pore Gels

Fully dense gels cease to scatter light and become transparent in the visible region. Large pore gels densify into clear monolithic pieces in the vicinity of 1200°C with little tendency to bloat. They still retain some water however, as evidenced by the UV-Visible-NIR spectra in Figure 7.22. Here the dense large pore gel is compared with a commercial low-water silica gel based dense glass produced by Geltech Inc., of Orlando, Florida. The characteristic water absorption peak at 2750nm is still clearly visible in the large pore gel. Even with the low surface area, high permeability and high pore closure temperatures, the large pore gels still retain a significant amount of water when sintered in ambient conditions. The Gelsil™ glass is produced using a chlorine dehydration treatment in a water free sintering atmosphere which improves the optical transmission in both the near infra-red and the ultraviolet.

7.7 Conclusions

The monolithic gels produced by the large pore system extend the pore size that can be achieved in a one step acid catalyzed process. The gels have pore radii on the order of 200Å, with a corresponding increased permeability but at the sacrifice of surface area. They are not mechanically strong when compared to bulk glasses but have adequate strength for most anticipated uses. The low strength enables the dried gels to be easily machined into the desired shape prior to sintering. The optical properties are dominated

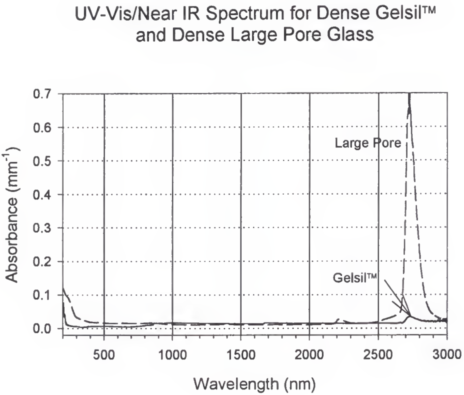

Figure 7.22. UV-Visible/NIR absorption spectrum of fully densified large pore gel compared to that of dense Gelsil™, a commercial low-water optical glass fabricated using a chloride based dehydration treatment.

by Rayleigh scattering and begin to deteriorate in visible region at pore radii above 100Å. However, if used in an aqueous environment, the increased refractive index of the solvent eliminates most of the scattering and provides good transparency throughout the visible portion of the spectrum. (Figure 7.23) The gels have good potential for use as catalyst supports due to the large pore size, higher permeability, large surface area, and chemical stability. These characteristics plus good optical transparency (especially in solution) make these gels attractive candidates for optical sensor substrates. The production of high quality net-shape or machined dense silica glass is also a potential application.

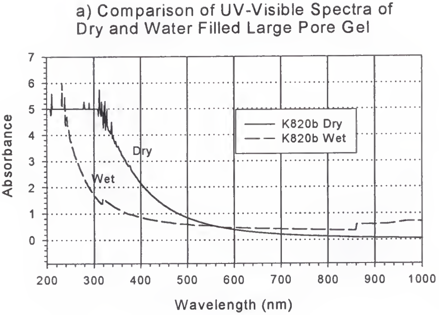

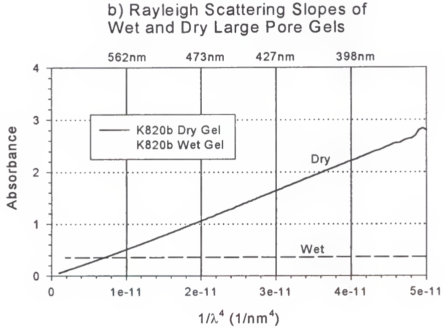

Figure 7.23. Comparison of UV-Vis spectra (a), and scattering curves (b), for a dry large pore gel (n_{air}=1.00) the same gel filled with deionized water (n_w=1.33).

CHAPTER 8

METAL COLLOIDS IN SOL GEL GLASS

Since the time of the Romans small colloidal metal particles have been incorporated in glass to produce striking colors such as the red of gold and copper "ruby" glasses and the yellow of silver stained glasses. Scientists have been interested in this phenomenon since the mid 19th century when Faraday investigated the stability of gold sols (Bam77). Early in this century, Mie used colloidal metal suspensions in the development of his theory of light scattering (Mie08). Throughout this century colloidal sols and specifically colloidal metals in glasses have been studied primarily to elucidate their optical properties and to further develop Mie's theory of light scattering. Doremus studied the optical characteristics of gold and silver colloidal glasses to determine the effects of particle size and method of preparation (Dor64, Dor65). His calculations used more reliable optical constants than were available to Mie. He reported that below a particle diameter of 85Å the optical adsorption peak near 525nm becomes proportional to the particle size indicating a deviation from the optical properties of the bulk metal (primarily ε_2). He attributes this to the size of the particles becoming much smaller than the mean free path of the electrons.

Today this phenomenon is called quantum confinement and continues to be studied in gold and silver glasses with nanometer size colloids. It has been found that such glasses exhibit high optical non-linearity and thus are attractive candidates for use in optical devices (Ina81, Kad93, Ahm96). Gold colloid particles, for example, can have a large third order nonlinear optical susceptibility ($\chi^{(3)} = 1.2\times10^{-7}$esu) and a near resonance nonlinear response that is on the order of 50 picoseconds. The potential usefulness of colloidal metal glasses has led to an increased interest in controlling the size, shape, number and environment of metal colloids in optical substrates, most notably silicate glasses. The traditional methods of precipitating colloidal metals have been augmented by ion implantation and the sol gel route to produce such materials (Mat93, Fuk94). The latter promises the ability to produce colloidal metals in either thin films or in bulk with a high degree purity and homogeneity of the silica matrix.

8.1 Traditional Gold Ruby Glasses

Traditionally, colloidal metal glasses have been produced by incorporating the desired metal in the batch formula for a given glass. Minor additives usually include a nucleating agent such as cerium oxide and a reducing agent such as tin oxide or selenium. The gold, silver or copper ions dissolved in the melt diffuse to the nucleation sites and are reduced to the base metal causing growth of the colloidal particles. There are many recipes for producing ruby glasses. Most are similar to those employed by Maurer (Mau58) and Doremus for the formation of gold ruby glass (Dor65). The formula used by Doremus is typical and is composed of 71.5% SiO_2, 23% Na_2O, 4%Al_2O_3, and 1% ZnO by weight. CeO_2 (0.02 - 0.1%) is added as a nucleating agent and 0.01 - 0.02% gold is added as a chloride salt. The batch is melted at 1200°C in a platinum crucible. After cooling the glass is irradiated with ultraviolet light to nucleate the growth sites and then treated at 400° to 630°C to nucleate and grow the colloidal gold particles. The latter step is often called "striking the ruby" as it is at this stage that the ruby color develops in the glass. Although it has been well established that the particles grow by the diffusion of gold through the glass, there remains some disagreement as to whether the gold diffuses as ions or as neutral atoms. Stookey presents a compelling case for the former although Doremus and others continue to refer to the diffusion of gold atoms through the melt

(Sto49). Typically the concentration of gold lies in the range of 0.01 - 0.2% by weight. The particle size after striking usually ranges from 1.5nm to 20 nm depending on the gold concentration, the concentration of nucleating agent, and the heat treatment employed to grow the colloidal particles. The growth is diffusion controlled (whether by atoms or ions). This has been has been well established by Rao (Rao96).

8.2 The Mechanism of Colloidal Color

The colors produced in ruby glasses are attributed to the scattering of light by the small metal particles as described by Mie (Mie08). However, the phenomenon encompasses more than the simple light scattering of dielectric materials. Metal colloids display a complex refractive index $n^* = n - jk$ where n and k are the real and imaginary (refractive and absorption) components respectively. The relatively high value of k for metals gives high optical absorption in the visible and hence their high reflectivity. At longer wavelengths both k and n tend to increase linearly with wavelength according to the free electron model of Drude (Hum93). In this model, electrons are considered to be free to oscillate with an interacting electromagnetic field. Due to lattice imperfections there is a damping term which is proportional to frequency. Thus the optical constants for metals can be expected to change in a predictable way at longer wavelengths. As the wavelength gets shorter in the visible and UV regions, absorption bands appear that the Drude model cannot account for. Lorentz postulated that the electrons could be considered bound to their nuclei and like any bound oscillating charge cause the appearance of dipoles. As with any bound oscillator there exists a resonance frequency at which the energy absorption is at its maximum. Since the electrons in the metal are assumed to react together in an electromagnetic field, this resonance is called a plasma (or plasmon) resonance. For most metals there is little spectral variation (dispersion) in the optical constants throughout the visible region and colloidal coloration tends toward neutral shades of brown or gray (e.g. Pd and Pt formulations). Gold, silver and copper, however depart from the norm. All three display a plasmon resonance in the visible region. There is a dramatic shift in the optical constants for the metals that affects both the adsorption and scattering of incident light. This is the source of the red colloidal coloration of gold and copper, and the yellow coloration of silver. It is this same phenomenon that is responsible for the gold and copper coloration of the bulk metals. The deviation for silver lies in the near ultraviolet and hence is not as visible in the bulk metal, however in silver colloid glasses the adsorption peak lies in the vicinity of 400nm with a tail that extends into the blue. Figure 8.1 shows the optical constants for gold as a function of frequency. In the vicinity of 525nm there is a rapid decrease in n and a concurrent increase in k. This is the gold plasmon band.

Doremus studied a gold doped ruby glass glasses and applied the scattering theory of Mie to more fully describe the mechanism of the absorption which gives rise to the color (Dor64, Dor65).

8.3 Scattering and Adsorption

Although Mie's classic paper regarding colloidal gold particles dealt primarily with scattering phenomena, it is a combination of scattering and absorption of the colloidal particles that is responsible for the color of these glasses. If one assumes spherical colloids, and a low concentration of scattering centers (independent scattering events), the scattering and absorption efficiency contributions to the total turbidity can be calculated by equations [8.1] and [8.2] (Bam77).

$$Q_{\text{scat}} = \mathrm{Re}\left[\frac{8}{3}\cdot(x)^4\cdot\left[\left|\frac{m^2-1}{m^2+2}\right|\right]^2\right] \qquad [8.1]$$

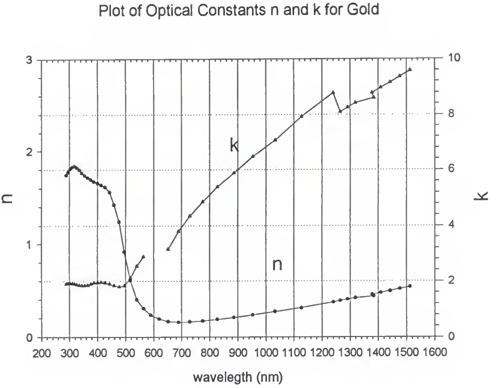

Figure 8.1. Optical Constants for Gold (Pal80).

$$Q_{abs} = -\operatorname{Im}\left[4\cdot x\cdot\left[\frac{m^2-1}{m^2+2}\right]+4\cdot\frac{x^3}{15}\cdot\left[\left|\frac{m^2-1}{m^2+2}\right|\right]^2\cdot\frac{m^4+27m^2+38}{2m^2+3}\right] \qquad [8.2]$$

where

$$x=\frac{2\cdot\pi\cdot a\cdot n_s}{\lambda} \qquad \text{and} \qquad m=\frac{N-iK}{n_s}$$

a = particle size in nm

λ= wavelength of incident light

N = real part of the refractive index

K = imaginary part of refractive index

n_s = refractive index of the matrix (in this case silica)

At particle sizes less than 10nm, the scattering contribution is negligible and the ruby color is generated by a combination of the absorption at 525nm and the higher absorption in the blue. Figure 8.2(a) shows the theoretical absorption and scattering efficiencies using the best available optical constants for gold (Pal80). In Figure 8.2(b) the same functions are plotted for a 40nm colloid size. Note that the scattering contribution which is minimal at 10 nm, increases dramatically as the particle size increases. The total diminuation of transmitted light, represented by the total efficiency factor Q_{total}, is the sum of the scattering and absorption contributions. Figure 8.3 shows the total attenuation of transmitted light as a function of gold colloid size.

As particle size increases, intuition might tempt one to expect the scattering component to eliminate more of the blue due to Rayleigh-Gans type scattering. However, the dispersion of gold is such that its index is relatively close to that of the glass matrix in the blue region and this minimizes the scattering in this area. By the same token, the variation (rapid decrease) in the real part of the refractive index in the vicinity of 530 nm

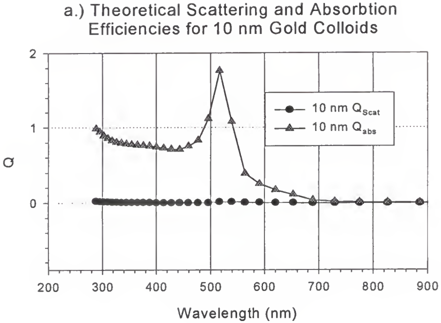

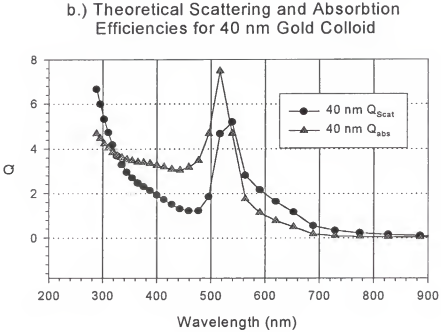

Figure 8.2. a.) Theoretical absorption and scattering efficiencies as a function of wavelength for 10 nm gold colloids in silica. b.) Same as (a) but calculated for 40 nm particles.

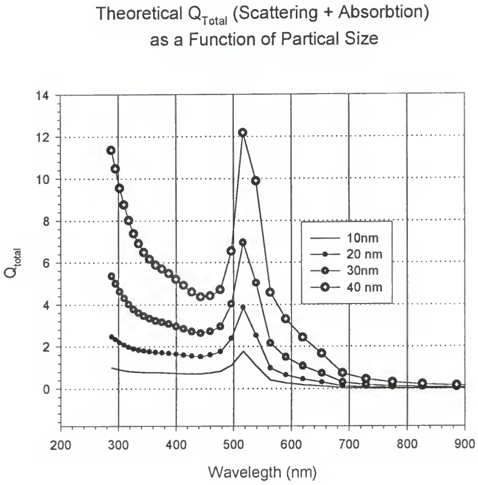

Figure 8.3. Total attenuation factors for transmitted light for several different particle sizes.

causes much greater scattering near the plasmon band. Finally, the tails of both the scattering peak and the absorption peak are large and extend into the red region of the visible spectrum. Consequently, as particle size grows both the scattering and absorption components combine and grow larger in the red than the blue. The combination of these effects produces the characteristic absorption/scattering spectrum we see. Thus as the colloidal gold particles increase in size either by aggregation or by growth (e.g. "overstriking" of a ruby glass), the result is a progressive change in color from red to violet to blue. If the particles grow large enough to behave as bulk metal (i.e. the particle size becomes much larger than the penetration depth ≈ 15nm for gold), reflection also begins to play a role and the glass takes on a muddy color.

In summary, as a gold sol is formed from very small spherical particles it develops a ruby red color due primarily to absorption in the blue and green, as the particles grow the color develops to a wine red as scattering and absorption tails grow into the red part of the spectrum. Larger particles or aggregates cause a rapid increase in scattering in the red allowing only blue light through. These gels appear blue in transmission and reddish or violet when viewed from the side. As particles become very large, the solution takes on a reddish brown or "muddy" look as reflection begins to contribute.

8.4 Scattering in Sol Gel Derived Porous Glasses

For most dense glasses there is very little scattering internal to the glass itself due to the fine scale of homogeneity in the glass. For porous sol gel glasses, however, there is inhomogeneity due to the empty pores ($n=1.0$ for air in pores and $n \approx 1.46$ for silica glass).

The scattering of pure silica gels of various pore sizes was discussed in the last chapter and for most mesoporous gels is dominated by Rayleigh scattering. The scattering is greatest in the ultraviolet and blue and there is significant loss in the visible spectrum as the pore size increases. In the last chapter, Figure 7.18 showed the total absorbance of a

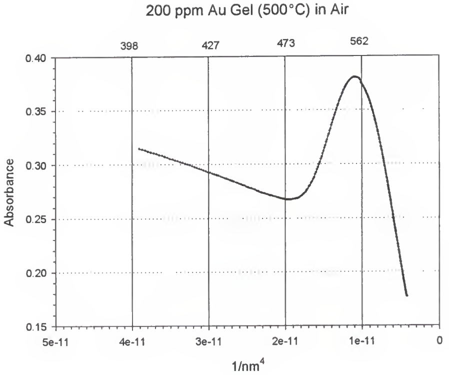

Figure 8.4. Plotting the absorbance vs. $1/\lambda^4$ clearly shows the contribution of the plasmon band versus the matrix scattering contribution.

200Å silica gel monolith plotted against $1/\lambda^4$. The resulting straight line was indicative of Rayleigh scattering. Figure 8.4 shows a gold ruby glass plotted in the same manner. It is clear that there is an additional source of absorption (or nonlinear scattering) that is responsible for the ruby red color of the colloidal gold glass. Thus when analyzing the optical properties of gold colloids in porous glasses, both the Rayleigh scattering of the glass and the scattering from the colloidal particles must be considered. In dense ruby glasses, there are no pores and the scattering contribution of the glass becomes negligible.

8.5 Quantum Size Effects

For very small particles or clusters of metal atoms the underlying assumption of band structures is no longer valid. As the number of atoms in the cluster becomes very small, the allowed electronic transitions again become discrete in accordance with the Pauli exclusion principle. The concept of a plasma of free electrons which respond in unison to electromagnetic radiation must give way to individual (or small cooperative groups) of electrons undergoing transitions between individual electronic levels. The exact manner in which individual or small cluster excitations give way to plasma oscillations in larger particles is still a matter of much speculation in solid state physics (Bra97). There are two ways to approach the interaction of light with very small metal clusters: quantum mechanical methods focusing on ab-initio or semi-empirical molecular orbital calculations, or quantum box models (jellium models) borrowed from solid state quantum theory (Bam77).

The quantum mechanical approach relies on the calculation of the electronic ground states and the excited states for the entire cluster. This involves calculating all the electron wavefunctions for the entire cluster. Coulombic interactions between electrons and nuclei and quantum mechanical (exchange) interactions must all be incorporated to arrive at an ab-initio solution. Even after ground states are computed, configuration interactions must be carried out for each applicable excited state. In very small clusters such optical transitions can change the stable geometric structures requiring additional computations. Even today with fast supercomputers, the complexity and computational demands rule out ab-initio calculations for all but the smallest clusters. Semi-empirical methods significantly reduce the computational complexity of the problem by making approximations to reduce the degrees of freedom in the cluster. The complex many body problem is reduced to an independent single electron system by replacing particle-particle interactions with properly defined effective potentials. Thus the nucleus and inner shell electrons are replaced with a core potential which is used to define the eigenvalue problem for the bonding (or conduction) electrons. The wave functions for conduction electrons are defined in terms of linear combinations of atomic orbital (LCAO) wavefunctions which are well characterized. The effective core potential operators are derived by comparing theoretical results for known compounds with measurable properties such as ionization potentials, polarizabilitites and optical excitation energies. These comparisons lead to adjustments in the theoretical parameters, hence the name "semi-empirical". The use of semi-empirical methods reduces the computer power necessary for complex calculations and allows calculations to be performed for larger clusters (e.g. in the 50 -60 atom range). However, the transition from cluster to bulk behavior most certainly occurs at much larger cluster sizes than this. In order to model the behavior of larger clusters, containing hundreds to thousands of atoms, physicists have invoked the jellium model.

The jellium approach views small metal clusters as a smooth "jelly" of positive charge (rather than a periodic lattice potential) to which the valence electrons are attracted. This model is justified by the assumption of a high density of delocalized electrons screened from the core potential which is represented by the positive jelly. This makes it possible to use a one electron model and an effective core potential determined by the size and configuration of the cluster. Thus it is possible to view the cluster as one "giant atom" with the electrons assigned "cluster" quantum numbers. Electronic states are filled governed by the Pauli exclusion principle. Certain cluster sizes (numbers of atoms) display closed electronic shells and give rise to electronic magic numbers. These magic numbers are believed to be related to the tendency for metal to preferentially form in certain size clusters. These particularly stable clusters often have specific shapes and internal structures that differ from the corresponding bulk metal giving them unique properties (Bra97, Kre95).

8.6 Variation of Electronic Spectrum with Cluster Size

The description of the absorption/scattering effects of metal colloids as described by Mie theory depends on electrodynamic effects between the particles and the impinging electromagnetic field. The calculations are dependent on the size of the particles and the wavelength dependent optical constants $\varepsilon_{1,2}(\nu)$ which are ordinarily derived from measurements on the bulk material. As the cluster size decreases toward molecular dimensions the dielectric properties of the material become size dependent $\varepsilon_{1,2}(\nu,r)$. Size dependencies can be due to a variety of reasons including changes in atomic structure, influence of the cluster surface, and shape factors (symmetry). For example, the atomic distance in Au_2 is 2.53Å as opposed to 3.25Å in the bulk metal (Rua59). The primary size effect is manifested as a narrowing of the dipole resonance which by Mie theory is expected to follow a (1/r) relationship. This 1/r law discovered by Mie turns out to be a quantum size effect in which the conduction band in the metal breaks up into discrete states as the dimensions become small enough. This is as can be expected and in the limit e.g. for trimers, dimers and single atoms, sharp and distinct spectral lines can be observed (Che81). There is also a change in the plasma resonance as cluster size decreases. For example there is a blue shift and band narrowing for Ag clusters as particle sizes approach 10 nm (Dor65). A similar effect takes place in gold and other metal clusters. The 10nm cluster radius can be used as a general "rule of thumb" as the point where cluster properties are best described by classical rather than quantum mechanical treatment.

8.7 Nonlinear Effects

The growing field of fiber optics and interest in electro-optical device technologies over the past two decades has spurred a dramatic increase in the study of nonlinear optical properties of materials. Small metal clusters display strong nonlinearity under certain conditions and optical properties that vary according to colloid size. Nonlinear optical effects are governed by the higher order contributions to the electric polarization vector $P(\omega)_i$ which can be described by

$$P_{NL}(\omega)_i = \sum_{i,j} \chi_{ijl}^{(2)} E_j^{\omega_1} E_l^{\omega_2} + \sum_{i,j} \chi_{ijml}^{(3)} E_j^{\omega_1} E_l^{\omega_2} E_m^{\omega_3} + \qquad [8.3]$$

$\chi_{ijl}^{(2)}$ and $\chi_{ijml}^{(3)}$ are the second and third order nonlinear susceptibilities that are responsible for a variety of nonlinear effects. Second Harmonic Generation (SHG) or sum and difference frequency mixing is governed by $\chi_{ijl}^{(2)}$, while $\chi_{ijml}^{(3)}$ corresponds to processes such as third order harmonics, degenerate four wave mixing, and the optical Kerr effect. SHG can be understood by assuming a scalar equation with an incident wave $E=E_0 (\sin\omega t)$. This creates a second order polarization proportional to $\chi^{(2)}E^2$. Using the relation $\sin^2(\omega t) = 0.5\,[1-\cos(2\omega t)]$ it becomes clear that the nonlinear polarization oscillates at a frequency of 2ω. Symmetry selection rules reduce the number of nonzero terms in the polarization tensor. In particular $\chi^{(2)} = 0$ for centrosymmetric systems. $\chi^{(3)}$ however, is nonzero for this symmetry.

The strong polarizability of small metal clusters at the surface plasma frequency can result in a dramatic increase in the nonlinear properties. If the particles are spherical, they automatically have inversion symmetry and hence could be expected to have no SHG.

However, this is only true if the field is homogeneous across the entire particle. As particles get larger (e.g. sizes comparable with λ), retardation leads to phase changes in the electric field across the cluster which can lead to emission of the second harmonic. For very small spherical clusters there is no second harmonic. This facilitates the study of third order effects.

Gold clusters are a good candidate for the study of non linear properties. Whereas quantum confinement in semiconductor clusters is responsible for their non linear properties, in metals it is the local field enhancement brought about by the excitation of the surface plasmon. Photodarkening occurs in semiconductor clusters under high intensity irradiation. No such effect is reported for gold colloid doped glass (melt derived) which has a third order susceptibility on the order of 2.5×10^{-11} e.s.u. The response time of the gold clusters is also much faster having been measured by degenerate four wave mixing (DFWM) at 5 picoseconds (Kad93, Ahm96). The stability of gold's nonlinear properties under laser irradiation make it a candidate for incorporation into nonlinear devices. In thin sol gel films, and ion implanted films, third order susceptibilities ($\chi^{(3)}$) as high as 1.2×10^{-7} e.s.u. have been measured (Mat93, Fuk94).

8.8 Metal Colloids in Sol Gel Derived Glasses

The preparation of small metal clusters in sol gel derived silica has received scant attention, perhaps due to the difficulty in drying (and/or densifying) samples large enough to analyze or in producing stable thin films. Clusters in porous samples are a necessary precursor to dense samples but may have applications of their own, particularly in the area of metal catalysts.

In this work, small gold and silver colloids are produced in monolithic porous glass with a variety of pore sizes. The difficulties of drying and densifying monoliths can be overcome by the proper formulation and careful control over the drying and densification conditions. Gold, silver and several other metals can be easily introduced into the silica gel by adding the desired amount to the gel formulation in the form of a metal salt (usually chloride for gold and nitrates for other metals) and then allowing the solution to gel. The salt remains in the pore liquor and is deposited on the interior surfaces of the pores as the liquid is evaporated during drying. Colliodal metal particles are produced by the decomposition of the salt during subsequent heat treatments or the reduction of the salt in a reducing atmosphere. In the case of gold, particles are sometimes formed by autocatalysis or disproportionation of the salt if the solution conditions are insufficiently oxidative. This is undesirable as the colloids tend to be large and inhomogeneous. Metal salts can also be post-doped into porous glass if the glass is stable enough towards rehydration. This is generally more applicable for larger pore systems.

Small sol gel monoliths can be produced with pore radii ranging from less than 10Å to greater than 400Å. In these investigations, three (nominal) pore radii were selected, 10Å, 30 Å and 200Å. It is postulated that the pore size will constrain the growth of the colloids producing different sizes of metal clusters suitable for analysis.

8.8.1 10 Å Pores -- Hot Nitric Acid Formula

Dried sol gel monoliths with 10Å pore radii are produced by using a low R-ratio (R= mole ratio of water to TMOS) in a heated bath under highly acidic conditions. The high temperature and acidic conditions insure rapid hydrolysis of the TMOS and promote the evaporation of methanol formed by the reaction. The elimination of the methanol is an important feature of this scheme for several reasons. Highly acidic sols promote reesterification of silicic acid back to the methoxy precursor. Reduction of methanol should shift the reaction towards more complete hydrolysis by LeChatelier's principle. Reduction of methanol also produces a higher dielectric solvent (closer to water). This should enhance the charge stabilization of the condensed species. Finally, the removal of methanol reduces the overall volume of the gel producing a higher initial gel density (increased solids loading). The higher gel density correlates to smaller pore size which increases capillary pressure (and hence syneresis) during drying. At the same time, it imparts greater strength to the wet gel helping it survive the drying process. The ultimate result is a microporous gel with an average pore radius of 1 nanometer. Figure 8.5 shows the BET data for a typical, as dried, gold doped microporous gel. The average pore radius is 10.88Å but the pore size distribution and micropore analysis (not shown) indicates substantial porosity below 10Å. When considering pore sizes in microporous gels, the admonitions of chapter three should be remembered. Pore radius is usually understated by a significant margin in microporous gels. Although the figures above can be used for comparative purposes, they should not be taken too literally.

8.8.2 30 Å Formula

Gels with an average pore radius of 30Å are prepared at room temperature by using an R ratio of 16:1 under acidic conditions (pH=2). A small quantity of HF (.001 moles HF:1 mole TMOS) is added as a catalyst. Figure 8.6 shows the BET isotherm and desorption pore size distribution data for these gels. The isotherm shows the typical Type E hysteresis loop of mesoporous silica gels indicating ink-bottle type pores.

8.8.3 200Å Formula

The formula used to produce a 200Å radius gel uses an R ratio of 16:1, acidic conditions (pH=2) and is also catalyzed with HF. For the larger pore gel a higher concentration of HF is required (.006 moles HF: 1 mole TMOS). This is the “standard” formula gel studied in Chapters 5-7. In order to slow down the reaction, the sol is diluted with an equal volume of methanol and cooled to 5°C before the addition of

Desorption Isotherm for 200ppm Au HNA

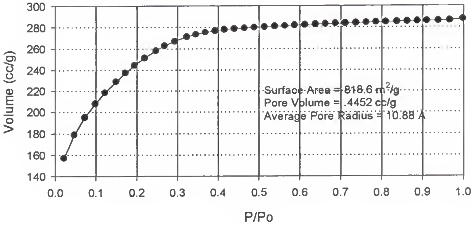

Desorption Pore Size Distribution for Au 200ppm HNA Formula

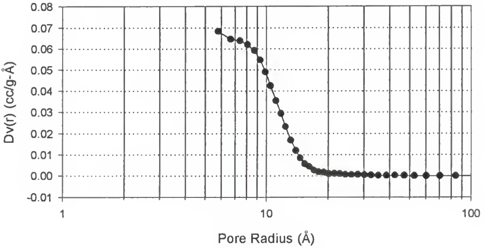

Figure 8.5. Desorption isotherm and pore size distribution for microporous (10Å) 200 ppm gold gel.

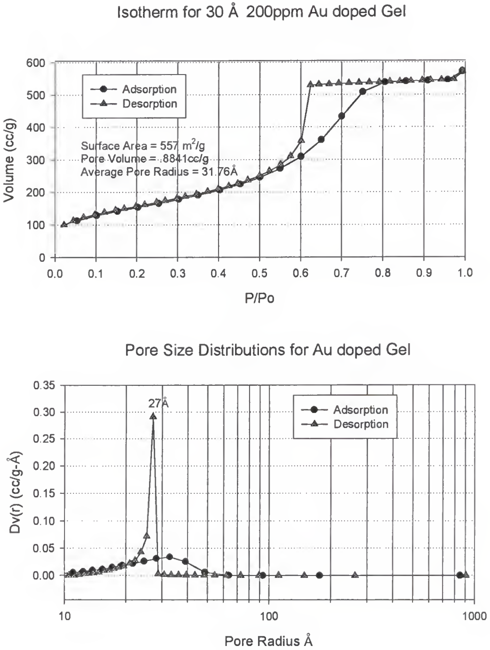

Isotherm for 30 Å 200ppm Au doped Gel

Surface Area = 557 m^2/g
Pore Volume = .8841cc/g
Average Pore Radius = 31.76Å

Pore Size Distributions for Au doped Gel

27Å

Figure 8.6. Isotherm and pore distribution for 30Å Au doped gel.

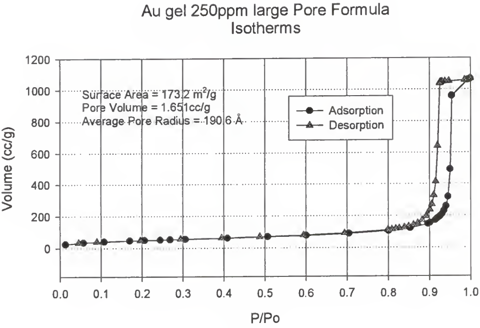

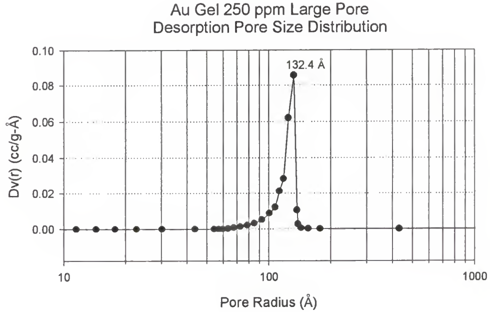

Figure 8.7. Isotherm and pore distribution for large pore (200 Å) silica gel monolith doped with 250ppm Au.

the TMOS. Figure 8.7 shows the BET analysis of the large pore gel doped with 250 ppm Au.

8.8.4 Doping and Heat Treatment

All of the gels in this experiment were pre-doped. The gold was added to the sol prior to gelation in the form of an ICP standard composed of AuCl in 2% nitric acid. The concentration of gold in the standard solution was 1000μg/ml. The final concentration of gold in ppm was calculated with reference to the dry weight of the stoichiometric silica in solution. (e.g. 100ppm Au indicates 100 parts Au per million parts silica by weight.

The gels were all aged and dried identically with a final drying temperature of 180°C. Some of the gels showed a slight coloration after drying indicating some formation of gold particles had already begun. Full formation of the colloids was complete after heat treating at 400°C. UV-Vis spectra were taken at this temperature, at 800°C and after achieving full density for the two larger pore sizes (1050°C for the 30Å gel and 1200°C for the 200Å). The microporous gel could not be brought to full density due to the evolution of water at high temperatures (bloating).

8.9 Results and Discussion

The results were determined by UV-Vis spectra taken on the gels after treatment at 400°C, 800°C, and fully dense glass. A peak at the plasmon frequency of ≈530nm is indicative of well dispersed particles and a spherical morphology. The presence of a broad plasmon band in the vicinity of 600 nm is indicative of large irregularly shaped particles or large aggregates. Figures 8.8 and 8.9 show the UV-Vis results for the three types of porous glass at several different annealing temperatures. The 10Å gels all appeared blue in transmission with clearly visible scattering of red when viewed from the side. Figure

a.) UV-Vis Spectra for 200 ppm
Au doped microporous (HNA) Gels

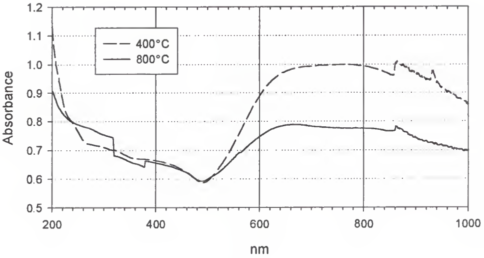

b.) UV-Vis Au 200ppm 30 Å Formula
With Different Heat Treatments

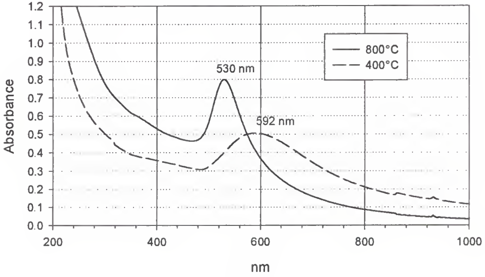

Figure 8.8. UV- Visible absorption spectra for 10Å and 30Å Au doped gels (200ppm). a.) UV- Visible absorption spectra for 10Å gel doped at 200ppm. b.) UV- Vis absorption spectra for 30Å Au doped gel (200ppm).

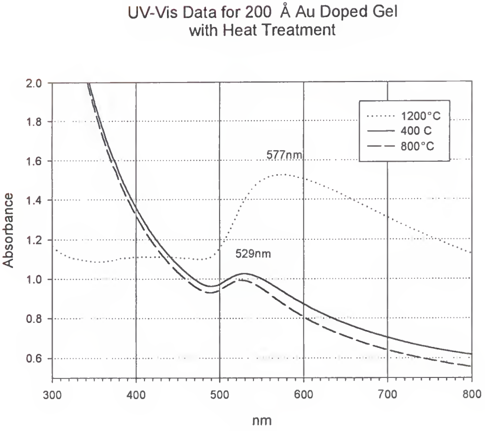

Figure 8.9. UV-Visible absorption spectrum for 200Å Au doped gels for three different stabilization temperatures (250ppm).

8.8(a) confirms this with a very broad band in the red which extends into the near infrared. This is most likely a product of aggregation as the particle size of the gels should be limited by the pore size of the glass. Linear or fractal aggregates can form along the pore network even with small pore sizes and give rise to the broad red shifted band (Che81). The 30Å glass (Figure 8.7(b)) also appeared bluish after treatment at 400°C indicating either large irregularly shaped particles or aggregates. After treatment at 800°C, however, the plasmon band shifted back to 530nm and narrowed. This same effect was reported by Doremus (Dor65) upon heat treatment of his "purple" sols and can be attributed to the particles becoming more spherical or the sintering of aggregates. Oddly, the 200Å gels showed the opposite effect upon densification at 1200°C. Whereas they started out with a plasmon peak at 529nm the peak red shifts and broadens as the gel becomes dense. This may be a function of the large degree of shrinkage in these gels (≈400% by volume, ≈40% linearly) during densification. Thus the gold clusters are brought into greater proximity and may form aggregates.

8.10 Conclusions

The doping of metal clusters into sol gel derived silica is an interesting and potentially fruitful area for research. The technique paves the way for the production of low expansion heat resistant optical composites that take advantage of the optical properties of small metal clusters. If the goal is the production of dense silica glass with well dispersed and spherical clusters, the 30Å or 200Å gel formulas are promising. For catalytic purposes the gels can be doped with platinum or palladium and kept in the porous state. (Other metals can be used if they are amenable to reduction by heat treatment in reducing atmospheres.) Porous gels can be made with a wide variety of pore volumes and surface areas and thus can be tailored to the specific need. Permeability plays a major role in catalytic applications and thus the larger pore sizes might be of particular interest.

There are still many questions to be answered about the formation and behavior of gold and other metallic clusters in sol gel derived porous glass. The size and morphology of the clusters needs to be established by TEM and compared with the porosity and spectroscopy data. The doping parameters need to fully explored in order to control the size and distribution of the metal clusters. Gold is just one of many metals (and semiconductors) that are amenable to cluster formation in sol gel glasses. Many other applications are waiting to be explored.

CHAPTER 9

CONCLUSIONS AND RECOMMENDATIONS

With the proper techniques, sol gel derived glasses can be fabricated with virtually any combination of surface area and pore volume. Prior to these investigations the program here at the University of Florida had developed and characterized a system for producing gel monoliths with pore radii ranging from 12 to 90Å. The work described here has extended that range to over 400Å although for practical reasons the 200Å system has been emphasized. Although not a direct goal, microporous gels based on a hot nitric acid sol have been produced with pore radii on the order of 10Å. These were analyzed in Chapter 3 and used for producing gold colloids in Chapter 8. This extends the total range of gel monolith technology to pore radii of 10Å to 400Å, a range that extends from the microporous to the macroporous. With the proper combination of formulation, aging treatment(s) and drying techniques, porous glass monoliths can now be tailor-made to any pore size within this range.

Problems remain, however. The production of monoliths using conventional drying techniques is still an art and even small adjustments to the formulation, aging or drying process can cause large changes in pore size. For example, in Chapter 6 decreasing the size of a "standard" monolith, and drying at 60° instead of 103°, cuts the pore size in half. This is because the monolith size, aging time, drying temperature and pore size are all interrelated. Smaller size monoliths dry faster (there is a larger surface area to volume ratio) therefore undergo less aging. The reduction in the pore size increases the capillary pressure and the driving force for shrinkage of the gel. Increased shrinkage reduces pore size even more but extends the drying time due to lower permeability. In short, *the* *drying time affects the pore size and the pore size affects the drying time.* This is particularly noticeable for larger pore sizes where the network is more compliant. Likewise, the drying temperature has a profound effect on the ultimate pore size. High drying temperatures speed drying and reduce the amount of time the gel is aged but the aging occurs faster at the higher temperature. Consequently, a certain amount of "fine tuning" is required whenever a new pore size is contemplated.

9.1 Nitrogen Adsorption Analysis

Analysis of porosity and texture by nitrogen adsorption is more complex than many believe. One of the reasons is the basic assumption in BET theory that the pores are cylindrical. This is the basis for the pore sizes calculated by equation [3.11] using the surface area and pore volume. This is acceptable for comparison purposes especially for porous materials with similar morphologies such as the gels analyzed in this study. However, analysis of the pore texture and shape is more complex. If one assumes a colloidal structure for gels as is indicated by the AFM and SEM images of Chapter 7, then it is probable that both small and large pore gels have pore shapes that are similar in shape but different in scale. The smaller pore sizes have hysteresis loops that indicate ink-bottle shaped pores while the isotherms of the larger pores invariably tend towards cylindrical.

The actual shape of the pores in both is similar, governed by the size of the colloidal particles on the pore walls and the fractal nature of the gel. But as pointed out in Chapter 3 the change in scale results in a "cylindrical" adsorption mechanism for the larger pore sizes leading to very steep isotherms. Small pore sizes adsorb nitrogen through a combination of the "cylindrical" and "meniscus" mechanisms leading to a broader hysteresis loop which is characteristic (by DeBoer's classification) of ink bottle shaped pores.

In practicality the precise shape of the pores is less important than the surface area of the gel, the total pore volume, and the minimum pore entry or "neck" size. Surface area is important in the use of gels for catalyst supports or when it is used to immobilize desired analyzates. The total pore volume and neck size are important in governing the permeability of the network and in trapping desired species within the network. The overall combination governs the optical transparency of the gel which is important for use in optical applications. Surface area and pore volume are measured quite accurately by nitrogen adsorption and the pore neck size can be estimated by the peak in the desorption pore size distribution. Even with a less than perfect understanding of pore morphology, nitrogen adsorption is a powerful technique for characterizing porous matrices.

9.2 Fluoride Catalysis

Perhaps the most interesting results of these investigations are the insights gleaned from the study of fluoride catalysis in Chapter4. The concentration of free fluoride and the pH was measured for HF catalyzed gels as they were titrated with TMOS. The complexation ratio and decrease in pH provide evidence that there is a negatively charged multifluorinated silicon species that forms in the HF catalyzed sol. Further measurements suggest that this species resides on the surface of the growing colloids and catalyzes the condensation of excess silicic acid. Consistent with these findings, theoretical studies also implicate a stable pentacoordinate species as the most likely candidate.

Apart from the purely theoretical findings, these results have practical applications as well. For example, the feasibility of fluoride catalysis of multicomponent bioactive sol gels has been questioned due to very low solubility limit of CaF_2 . If, however, the silica source is added first, the bulk of the fluoride combines with the silica to form multifluorinated species and the soluble calcium salt can then be added to the sol without precipitation of CaF_2. This has been demonstrated in the laboratory. The condensation reaction is still fluoride catalyzed and there is a 50% increase in pore volume and average pore radius. The same procedure may be useful in the catalysis of sols containing other components that have an affinity for fluoride such as some transition metal salts (e.g. erbium).

Implications of the HF catalysis findings may extend beyond the HF catalysis of acidic sols. Remember that the fluoride and hydroxide ions are very similar in size and electronegativity. If the pentacoordinate species proposed is correct, it is likely that the condensation reaction throughout the spectrum of pH conditions shares a similar mechanism. The difference in the rates and reaction characteristics may simply be a function of the differences between the size and electronegativity of the two ions and the equilibrium conditions governing their concentrations.

Like the fluoride catalyzed gels, OH^- catalyzed condensation also relies on a hypercoordinated silica species. The difference is that in water, OH^- is ubiquitous; its availability governed only by pH. The concentration of OH^- as a function of pH varies from 1.0×10^{-14} molar at a pH of 0 to 1.0 molar at pH 14. The difference between HF and OH^- however is that whereas the pentacoordinate F^- species SiF_4OH^- is limited by the amount of HF added to the mix, the concentration of the analogous pentacoordinate species $Si(OH)_5^-$ is limited only by pH and the kinetics of the competing condensation and dissolution reactions.

9.3 Large Pore Gel Monoliths

Chapters 5, 6 and 7 document the fabrication and characterization of large mesoporous gel monoliths having a nominal pore radius of 200Å. These gels are based on the HF catalysis of TMOS under acidic conditions. It was found that the system is well behaved and produces good quality gel monoliths with several attractive properties making them good candidates for chemical or optical sensor substrates. These properties include:

1. Large surface area - 150m^2/g.
2. Large Pore Volume - 1.60 cc/g.
3. Large Average Pore radius - 200 Å.
4. High permeability.
5. Good optical transmission.
6. Environmental stability.
7. Chemical stability.
8. Stability towards rehydration.
9. Machinable in dry state.
10. Good sintering characteristics.

The large surface area is advantageous in applications requiring surface mediated reactions or surface modification. These include catalyst supports or chemical sensors where the surface is modified with an analyzate. The large pore volume and large pore radius combine to increase the permeability of the gel providing access to reactants and/or analytes. The large pore size also increases the accessibility of the gel to large molecules or second phases that can be restricted by smaller openings.

Since the composition of the undoped gels is pure silica, it has good chemical stability under a wide range of conditions. Unlike gel monoliths with smaller pore sizes, large pore gels can be stored in ambient conditions for long periods without degradation or cracking. Likewise, there is little tendency to absorb atmospheric contaminants.

For optical applications, the gels can be used either as porous optical composites or sintered to full density. Nanoscale second phases are incorporated by doping either during formulation or after processing. With care, the gels can be rehydrated and redried to accommodate dopants that are sensitive to the harsh conditions necessary during processing. Although the porous substrates display a high degree of optical scattering when dry, they become quite transparent in the visible when filled with water. Dense optical composites have the advantage of containing only the desired dopant and silica, capitalizing on the desirable properties of high silica glass.

Dried gels can be easily machined to desired shapes before densification with little tendency to fracture. Thus optical components can be cast to the desired shape, machined, or a combination of both. Although there is still some water retained when sintered in ambient conditions, there is little tendency toward bloating. Dehydroxylation treatments can be applied if low water components are required.

Although the research conducted here focused on a pore size of 200Å, gels with pore radii as large as 400Å have been fabricated. They are similar in most characteristics, however the optical transparency deteriorates rapidly as pore size increases above 200Å.

9.4 Nanocomposites Made With Sol Gel Glass

A variety of inorganic second phases have been doped into porous silica gels. Due to its unique optical properties, colloidal gold was used to produce both porous and dense silica nanocomposites. Gels of several different pore sizes were predoped with gold chloride and heat treated to produce gold colloids in a silica matrix. The resulting composites were heat treated at various temperatures and examined. It was found that the optical properties of porous composites differed considerably according to pore size. Full density ruby glass can be made under ambient conditions only with the larger pore silica gels. Smaller pore sizes are subject to bloating when sintered but might be brought to full density if suitable dehydroxylation treatments were employed.

9.5 Recommendations for Future Work.

There are several findings in these investigations that suggest areas for future research. Fluoride catalysis should be examined in greater depth at a variety of different pHs. The fluoride electrode can be used up to a pH of 5 or 6 before the hydroxide concentration begins to interfere with its operation. It might be possible to confirm the catalysis mechanism suggested in Chapter 4 through ^{29}Si NMR of HF catalyzed sols.

There is no reason to believe that 400Å is the maximum size of pores that can be produced using sol gel methods. With the use of various aging strategies and supercritical drying techniques, gels can be fabricated with even larger pore sizes. Composites with degradable second phases should be investigated as avenues for the introduction of large macropores. The combination of large macropores for greater permeability and small pores with large surface areas might have numerous applications in the field of catalysis and chemical synthesis.

Finally, there is great potential for producing nanocomposites of silica and a variety of second phases. It may be possible to tailor the size of the second phase on a nanometer scale by controlling the pore size of the host silica gel. Inorganic phases that can survive sintering temperatures can be consolidated in the silica matrix to produce novel optical or electronic properties.

9.6 Closing

Despite the massive amount of research that has been conducted over the last few decades, sol gel science still has many fruitful areas and potential applications. The use of sol gel technology for the production of high purity silica products is still in need of development. The use of porous substrates in optical sensors and as a route to novel optical materials is in its infancy. The work accomplished here has extended the pore sizes that can be routinely fabricated and demonstrates that with a concerted effort virtually any pore size surface area combination is within reach.

LIST OF REFERENCES

Ael50a Aelion, R., Loebel, A., and Eirich, F., Journal of the American Chemical Society, 72 (1950), 124.

Ael50b Aelion, R., Loebel, A., and Eirich, F., Journal of the American Chemical Society, 72 (1950), 5705.

Ahm96 Ahmadi, T. S., Logunov, S. L., and El-Sayed, M. A., Journal of Physical Chemistry 100 (1996), 8053-8056.

Ale67 Alexander, G. B., Silica and Me; the Career of an Industrial Chemist, Doubleday, Garden City, N.J. (1967).

Ale54 Alexander, G. B., Heston, W.M., and Turner, R.K., Journal of Physical Chemistry, 58 (1954), 153.

Ara95 Araujo, F.G., Latorre, G.P. and Hench, L.L., Journal of Non-Crystalline Solids, 185 (1995), 41-48.

Bae76 Baes, C.F. Jr., and Messmer, R.E., The Hydrolysis of Cations, John Wiley and Sons, Inc., New York (1976).

Bam77 Bamford, C. R., Colour Generation and Control in Glass, Elsevier Scientific Publishing Company, New York (1977).

Bar51 Barret, E. P., Joyner, L. G., and Halenda, P. P., Journal of the American Chemical Society, 73 (1951), 373.

Bee45 Beebe, R.A., Beckwith, J.B., and Honig, J.M., Journal of the American Chemical Society, 67 (1945), 1554.

Bel90 Belot, V., Corriu, R., Guerin, C., Henner, B., Leclerq, D., Mutin, H., Vioux, A., and Wang,Q., Mat. Res. Soc. Symp. Proc. Vol 180, Materials Research Society, Pittsburgh, PA (1990), 3.

Berg94a Bergna, H. E., in The Colloid Chemistry of Silica, H.E. Bergna, Ed., American Chemical Society, Washington, DC (1994), 147-159.

Berg94b Bergna, H.E., in The Colloid Chemistry of Silica, H.E. Bergna, Ed., American Chemical Society, Washington, DC (1994), 1-45.

Bla82 Blatchford, C.G., Campbell, J.R., and Creighton, J.A., Surface Science, 120 (1982), 435-455.

Bog88 Bogush, G.H., and Zukoski, C.F., in Ultrastructure Processing of Advanced Ceramics, J.D. Mackenzie and D.R. Ulrich Eds., Wiley, New York (1988), 477-486.

Bon80 Bond, A.M. and Hefter, G. T., Critical Survey of Stability Constants and Related Thermodynamic Data of Fluoride Complexes in Aqueous Solution, IUPAC Chemical Data Series, No. 27, Pergamon Press, New York (1980).

Bra97 Brack, M., Scientific American, 227, n6 (1997), 50-55.

Bri86 Brinker, C.J., Roth, E.P., and Tallant, D.R., in Science of Ceramic Chemical Processing, Hench,L.L. and Ulrich, D. R., Eds., Wiley, New York (1986), 37.

Bri88 Brinker, C.J., Kirkpatrick, R.J., Tallant, D.R., Bunker, B.C., and Markey, B.J., Journal of Non-Crystalline Science, 99 (1988), 418.

Bri90 Brinker, C.J., and. Scherer, G.W., , Sol-Gel Science, The Physics and Chemistry of Sol-Gel Processing, Academic Press Inc., San Diego, Ca. (1990).

Bri94 Brinker, C.J., in The Colloid Chemistry of Silica, H.E. Bergna, Ed., American Chemical Society, Washington, DC (1994), 361-402.

Bro86 Broeker, F. J., Heckman, W., Fischer, F., Mielke, M. Schroeder J., and Stange A., in Aerogels, Springer Proceedings in Physics, Vol 6, Springer Verlag, Heidleberg, FRG (1986).

Bru40 Brunauer, S., Deming, L.S., Deming, W. E., and Teller, E., Journal of the American Chemical Society, 62 (1940), 1723.

Bur92 Burggraf, L.W., Davis, L. P., and Gordon, M. S., in Ultrastructure Processing of Advanced Materials, Uhlman, D. R., and Ulrich, D.R. Eds., Wiley, New York (1992), 47-55.

Car96 Carasso, M., The Effect of Polymer Adsorption on the Electroacoustic Signals of Colloidal Silica, Ph.D. Thesis, University of Sydney, Sydney, Austrailia (1996).

Carm40 Carmen, P.C., Transactions of the Faraday Society, 36 (1940), 964.

Cao94 Cao, W.Q., and Hunt, A. J., App. Phys. Lett., 64 (1994), 2376.

Che81 Chen, W.P., and Chen, J. M., J. Opt Soc Amer., 71 (1981), 189.

Chm89 Chmel, A., Kharshak, A.A., and Kuksenko, K.N., Journal of Non-Crystalline Solids, 108 (1989), 194.

Clas87 Clasen, R., Journal of Non-Crystalline Solids, 89 (1987), 335-344.

Coh38 Cohan, L.H., Journal of the American Chemical Society, 60 (1938), 433.

Col91 Coltrain, B.K., Melpolder, S.M., and Salva, J. M., Proceedings of the IVth International Conference on Ultrastructure Processing, D.R. Uhlman and D.R. Ulrich, Eds., Wiley, New York (1991).

Col94 Coltrain B.K.,and Kelts, L.W., in The Colloid Chemistry of Silica, H.E. Bergna, Ed., American Chemical Society, Washington, DC (1994), 403.

Cor86 Corriu, R.J.P., LeClerq, D., Vious, A., Pathe, M., and Phalippou, J., in Ultrastructure Processing of Ceramics, Glasses and Composites, L.L. Hench and D. R. Ulrich, Eds., Wiley, New York (1986).

Cor88 Corriu, R.J.P., LeClerq, D., Vioux, A., and Phalippou J., in Ultrastructure Processing of Advanced Ceramics, J.D. Mackenzie and D.R. Ulrich Eds., Wiley, New York (1988), 113-126.

CRC70 CRC Handbook of Chemistry and Physics, 50th Edition, Chemical Rubber Company, Cleveland, Oh., (1970).

Dav86 Davis, L.P. and Burggraf, L.W., in Science of Ceramic Chemical Processing, L.L. Hench and Ulrich D.R., Eds., Wiley, New York (1986), 400.

Dav88 Davis, L.P. and Burggraf, L.W., in Ultrastructure Processing of Advanced Ceramics, J.D. Mackenzie, and D.R. Ulrich, Eds., Wiley, New York (1988), 367.

DeB60 DeBoer, J.H., Linsen, B.G., and Okkerse, C., K. Ned. Akad. Wet. Proc. Ser. B, 63 (1960), 360.

Deb64	DeBoer, J.H., and Lippens, B. C., Journal of Catalysis, 3 (1964), 38.
Deb65a	DeBoer, J.H., Linsen, B. G., and Osinga, Th. J., Journal of Catalysis, 4 (1965), 643.
Deb65b	DeBoer, J.H., Linsen, B. G., Van der Plas ,Th., and Zondervan, G.J., Journal of Catalysis, 4 (1965), 649.
DeBu72	DeBussetti, S.G., Tschapek M., and Helmy, A.K., J. Electroanalytical Chem., 3, (1972), 507.
Dor64	Doremus, R. H., J. Chem Phys., 40 (1964), 2389.
Dor65	Doremus, R. H., J. Chem Phys., 42 (1965), 414.
Dwi86	Dwivedi, R.K., Journal of Material Science, Letters, 5 (1986), 373-376.
Ebe46	Ebelmen, M., Ann. Chimie Phys., 16 (1846), 129.
Elm83	Elmer, T.H., Am. Ceram. Soc. Bull., 62 n4, (1983) 513-516.
Elm92	Elmer, T. H. in Engineered Materials Handbook®, Volume 4: Ceramics and Glasses, ASM International, Materials Park, OH (1992), 427.
Elm92b	Elmer, T.H., *Porous and Reconstructed Glasses*, Engineered Materials Handbook, Vol 4: Ceramics and Glasses, ASM International, Materials Park, OH (1992).
Fan83	Fanderlik, I., Optical Properties of Glass, Elsevier, New York (1983).
Flo53	Flory, P.J., Principles of Polymer Chemistry, Cornell University Press, Ithaca, NY (1953).
Fre26	Freundlich, H. Colloid and Capillary Chemistry, Methuen & Co., London (1926).
Fri86	Fricke, J., Aerogels, Springer Proceedings in Physics, Vol 6., Springer Verlag, Heidleberg, FRG (1986).
Fri87	Fricke, J., and Reichenauer, G., Journal of Non-Crystalline Solids, 95&96 (1987), 1135.
Fri92	Fricke, J., and Emmerling, A., Journal of the American Ceramic Society, 75, n8 (1992), 2027.

Fuk94 Fukumi, K., Chayahara, A., Kadono, K., Sakaguchi, T., Horino, Y., Miya, M., Fujii, K., Hayakawa, J., and Satou, M., J. Appl. Phys., 75, n6 (1994), 3075-3080.

Gra64 Graham, T., J.Chem. Soc., 17 (1864) 318.

Gre82 Gregg S.J., and Sing, K. S. W., Adsorption, Surface Area and Porosity, 2nd Ed, Academic Press Inc., London (1982).

Gro88 Gross, J. Reichenauer, G., and Fricke, J., J. Phys. D: Appl. Phys., 21 (1988), 1447.

Gur70 Gurfein, N.S., Dobychin, D.P., and Koplienko, L.S., Russ. J.Phys. Chem.,44 (1970), 411.

Hea94 Healy, T. W., in The Colloid Chemistry of Silica, H.E. Bergna, Ed., American Chemical Society, Washington, DC (1994), 147-159.

Hen90a Hench, L.L., and Wang, S.H., Phase Transitions, 24-26 (1990), 785-834.

Hen90b Hench, L. L. and West, J. K., Chemical Review, 90 (1990), 33.

Hen90c Hench, L.L. and West, J.K., Principles of Electronic Ceramics, Wiley, New York (1990).

Hen92 Hench, L.L., in Chemical Processing of Advance Materials, L.L. Hench, and J.K. West, Eds., Wiley, New York (1992), 875.

Her91 Hernandez, R., Diaz, G., Vasquez, A., Reyes-Gasga J., and Jose-Yacaman, M., Langmuir, 7 (1991), 1546-1549.

Hoo38 Hood H. P. and Nordberg, M. E., U.S. Patent, 2,106,744, Feb (1938).

Hoo42 Hood H. P. and Nordberg, M. E., U.S. Patent, 2,286,275, Feb (1942).

Hov97 Hoversten, P., USA Today, 14 July (1997), A3.

Huh72 Huheey, J. E., Inorganic Chemistry, Harper and Row, New York (1972).

Hum93 Hummel, R. E., Electronic Properties of Materials 2nd Ed., Springer Verlag, Berlin (1993).

Hun85 Hunt, A.J., Russo, R.E., Tewari, P.H., and Lafftus, K. D., Intersol '85 - Solar-Energy, Pergomon Press, New York (1985).

Hus95 Husing, N., Schwertfeger, F., Tappert, W., Schubert, U., Journal of Non-crystalline Solids, 186 (1995), 37.

Iler79 Iler, R.K., The Chemistry of Silica, Wiley, New York (1979).

Ina93 Inagaki, T, Arakawa, E. T. and Williams, M. W. Phys Rev. B, 23 (1981), 5246.

Isr85 Israelachvili, J.N., Chem. Scr., 25 (1985), 7-14.

Isr92 Israelachvili, J.N. Intermolecular And Surface Forces Second Edition, Academic Press, San Diego (1992).

Kad93 Kadono, K., Sakaguchi, T., Miya, M., Matsuoka, J., Fukumi, T., and Tanaka, H., Journal of Materials Science:Materials in Electronics, 4 (1993), 59-61.

Kau66 Kauuzman, W.A., Kinetic Theory of Gases, W. A. Benjamin, New York (1966).

Kel86 Kelts, L.W., Effinger, N.J., Melpolder, S.M., Journal of Non-crystalline Solids, 83 (1986), 353-374.

Kel88 Kelts, L.W., and Armstrong , N.J., Materials Research Society. Symposium Proceedings, Vol 121, Materials Research Society, Pittsburgh, PA (1988), 519.

Ker69 Kerker, M. The Scattering of Light, Academic Press Inc., New York (1969).

Kha52 Khaskin, I.G., Dokl. Akad. Nauk SSSR, 85 (1952) 129.

Kis31 Kistler, S.S., Nature, 127 (1931), 741.

Kre81 Kreibig, U., Optical Properties of Metal Clusters, Springer-Verlag, Heidleberg (1995).

Kro86 Krol, D.M., and Rabinovich, E.M., Journal of Non-Crystalline Solids, 82 (1986), 143.

Lam50 LaMer, V.K., Dinegar, R.H., Journal of the American Chemical Society, 72, n11 (1950), 4847.

Lip65 Lippens, B. C., and DeBoer, J.H., Journal of Catalysis, 4 (1965). 319.

Liu92 Liu S. and Hench, L.L., SPIE Vol. 1758, Sol Gel Optics II, (1992) 14-25.

Mar87 Martin, J.E., Phys. Rev. A, 36, n4 (1987), 1803.

Mat93 Matsuoka, J., Mizutani, R., Kaneko, S. , Nasu, H. , Kamiya, K., Kadono K., Sakaguchi, T., and Miya, M.., Journal of the Ceramic Society of Japan, 101, n1 (1993), 53-58.

Mau58 Maurer, R. D., J. Appl. Phys. 29 (1958), 1.

McN80 McNeill, K.J., DiCaprio, J.A., Walsh, D.A., and Pratt, R.F., Journal of the American Chemical Society, 102 (1980), 1859.

Mie08 Mie, G., Ann Physik, 25 (1908), 377-445.

Mil87 Miller, T.J., Nicol, D.A., Pohl, K.D., and Clark, H.R., Materials Research Society. Symposium Proceedings, Vol 88, Materials Research Society, Pittsburgh, PA (1987), 43.

Mon88 Montey, B.J., Journal of Non-Crystalline Solids, 99 (1988), 418.

Nas86 Nassau, K., Rabinovich, E.M., Miller, A.E., and Gallagher, P.K., Journal of Non-Crystalline Solids, 82 (1986), 78.

Nor44 Nordberg, M. E., Journal of the American Chemical Society, 27, n10 (1944), 299-305.

Orc86 Orcel, G., Gould, R.W., and Hench,L.L., Materials Research Society symposium Proceedings, Vol. 73, Materials Research Society, Pittsburgh, PA (1986), 289-294.

Orc87 Orcel, G, The Chemistry of Silica Sol-Gel, Ph.D. Dissertation, University of Florida (1987), 192.

Orc88 Orcel, G., Hench, L.L. Artaki, I., Jonas, J., and Zerda, T. W., Journal of Non-Crystalline Solids, 105 (1988), 223-231.

Pal85 Palik, E.D., Editor, Handbook of Optical Properties of Solids, Academic Press Inc., New York (1985).

Par86 Park, S. C., and Hench, L.L., in Science of Ceramic Chemical Processing, L.L. Hench, and D.R. Ulrich, Eds., Wiley (1986), 168.

Park65 Parks, G. H., Chemical Review, 65 (1965), 177.

Poh85 Pohl E.R., and Osterholz, F.D., Molecular Characterization of Composite Interfaces, H. Ishida and G. Kumar, Eds., Plenum, New York (1985), 157.

Pop86 Pope, E.J.A., and Mackenzie, J.D., Journal of Non-Crystalline Solids, 87 (1986), 185.

Qua85 Quantachrome Corporation, Operations Manual for the Autosorb 6 Nitrogen Sorption System , Quantachrome Co., Boynton Beach, FL., (1985).

Rab86a Rabinovich, E.M., and Wood, R.L., in Better Ceramics Through Chemistry II, C.J. Brinker, D.E. Clark, and D.R. Ulrich, Eds., Materials Research Society, Pittsburgh, PA (1986), p251-259.

Rab86b Rabinovich, E.M., MacChesney, J.B., and Johnson Jr., D.W., in Science of Ceramic Chemical Processing, L.L. Hench and D.R. Ulrich, Eds., Wiley, New York (1986), 208.

Rab89 Rabinovich, E.M., Krol, D.M., Kopylov N.A., and Gallagher, P.K., Journal of the American Ceramic Society, 72, n7 (1989), 1229.

Rao96 Rao P., and Doremus, R., Journal of Non-Crystalline Solids, 302 (1996), 202-205.

Rua59 Ruamps, A., Ann. Phys., 13 (1959), 1111.

Sac87 Sacks M.D., and Sheu, R. S., Journal of Non-crystalline Solids, 92 (1987), 383-396.

Sch87 Scherer G.W., in Surface and Colloid Science, Vol 14, E. Matijevic, Ed., Plenum, New York (1987), 265-300.

Sch89 Scherer, G.W., Journal of Non-Crystalline Solids, 108 (1989), 18-27.

Sch92 Scherer, G.W., Journal of Non-Crystalline Solids, 1144 (1992), 210-216.

Sche67 Scherban, J.D., Akad. Nauk. SSSR, 177, n5 (1967), 1200.

Schm86 Schmidt, H., Kaiser, A. Rudolph, M., and Lentz, A., in Science of Ceramic Chemical Processing, L.L. Hench and D. R. Ulrich, Eds., Wiley, New York (1986), 87-93.

She65 Sheinfain, R. Yu., Stas, O. P., and Neimark, I.E., Kolloidn. Zh., 27 (1965), 916.

Sin76 Sing, K. S. W., Characterization of Powder Surfaces ; with Special Reference to Pigments and Fillers, Academic Press, London (1976).

Smi95 Smith, D.M., Stein, D., Anderson, J.M., and Ackerman, W., Journal of Non-Crystalline Solids, 186 (1995), 104-112.

Sta82 Stauffer, D., Cariglio, A., and Adam, M., Advances in Polymer Science, 44 (1982), 103-158.

Sto49 Stookey, S. D., Journal of The American Ceramic Society, 32, n8 (1949), 246-249.

Stob68 Stober, W., Fink, A., and Bohn, A., Journal of Colloid Interface Science.,26 (1968), 62-69.

Str55 Struckman, C., Ann. Chem., 94 (1855), 341.

Suz87 Suzuki, F., Onozato, K., and Kurokawa,Y., Journal of Non-Crystalline, 94 (1987), 83-100.

Tew85 Tewari P.H., Hunt, P.H., and Lofftus, K.D., Materials Letters, 3 (1985), 363.

Tew86 Tewari P.H., Hunt, P.H., and Lofftus, K.D., U.S. Patent 4610,863 (1986).

Var94 Varshneya, A.K., Fundamentals of Inorganic Glasses, Academic Press, Inc., San Diego (1994).

Vyc91 Product Information Sheet for Vycor Brand Porous Glass, Corning, Inc., Corning, New York (1991).

Vys73 Vysotskii, Z.Z., and Strazhesko, D.N., in Adsorption and Absorbents, D. N. Strazhesko, Ed., Wiley, New York, (1973), 55..

Wal91 Wallace, S., Porous silica Gel Monoliths: Structural Evolution and Interactions With Water, Ph.D. Dissertation, University of Florida (1991).

Wat59 Watanabe, M., Naoke, H., and Aiba, T., Journal of the American Ceramic Society, 42, n12 (1959), 593-599.

Wij91 Wijnen, P.W.J.G., Beelen, T.P.M., Rummens, K.P.J., Saeijs H.C.P.L., De Haan J.W., Van De Ven, L.J.M., and Van Santen, R.A., Journal of Colloid and Interface Science, 145, n1 (1991), 17.

Wil76 Williams, J.P., Su, Y. S., Strzegowski, W.R., Butler, B.L., Hoover, H.L, and Altemose, V.O., American. Ceramic Society Bulletin, 55 (1976), 524-527.

Win84 Winslow, D. N., in Surface and Colloid Science, Vol 13, E. Matijevic and R. J. Good Eds., Plenum Press, New York (1984), 259.

Wint88 Winter, R., Chan, J.B., Frattini R., and Jonas, J., Journal of Non-Crystalline Solids, 105 (1988), 214.

Wint89 Winter, R., Hua, D.W., Thiyagargajan, P., and Jonas, J., Journal of Non-Crystalline Solids, 108 (1989), 137.

Woo86 Wood, D.L. and Rabinovich, E.M., Journal of Non-Crystalline Solids, 82 (1986), 171.

Yok95 Yokogawa, H., and Yokoyama, M., Journal of Non-Crystalline Solids, 186 (1995), 23-29.

Zar91 Zarzycki, J., Glasses and the Vitreous State, Cambridge University Press, Cambridge, UK (1991).

Zer86 Zerda, T.W., Artaki, I., and Jonas, J.J., Journal of Non-crystalline, 81 (1986), 365-379.

Zhur87 Zhuravlev, L.T., Langmuir, 3 (1987), 316.

Zhur93 Zhuravlev, L.T., Colloids Surf., 74, n1 (1993), 71.

Zhur94 Zhuravlev, L.T., in The Colloid Chemistry of Silica, H.E. Bergna, Ed., American Chemical Society, Washington, DC (1994), 629-676.

BIOGRAPHICAL SKETCH

Kevin W. Powers was born in New London,Connecticut, on December 7th, 1951. As a military dependent he attended a variety of schools throughout the United States. In 1969 he won an appointment to the United States Air Force Academy where he majored in chemistry and physics. At graduation in June 1973 he received the Outstanding Cadet in Chemistry award, was commissioned a second lieutenant in the U.S. Air Force and was given an Air Force Institute of Technology graduate scholarship. After receiving a Masters of Science in Chemistry degree from Michigan State University in March, 1974, he attended Air Force flight school at Webb AFB, Texas. In June 1975 he received his pilot's wings and remained at Webb Air Force Base as a primary jet instructor pilot in the Foreign Assistance Training Program.

Over the next eighteen years he flew a variety of tactical and training aircraft in the United States, Europe and the Far East. From 1981 to 1985 he served as an Assistant Professor of Chemistry at the U.S. Air Force Academy. Upon leaving the Air Force in 1993 he enrolled at the University of Florida where in May, 1998 he earned his Doctor of Philosophy degree in materials science and engineering.

I certify that I have read this study and that in my opinion it conforms to acceptable standards of scholarly presentation and is fully adequate, in scope and quality, as a dissertation for the degree of Doctor of Philosophy.

Larry L. Hench, Chairman
Graduate Research Professor of Materials
Science and Engineering

I certify that I have read this study and that in my opinion it conforms to acceptable standards of scholarly presentation and is fully adequate, in scope and quality, as a dissertation for the degree of Doctor of Philosophy.

Joseph H. Simmons, CoChair
Professor of Materials Science and
Engineering

I certify that I have read this study and that in my opinion it conforms to acceptable standards of scholarly presentation and is fully adequate, in scope and quality, as a dissertation for the degree of Doctor of Philosophy.

David E. Clark
Professor of Materials Science and
Engineering

I certify that I have read this study and that in my opinion it conforms to acceptable standards of scholarly presentation and is fully adequate, in scope and quality, as a dissertation for the degree of Doctor of Philosophy.

James H. Adair
Associate Professor of Materials Science
and Engineering

I certify that I have read this study and that in my opinion it conforms to acceptable standards of scholarly presentation and is fully adequate, in scope and quality, as a dissertation for the degree of Doctor of Philosophy.

Joseph J. Delfino
Professor of Environmental Engineering
Sciences

This dissertation was submitted to the Graduate Faculty of the College of Engineering and to the Graduate School and was accepted as partial fulfillment of the requirements for the degree of Doctor of Philosophy.

May, 1998

Winfred M. Phillips
Dean, College of Engineering

Karen A. Holbrook
Dean, Graduate School